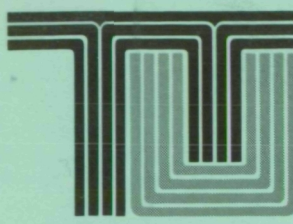


IN-39-CR
4778
P-192

NCC8-8



STRAIN SENSING USING OPTICAL FIBERS

FINAL REPORT

Richard Houghton/Steven Hiles

(NASA-CR-195807) STRAIN SENSING
USING OPTICAL FIBERS Final Report
(Tennessee Technological Univ.)
192 p

N94-32940

unclas

63/39 0004778

Technical Report #MCTR-0594-07

Center for Manufacturing Research
and
Technology Utilization

Cookeville, Tennessee 38505

STRAIN SENSING USING OPTICAL FIBERS

FINAL REPORT

Richard Houghton/Steven Hiles

Technical Report #MCTR-0594-07

TABLE OF CONTENTS

	Page
LIST OF FIGURES	vii
LIST OF TABLES	xiv
LIST OF SYMBOLS	xvii
Chapter	
1. Introduction	1
2. Analytical Relationships For Optical Waveguides	4
2.1 Derivation of Singlemode Optical Fiber Properties	6
2.1.1 Wave Propagation	7
2.1.2 Steady-State Wave Propagation	14
2.1.3 Wave Parameters	19
2.1.4 Waveguide Equations	21
2.1.5 Step-Index Optical Fiber	30
2.1.6 Modes in an Optical Fiber	38
2.1.7 Cutoff Conditions for Propagating Modes	40
2.2 Loss Properties in Optical Fibers	47
2.2.1 Transition Losses	49
2.2.2 Pure Bend Losses - The Whispering Gallery Mode	51
2.3 Strain Sensing	56
3. Attenuation Measurement Methods	60
3.1 Continuous Wave Through Transmission	60
3.2 Optical Time Domain Reflectometry	61

Chapter	Page
3.3 Photon Counting Reflectometer	64
4. Experimental Evaluation of Whispering Gallery Modes - CWTT	66
4.1 Reduction of the Whispering Gallery Mode	69
4.2 Characterization of Whispering Gallery Modes	78
5. Experimental Evaluation of Whispering Gallery Modes - Reflectometry	87
6. Applications of the Optical Fiber Strain Sensor to Test Parts	91
6.1 Application of Strain Sensor to a Filament Wound Graphite Tube	91
6.2 Application of Strain Sensor to a Graphite Filament Wound Flat Panel	93
6.3 Application of Strain Sensor to a Four Layer Polycarbonate Flat Panel	95
7. Evaluation of the Strain Sensor Embedded in a Test Structure	98
7.1 Temperature Testing of The Flat Graphite Panel to Determine Serpentine Bend Radius	100
7.2 Graphite Tube Under Three Point Loading	102
7.3 Flat Graphite Panel Under Three Point Loading	104
7.4 Lexan Flat Panel Subjected to Three Point Loading	106
7.4.1 Lexan Specimen Tests Relating Attenuation To Structural Loading	108
7.4.2 Lexan Specimen Tests Relating Attenuation To Fiber Bend Radius	114
7.4.3 Lexan Specimen Testing Compared To Taper Test Data	118

Chapter		Page
7.4.4 Lexan Specimen Tests Relating Attenuation To Structural Strain		126
8. Conclusions and Recommendations for Future Research		132
REFERENCES		140
APPENDICES		
A. Tabular Data For Attenuation as a Function of Optical Fiber Bending		141
B. Results of Temperature Characterization Using Attenuation as a Function of Temperature		142
C. Tabular Data for Attenuation as a Function of Temperature Characterization		150
D. Results of Temperature Characterization Using Attenuation as a Function of Temperature Rate		151
E. Data For Attenuation as a Function of Radius Change Using Optical Reflectometry		159
F. Termination Methods For Optical Fibers Embedded in Graphite Composite Structures		160
G. Tabular Data For Sample Structures Under Three Point Loading . .		170
H. Data Acquisition Program Used To Transfer Data From LeCroy Oscilloscope to Computer		171

LIST OF FIGURES

Figure		Page
2.1	Schematics of Typical Singlemode and Multimode Fibers	4
2.2	The Bessel Functions and the Mode Cutoff Conditions	46
2.3	Schematic of an Optical Fiber Bent to a Radius R Showing One of the Whispering Gallery Mode Rays Between the Radiation Caustic (r.c) and the Cladding Surface	53
2.4	A Schematic Showing The Properties Used to Relate Fiber Bend Radius to Structural Bend Radius	57
3.1	Display of an OTDR Showing the Dead Zone of the Fiber	63
4.1	Test Setup Used to Test Attenuation vs. Bending Using CWTT and Drill Rods	67
4.2	P_{out}/P_{in} vs. Bend Radius for an 850 nm SM Fiber with an 833 nm Laser(18 Data Points)	67
4.3	α Attenuation per Bend Length vs. Bend Radius for an 850 nm SM Fiber with an 833 nm Laser(18 Data Points)	68
4.4	Test Setup Using Tapered Shanks to Determine Attenuation as a Function of Bend Radius	69
4.5	P_{out}/P_{in} vs. Bend Radius for an 850 nm SM Fiber with an 833 nm Laser (23 Data Points, 125 Data Points, and 184 Data Points)	70
4.6	α Attenuation vs. Bend Radius for the 184 Data Point Test Showing the Theoretical Curve and the Synchronous Coupling Points	72
4.7	P_{out}/P_{in} vs. Bend Radius for a 514 nm SM Fiber and a 670 nm Laser	73

Figure		Page
4.8	α Attenuation per Bend Length vs. Bend Radius for a 514 nm SM Fiber and a 670 nm Laser	74
4.9	P_{out}/P_{in} vs. Bend Radius for a 633 nm SM Fiber Using an 833 nm Laser	75
4.10	α Attenuation per Bend Length vs. Bend Radius for a 633 nm SM Fiber Using an 833 nm Laser	75
4.11	P_{out}/P_{in} vs. Bend Radius for an 850/1300 nm MM Fiber Using an 830 nm Laser	77
4.12	α Attenuation per Bend Length vs. Bend Radius for an 850/1300 nm MM Fiber Using an 830 nm Laser	77
4.13	Schematic of The Setup Used to Test the Optical Fiber's Sensitivity to Heating	79
4.14	Heat Test of the Aluminum and Steel Tapers Showing Attenuation vs. Actual Temperature Change	80
4.15	Heat Test of the Aluminum and Steel Tapers Showing The Attenuation vs. Radius Change Caused by Thermal Expansion of the Taper	80
4.16	Attenuation vs. Bend Radius for the SM 850 nm Fiber Showing the Test Points Used in the Heat Test	82
4.17	Example Figure Used in Determining the Fiber Bend Radius from Temperature Testing	85
5.1	α Attenuation vs. Bend Radius for 1300/1550 nm SM Fiber Using the Hewlett Packard and the Ando OTDRs	88
5.2	α Attenuation vs. Bend Radius for the 850 nm MM Fiber Using the PCR	90
6.1	Schematic View of the Graphite Mandrel Wrapped Tube	92
6.2	Schematic View of the Graphite Mandrel Wrapped Flat Panel	94

Figure		Page
6.3	Configuration of Lexan specimen with Optical Sensors Embedded	96
7.1	Three Point Bend Fixture Used to Find the Attenuation vs. Bending for the Sample Structures	99
7.2	Test Setup for Determining the Relation of Attenuation to Fiber Bend Radius using a Sample Structure	99
7.3	Attenuation as a Function of Temperature for the Flat Panel Sample Structure	101
7.4	Complex Fourier Transform of the Flat Panel Temperature Data	101
7.5	Theoretical and Experimental Results for Attenuation vs. Radius Change Due to Three Point Loading of the Graphite Tube	103
7.6	Theoretical and Experimental Results for Attenuation vs. Radius Change Due to Three Point Loading of the Flat Panel	105
7.7	Schematic of Lexan Specimen Showing Load Test Points	107
7.8	Three Point Loading of Lexan Specimen for Test 1	109
7.9	Three Point Loading of Lexan Specimen for Test 2	109
7.10	Three Point Loading of Lexan Specimen for Test 3	110
7.11	Three Point Loading of Lexan Specimen for Test 4	110
7.12	Three Point Loading of Lexan Specimen for Test 5	111
7.13	Three Point Loading of Lexan Specimen for Test 6	111
7.14	Three Point Loading of Lexan Specimen for Test 7	112
7.15	Three Point Loading of Lexan Specimen for Test 8	112
7.16	Attenuation as a Function of Fiber Bend Radius for Test 1	114

Figure	Page
7.17 Attenuation as a Function of Fiber Bend Radius for Test 2	115
7.18 Attenuation as a Function of Fiber Bend Radius for Test 3	115
7.19 Attenuation as a Function of Fiber Bend Radius for Test 4	116
7.20 Attenuation as a Function of Fiber Bend Radius for Test 6	116
7.21 Attenuation as a Function of Fiber Bend Radius for Test 7	117
7.22 Attenuation as a Function of Fiber Bend Radius for Test 8	117
7.23 Tests 1 and 3 from Lexan Specimen Overlaid onto Taper Test Data	119
7.24 Tests 2 and 8 from Lexan Specimen Overlaid onto Taper Test Data	120
7.25 Tests 4 and 7 Overlaid onto Taper Test Data	120
7.26 Lexan Test 6 overlaid onto the Taper Test Data	121
7.27 Comparison of Taper Test with Corrected Data from Lexan Tests 1 and 3	124
7.28 Comparison of Corrected Lexan Tests 2 and 8 to the Taper Test	125
7.29 Comparison of Lexan Tests 4 and 7 to Taper Test	125
7.30 Comparison of Lexan Test 6 and Taper Test	126
7.31 Structural Strain vs. Attenuation For Lexan Test 1 (Compressive Stress)	127
7.32 Structural Strain vs. Attenuation For Lexan Test 2 (Compressive Stress)	128
7.33 Structural Strain vs. Attenuation For Lexan Test 3 (Tensile Stress)	128
7.34 Structural Strain vs. Attenuation For Lexan Test 4 (Tensile Stress)	129

Figure	Page
7.35 Structural Strain vs. Attenuation For Lexan Test 6 (Tensile Stress)	129
7.36 Structural Strain vs. Attenuation For Lexan Test 7 (Compressive Stress)	130
7.37 Structural Strain vs. Attenuation For Lexan Test 8 (Tensile Stress)	130
B.1 Attenuation vs. Temperature at a Bend Radius of .329569 cm (Peak 1)	143
B.2 Attenuation vs. Temperature at a Bend Radius of .352924 cm (Peak 2)	143
B.3 Attenuation vs. Temperature at a Bend Radius of .381840 cm (Peak 3)	144
B.4 Attenuation vs. Temperature at a Bend Radius of .409644 cm (Peak 4)	144
B.5 Attenuation vs. Temperature at a Bend Radius of .444121 cm (Peak 5)	145
B.6 Attenuation vs. Temperature at a Bend Radius of .334017 cm (Middle 1)	145
B.7 Attenuation vs. Temperature at a Bend Radius of .347363 cm (Middle 2)	146
B.8 Attenuation vs. Temperature at a Bend Radius of .419654 cm (Middle 3)	146
B.9 Attenuation vs. Temperature at a Bend Radius of .453019 cm (Middle 4)	147
B.10 Attenuation vs. Temperature at a Bend Radius of .340690 cm (Valley 1)	147

Figure		Page
B.11	Attenuation vs. Temperature at a Bend Radius of .366270 cm (Valley 2)	148
B.12	Attenuation vs. Temperature at a Bend Radius of .395186 cm (Valley 3)	148
B.13	Attenuation vs. Temperature at a Bend Radius of .427439 cm (Valley 4)	149
B.14	Attenuation vs. Temperature at a Bend Radius of .460804 cm (Valley 5)	149
D.1	Complex Fourier Transform of the Heat Test Data at a Bend Radius of .329596 cm (Peak 1)	152
D.2	Complex Fourier Transform of the Heat Test Data at a Bend Radius of .352924 cm (Peak 2)	152
D.3	Complex Fourier Transform of the Heat Test Data at a Bend Radius of .381840 cm (Peak 3)	153
D.4	Complex Fourier Transform of the Heat Test Data at a Bend Radius of .409644 cm (Peak 4)	153
D.5	Complex Fourier Transform of the Heat Test Data at a Bend Radius of .444121 cm (Peak 5)	154
D.6	Complex Fourier Transform of the Heat Test Data at a Bend Radius of .334017 cm (Middle 1)	154
D.7	Complex Fourier Transform of the Heat Test Data at a Bend Radius of .347363 cm (Middle 2)	155
D.8	Complex Fourier Transform of the Heat Test Data at a Bend Radius of .419654 cm (Middle 3)	155
D.9	Complex Fourier Transform of the Heat Test Data at a Bend Radius of .453019 cm (Middle 4)	156

Figure	Page
D.10 Complex Fourier Transform of the Heat Test Data at a Bend Radius of .340690 cm (Valley 1)	156
D.11 Complex Fourier Transform of the Heat Test Data at a Bend Radius of .366270 cm (Valley 2)	157
D.12 Complex Fourier Transform of the Heat Test Data at a Bend Radius of .395186 cm (Valley 3)	157
D.13 Complex Fourier Transform of the Heat Test Data at a Bend Radius of .427439 cm (Valley 4)	158
D.14 Complex Fourier Transform of the Heat Test Data at a Bend Radius of .460804 cm (Valley 5)	158
F.1 Prism-Lens System for Fiber Termination	163
F.2 Sine Wave Light Pattern Through GRIN Lens	164
F.3 Boot Connector for Fiber Termination	166

LIST OF TABLES

Table		Page
2.1	Types of Propagating Modes in a Dielectric	26
4.1	Mean and Frequency Values from Temperature Characterization of Optical Fiber	84
7.1	Descriptions of the Tests performed on the Lexan Specimen	107
A.1	Attenuation as a Function of Fiber Bending For an 850 nm SM Fiber and an 833 nm Laser Using Rods of Varying Radius (18 Data Points)	Disk
A.2	Attenuation as a Function of Fiber Bending For an 850 nm SM Fiber and an 833 nm Laser Using Aluminum Tapers (23 Data Points, 125 Data Points, and 184 Data Points)	Disk
A.3	Theoretical and Experimental Values of Attenuation as a Function of Bending For an 850 nm SM Fiber and an 833 nm Source	Disk
A.4	Attenuation as a Function of Fiber Bending For a 514 nm SM Fiber and a 670 nm Laser Using the Taper Fixture	Disk
A.5	Attenuation as a Function of Fiber Bending For a 630 nm SM Fiber and an 833 nm Laser Using the Taper Fixture	Disk
A.6	Attenuation as a function of Fiber Bending For an 850/1300 nm MM Fiber and an 833 nm Laser Using the Taper Fixture	Disk
A.7	Attenuation as a Function of Temperature For an 850 nm SM Fiber and an 833 nm Laser Using the Aluminum and Steel Tapers	Disk
C.1	Attenuation as a Function of Temperature For an 850 nm SM Fiber and an 833 nm Laser Using the Graphite Taper at a Bend Radius of .329569 cm (Peak 1)	Disk
C.2	Attenuation as a Function of Temperature For an 850 nm SM Fiber and an 833 nm Laser Using the Graphite Taper at a Bend Radius of .352924 cm (Peak 2)	Disk

Table	Page
C.3 Attenuation as a Function of Temperature For an 850 nm SM Fiber and an 833 nm Laser Using the Graphite Taper at a Bend Radius of .381840 cm (Peak 3)	Disk
C.4 Attenuation as a Function of Temperature For an 850 nm SM Fiber and an 833 nm Laser Using the Graphite Taper at a Bend Radius of .409644 cm (Peak 4)	Disk
C.5 Attenuation as a Function of Temperature For an 850 nm SM Fiber and an 833 nm Laser Using the Graphite Taper at a Bend Radius of .444121 cm (Peak 5)	Disk
C.6 Attenuation as a Function of Temperature For an 850 nm SM Fiber and an 833 nm Laser Using the Graphite Taper at a Bend Radius of .334017 cm (Middle 1)	Disk
C.7 Attenuation as a Function of Temperature For an 850 nm SM Fiber and an 833 nm Laser Using the Graphite Taper at a Bend Radius of .347363 cm (Middle 2)	Disk
C.8 Attenuation as a Function of Temperature For an 850 nm SM Fiber and an 833 nm Laser Using the Graphite Taper at a Bend Radius of .419654 cm (Middle 3)	Disk
C.9 Attenuation as a Function of Temperature For an 850 nm SM Fiber and an 833 nm Laser Using the Graphite Taper at a Bend Radius of .435019 cm (Middle 4)	Disk
C.10 Attenuation as a Function of Temperature For an 850 nm SM Fiber and an 833 nm Laser Using the Graphite Taper at a Bend Radius of .340690 cm (Valley 1)	Disk
C.11 Attenuation as a Function of Temperature For an 850 nm SM Fiber and an 833 nm Laser Using the Graphite Taper at a Bend Radius of .366270 cm (Valley 2)	Disk
C.12 Attenuation as a Function of Temperature For an 850 nm SM Fiber and an 833 nm Laser Using the Graphite Taper at a Bend Radius of .395186 cm (Valley 3)	Disk

Table	Page
C.13 Attenuation as a Function of Temperature For an 850 nm SM Fiber and an 833 nm Laser Using the Graphite Taper at a Bend Radius of .427439 cm (Valley 4)	Disk
C.14 Attenuation as a Function of Temperature For an 850 nm SM Fiber and an 833 nm Laser Using the Graphite Taper at a Bend Radius of .460804 cm (Valley 5)	Disk
E.1 Attenuation as a Function of Fiber Bending For a 1300/1550 nm SM Fiber Using the Hewlett-Packard and Ando OTDRs	Disk
E.2 Attenuation as a Function of Fiber Bending For a 850/1300 nm MM Fiber Using the Photon Counting Reflectometer (Fresnel Detection Mode)	Disk
G.1 Results of the Temperature Testing Performed on the Flat Graphite Panel	Disk
G.2 Attenuation as a Function of Fiber Bending for a 1300/1550 nm SM Fiber Embedded in a Graphite Tube	Disk
G.3 Attenuation as a function of Fiber Bending For an 850 nm SM Fiber Embedded in a Flat Graphite Panel	Disk
G.4 Lexan Test 1: Sensor 2 of Fiber 2 Active (Compression)	Disk
G.5 Lexan Test 2: Sensor 2 of Fiber 2 Active (Compression)	Disk
G.6 Lexan Test 3: Sensor 2 of Fiber 2 Active (Compression)	Disk
G.7 Lexan Test 4: Sensor 2 of Fiber 2 Active (Compression)	Disk
G.8 Lexan Test 5: Sensor 2 of Fiber 2 Active (Compression)	Disk
G.9 Lexan Test 6: Sensor 2 of Fiber 2 Active (Compression)	Disk
G.10 Lexan Test 7: Sensor 2 of Fiber 2 Active (Compression)	Disk
G.11 Lexan Test 8: Sensor 2 of Fiber 2 Active (Compression)	Disk

Table	Page
G.12 Data From Lexan Testing Including Data With Interface Correction Factor of 9 Applied	Disk

LIST OF SYMBOLS

Symbol	Description	Units
A_r	Average transition loss	
a	Radius of optical fiber core	m
\bar{a}	General unit vector	
$\bar{\mathcal{B}}$	Magnetic flux density	Wb/m^2
c	Speed of light in free space	m/s
$\bar{\mathcal{D}}$	Electric flux density	C/m^2
d	Distance from the center of the fiber core to the radiation caustic	m
\bar{E}	Electric field vector	
E_{st}	Structural Modulus of Elasticity (Young's Modulus)	psi
$\bar{\mathcal{E}}$	Electric field intensity	V/m
EH	Hybrid electric-magnetic mode with electric field dominating	
\bar{F}	General vector variable	
f	General scalar variable, frequency	
\bar{H}	Magnetic field vector	
$\bar{\mathcal{H}}$	Magnetic field intensity	A/m
HE	Hybrid electric-magnetic mode with magnetic field dominating	
\bar{j}	Current density	A/m^2
k	Wave number	
\bar{k}	Propagating wave vector	
L_1	Path length of a ray between cladding/buffer reflections	m
L_2	Path length of a ray between cladding/buffer reflections	m
m	Integer value defining synchronous coupling radii	
n	General refractive index of a medium	
\bar{n}	Unit vector in the direction of wave propagation	
n_1	Refractive index of optical fiber core	
n_2	Refractive index of optical fiber cladding	
NA	Numerical aperture	
P_{in}	Input power for optical fiber	W
P_{out}	Output power for optical fiber	W
R	Serpentine bend radius	cm
\bar{r}	Radius vector for cylindrical coordinates	
t	time variable for derivatives	sec
TE	Transverse electric mode	

Symbol	Description	Units
TM	Transverse magnetic mode	
w_o	Mode field radius	m
y	Distance from center of core to cladding/buffer interface	m
α	Optical attenuation	dB
α_c	Average pure bend loss	dB
β	Longitudinal component of the propagating vector \vec{k}	
β_0	Variable representing a point on a plane of constant phase	
Δn	Index difference between the core and the cladding	
ϵ	Permittivity	F/m
ϵ_r	Relative permittivity	F/m
λ	Spatial wavelength	
λ_0	Cutoff wavelength	
μ	Permeability of a medium	H/m
μ_r	Relative permeability of a medium	H/m
v	Velocity of plane wave propagation, Phase velocity	m/s
v_{pr}	Poison's Ratio	
ρ	Charge density	C/m ³
$\rho(\theta_f)$	Bend radius of optical fiber based on orientation	cm
σ	Conductivity of a medium	S/m
σ_x	Normal stress in the x direction	psi
σ_y	Normal stress in the y direction	psi
ϕ	Phase change	
ψ	General wavelength variable	
ω	Frequency	Hz
ω_c	Mode cutoff frequency	
∇	Del Operator	

CHAPTER 1

Introduction

From the beginning of communication technology, the industry has used increasingly higher frequencies of electromagnetic waves to transmit signals. Radio waves on the order of kilometers were soon shortened to meters which were then shortened to fractions of meters. Microwave technology soon followed and finally, after the invention of the laser, optical communications with wavelengths on the order of nanometers was developed. After it was discovered that light could be guided down hollow pipes with the use of lenses, the industry sought a continuous media which could guide the light waves for long lengths.

The first optical waveguides (optical fibers) developed had such high light losses it was assumed that this method would not produce a usable communications media. These losses, referred to as attenuation, are caused by manufacturing defects and the environmental losses due to conditions in which the fiber is placed. Examples of manufacturing defects are (1) impurities which cannot be removed from the optical fiber as it is formed and (2) slight discontinuities in the guide structures. Examples of environmental losses are when the fiber is subjected to (1) tension, (2) axial twisting, (3) temperature changes, or (4) bending.

Kao and Davies [1] during their study of the transmission of light in pure fused silica rods found that the attenuation for this media was on the order of tens of dB/km for a straight rod with no environmental loss effects included. This was a tremendous improvement compared to losses of thousands of dB/km for the material used in the first optical fibers. In 1970, a high silica fiber produced by Corning Glass had losses of 20

dB/km. Presently, silica optical fiber with losses of less than 0.2 dB/km are being produced which satisfy the current communication industries needs.

All of the principles used to develop fiber optics for the communications industry hold true for strain sensing applications except that some of the advantages in fibers for communications are disadvantages for smart sensing. In communications, the ideal fiber would have zero attenuation from both manufacturing defects and environmental loss effects. This would essentially mean that light could travel an infinite length through an optical fiber without losing any optical power. For strain sensing, the attenuation due to the impurities is not important, but the losses due to bending or axially loading are. The optical fibers property of light attenuation when bent is the basis of mechanical strain sensing since the embedded fiber is strained in bending as the structure deflects. In this way, advancements in optical fibers for the communications industry are developing in a direction opposite to the needs of the strain sensing industry.

There are many different fiber designs on the market today and they are categorized as either singlemode or multimode fibers. Singlemode fibers are ones which, when used with a matching wavelength laser, allow only a specified mode of light to pass through the fiber without significant attenuation. All other modes except the specified mode are attenuated after a short length of travel in the fiber. Multimode fibers allow hundreds of different modes to pass through the optical fiber without being greatly attenuated.

There is also a wide variety of products on the market which determine the levels of attenuation in the optical fibers, and these also fall into two classes. These classes of attenuation measurement are either Through Transmission testing or Optical Time Domain Reflectometry(OTDR). With the Through Transmission testing the laser source is placed at one end of the optical fiber and the light is detected at the other end of the fiber. Using

the OTDR, light is sent through the fiber and light reflections in the fiber are detected at the same end. A more sophisticated OTDR called a Photon Counting Reflectometer(PCR) uses microwave technology and highly stable triggering to provide much higher resolution than the typical OTDR, but it still operates on the same reflection principle.

The main source of attenuation which will be studied is the fiber's sensitivity to bending at radii that are much larger than the radius of the fiber. This type of environmental attenuation causes losses that are a function of the severity of the bend. The average attenuation caused by bending varies exponentially with the bend radius.

There are many different fibers, sources, and testing equipment available. This thesis describes tests that were performed to evaluate the variables that effect bending related attenuation and will discuss the consistency of the results. Descriptions and comparisons will be made between singlemode and multimode fibers as well as instrumentation comparisons between detection equipment. Detailed analysis of the effects of the Whispering Gallery mode will be performed along with theorized methods for characterization of these modes.

CHAPTER 2

Analytical Relationships For Optical Waveguides

Optical fibers can be thought of as two coaxial cylinders of glass, each of which has a different index of refraction. The inside cylinder is termed the core of the fiber and the outside cylinder is called the cladding. The index of refraction of the core is always slightly larger than the index of the cladding and there is typically less than 2 percent difference in the indexes. The differences in indexes allows the rays to reflect at the interface so they are guided along the length of the fiber by internal reflection. If the core has a uniform refraction index the fiber is called a "step index fiber." This is due to the "step" change in index between the core and the cladding. If the core has a nonuniform index which gradually decreases from the center toward the cladding, the fiber is termed "gradient-index fiber." This is due to the gradient change in the index of the core. Figure 2.1 shows schematics of singlemode and multimode fibers with the different refractive indexes for the core and cladding.

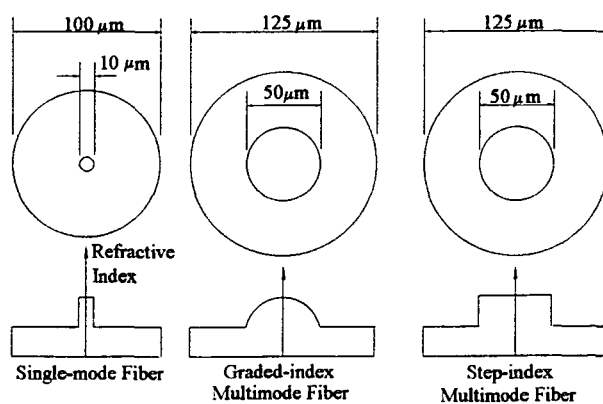


Figure 2.1. Schematics of typical singlemode and multimode fibers

Optical fibers can be separated into two major classes, singlemode and multimode fibers. Within these major classes, various types of fiber such as step-index and gradient-index are found which have different guide structures. A singlemode fiber is one which allows only one mode of light to travel through the waveguide. This type of fiber is used in communications where very high bandwidths are required. Although the singlemode fiber carries only one mode, the mode exists in two mutually orthogonal polarizations. Multimode fibers are used with lower bandwidth systems such as optical scanners or image projection equipment. Multimode fibers can transmit hundreds of different modes simultaneously due to the design of the guide structure.

In both singlemode and multimode fibers, the light travels through the core by internal reflection at the cladding-core interface. If the rays of light pass through the interface they are only able to propagate for a short distance until they are lost through the cladding to the surroundings or are attenuated in the cladding. From Snell's law there is an angle at which total internal reflection occurs and is termed the critical angle. The numerical aperture (NA) of an optical fiber is related to the critical angle by

$$NA = n_1 \sin \theta_c \quad (2.1)$$

where θ_c = the critical angle for total internal reflection and

n_1 = the refractive index of the fiber core.

The numerical aperture is a means of defining the maximum acceptance angle of light for a fiber. The NA is also related to the difference between the core and cladding refractive indexes by the relationship [3]

$$NA = \sqrt{n_1^2 - n_2^2} \quad (2.2)$$

where n_2 = the refractive index of the fiber cladding.

Based on how the light is guided in different types of optical fiber it seems that the singlemode fiber would produce the best strain sensor. This is because the guide properties of the singlemode are simple in comparison to the multimode fibers. With the singlemode fiber, the derivation of wave propagation, wave equations, types of propagating modes, and the field descriptions are not complicated by having hundreds of modes propagating in the fiber. For this reason, optical waveguide properties are derived in this thesis for the singlemode fiber only.

The main type of attenuation studied for optical strain sensing is the optical fibers attenuation due to macrobending. This type of loss is found when an optical fiber is bent to a radius much larger than the radius of the fiber. When the optical fiber is bent, there are three main locations on the fiber which have significance. These are the two points of transition from a straight fiber to the bent section of a prescribed radius and the length of the fiber which experiences the actual bend. The two radius transition points produce transition losses and the bent section produces a pure bend loss. These two loss mechanisms are based on different principles and are treated as individual properties of attenuation due to bending.

2.1 Derivation of Singlemode Optical Fiber Properties

The study of how light propagates in an optical fiber is an important part of understanding what causes attenuation and how the guide parameters affect relations in attenuation and fiber bending. Important factors such as cutoff conditions, types of

propagating modes allowed, and propagation parameters can all be obtained from the characteristic equations which describe a specific waveguide.

Characteristic equations are used in many different sciences and are the basis for describing systems. Due to the many different factors involved in optical waveguides the characteristic equations are complex. For this reason the derivation of these equations in the next sections is approached by starting with Maxwell's Equations for electromagnetic fields.

2.1.1 Wave Propagation

The derivation of how light waves propagate in an optical fiber will be made with respect to a singlemode step index fiber, but the formulation is similar for all types of fibers. The mathematical development that follows is a condensation of material found in References [2], [3], and [4].

The derivation begins with the differential form of Maxwell's equations since they are the basis for relating field vectors at a given space and time. The Maxwell's equations for electromagnetic fields are found to be

$$\nabla \times \bar{E} = -\frac{\partial \bar{B}}{\partial t} \quad (2.3)$$

$$\nabla \times \bar{H} = \bar{J} + \frac{\partial \bar{D}}{\partial t} \quad (2.4)$$

$$\nabla \cdot \bar{B} = 0 \quad (2.5)$$

$$\nabla \cdot \bar{D} = \rho \quad (2.6)$$

where \bar{E} = electric field intensity, Volt/meter, V/m

\bar{B} = magnetic flux density, Weber/meter², Wb/m²

\bar{D} = electric flux density, Coulomb/meter², C/m²

\bar{H} = magnetic field intensity, Ampere/meter, A/m

\bar{J} = current density, Ampere/meter², A/m²

and

ρ = Charge density, Coulomb/meter³, C/m³.

For a linear, isotropic, homogeneous medium such as a dielectric guide, Equations (2.3) to (2.6) are related by the constitutive relations

$$\bar{J} = \epsilon(\bar{E}) \quad (2.7)$$

$$\bar{B} = \mu(\bar{H}) \quad (2.8)$$

$$\bar{J} = \sigma(\bar{E}) \quad (2.9)$$

where ϵ = Permittivity, F/m

μ = Permeability of the medium, Henry/meter, H/m

and

σ = conductivity of the medium, 1/(Ohm*meter), 1/(Ω·m).

For lossless dielectrics the permittivity, permeability, and conductivity have the following values:

$$\sigma = 0$$

$$\mu_r = \frac{\mu}{\mu_0} = 1 \quad (2.10)$$

$$\epsilon_r = \frac{\epsilon}{\epsilon_0}$$

where μ_r = relative permeability of the medium,

ϵ_r = relative permittivity of the medium,

$$\mu_0 = 4\pi \times 10^{-7}, \text{ H/m} = \text{free space parameter},$$

and

$$\epsilon_0 = \frac{1}{36\pi \times 10^9}, \text{ F/m} = \text{free space parameter}.$$

Since the medium used in optical fibers is glass, the permittivity is usually referred to as the index of refraction of a medium. The relation of the index to permittivity is

$$n = \sqrt{\epsilon_r}. \quad (2.11)$$

The Maxwell's equations for a charge-free, lossless, linear isotropic material such as the dielectric waveguide are the same as Equations (2.3) to (2.6) except that Equation (2.6) is set equal to zero since the guide is charge free so there is no charge density. Equation (2.6) then becomes

$$\nabla \cdot \vec{D} = 0. \quad (2.12)$$

By substituting Equation (2.10) into Equations (2.7) to (2.9), the constitutive relationships for the specific guide become

$$\begin{aligned} \mu_r &\approx 1 \\ \bar{B} &= \mu_0 \bar{H} \\ \bar{D} &= \epsilon \bar{E}. \end{aligned} \quad (2.13)$$

The wave equation for an optical fiber can be found using Equations (2.3) to (2.5), Equation (2.12) and the constitutive relations from Equation (2.13). This equation provides a simple relation for describing the propagation of energy through a medium. For the research in this thesis the medium is an optical fiber and the propagation energy is in the form of light photons. The equations which describe the electric and magnetic fields are found using the same derivations therefore only one type will be presented. The electric field equations will be derived and only the important magnetic field equations will be shown.

Taking the curl of Equation (2.3) and substituting Equation (2.13):

$$\nabla \times \nabla \times \bar{\mathcal{E}} = \nabla \times \frac{\partial \bar{\mathcal{B}}}{\partial t} = -\mu_0 \frac{\partial}{\partial t} (\nabla \times \bar{\mathcal{H}}). \quad (2.14)$$

Using Equation (2.4) in Equation (2.14):

$$\nabla \times \nabla \times \bar{\mathcal{E}} = -\mu_0 \frac{\partial}{\partial t} \left(\frac{\partial \bar{\mathcal{B}}}{\partial t} \right) = -\mu_0 \frac{\partial^2 \bar{\mathcal{B}}}{\partial t^2}. \quad (2.15)$$

Substituting Equation (2.13) into Equation (2.15):

$$\nabla \times \nabla \times \bar{\mathcal{E}} = -\mu_0 \epsilon \frac{\partial^2 \bar{\mathcal{E}}}{\partial t^2}. \quad (2.16)$$

Using the Curl identity: $\nabla \times \nabla \times \bar{F} = \nabla(\nabla \cdot \bar{F}) - \nabla^2 \bar{F}$, Equation (2.16) becomes after arrangement:

$$\nabla^2 \bar{\epsilon} - \mu_0 \epsilon \frac{\partial^2 \bar{\epsilon}}{\partial t^2} = \nabla(\nabla \cdot \bar{\epsilon}). \quad (2.17)$$

In order to get the right side of Equation (2.17) in the proper form, apply Equation (2.13) to Equation (2.12) as follows:

$$\nabla \cdot \bar{\epsilon} = 0 \Rightarrow \nabla \cdot (\epsilon \bar{\epsilon}) = 0. \quad (2.18)$$

Using the identity of the Del operator, $\nabla \cdot (fF) = f\nabla \cdot F + F \cdot \nabla f$, Equation (2.18) becomes

$$\nabla \cdot (\epsilon \bar{\epsilon}) = \epsilon \nabla \cdot \bar{\epsilon} + \bar{\epsilon} \cdot \nabla \epsilon = 0. \quad (2.19)$$

Solving for $\nabla \cdot \bar{\epsilon}$ in Equation (2.19):

$$\nabla \cdot \bar{\epsilon} = -\bar{\epsilon} \cdot \frac{\nabla \epsilon}{\epsilon}. \quad (2.20)$$

Substituting Equation (2.20) into Equation (2.17) results in the inhomogenous equation:

$$\nabla^2 \bar{\epsilon} - \mu_0 \epsilon \frac{\partial^2 \bar{\epsilon}}{\partial t^2} = -\nabla(\bar{\epsilon} \cdot \frac{\nabla \epsilon}{\epsilon}). \quad (2.21)$$

For a homogenous medium, the gradient of the permittivity (refractive index) is zero therefore Equation (2.21) becomes

$$\nabla^2 \bar{E} - \mu_0 \epsilon \frac{\partial^2 \bar{E}}{\partial t^2} = 0. \quad (2.22)$$

Equation (2.22) is the homogeneous wave equation for the electric field. Similarly by starting with Equation (2.4) of Maxwell's equations the homogeneous wave equation for the magnetic field is

$$\nabla^2 \bar{H} - \mu_0 \epsilon \frac{\partial^2 \bar{H}}{\partial t^2} = 0 \quad (2.23)$$

Equations (2.22) and (2.23) are vector wave equations which can be separated into their x, y, and z components. Letting

$$v = \frac{1}{\sqrt{\mu_0 \epsilon}} \text{ m/s} \quad (2.24)$$

then from Equation (2.24):

$$\mu_0 \epsilon = \frac{1}{v^2} \quad (2.25)$$

and Equations (2.22) and (2.23) can be written as scalar equations with the general form:

$$\nabla^2 \psi - \frac{1}{v^2} \frac{\partial^2 \psi}{\partial t^2} = 0 \quad (2.26)$$

where ψ represents the components of the electric and magnetic fields in rectangular coordinates.

The general solution of Equation (2.26) is given as

$$\psi = f(t \pm \frac{1}{v} \bar{n} \cdot \bar{r}) \quad (2.27)$$

as long as the second derivative of f exists. Equation (2.27) defines a plane wave propagating in a dielectric medium since it is the general expression for both electric and magnetic fields. \bar{r} is a radius vector given in rectangular coordinates as

$$\bar{r} = x \bar{a}_x + y \bar{a}_y + z \bar{a}_z \quad (2.28)$$

where \bar{a}_x , \bar{a}_y , and \bar{a}_z are unit vectors in the x y z space. \bar{n} is a unit vector in the direction of wave propagation which is also perpendicular to surfaces of constant phase and is defined as

$$\bar{n} = n_x \bar{a}_x + n_y \bar{a}_y + n_z \bar{a}_z. \quad (2.29)$$

To describe how the constant phase planes propagate, a function can be defined, $f(\beta)$, where β is located on the plane. By letting

$$\beta = t - \frac{1}{v} \bar{n} \cdot \bar{r} \quad (2.30)$$

then for a fixed time $t = t_1$, $\beta = \beta_0$ which equals a constant on the plane defined by

$$\bar{n} \cdot \bar{r} = \text{constant} \quad (2.31)$$

and

$$n_x x + n_y y + n_z z = \text{constant}. \quad (2.32)$$

By taking the same fixed value on another plane at an incremented time $t = t_1 + \Delta t$ and space $\bar{r} = \bar{r}_1 + \Delta \bar{r}$ the following relation is found:

$$\beta_0 = t_1 + \Delta t - \frac{1}{v} \bar{n} \cdot (\bar{r}_1 + \Delta \bar{r}) = t_1 - \frac{1}{v} \bar{n} \cdot \bar{r}_1. \quad (2.33)$$

After simplification, Equation (2.33) becomes

$$v \Delta t = \bar{n} \cdot \Delta \bar{r}. \quad (2.34)$$

From Equation (2.34) it is seen that $\bar{n} \cdot \Delta \bar{r}$ is the distance traveled by the plane of constant phase, which is also the plane wave, during the time increment Δt . This defines the variable v as the velocity of propagation of the plane wave or the phase velocity.

2.1.2 Steady-State Wave Propagation

By studying the steady-state wave several wave parameters can be defined which are useful in describing the characteristics of waves in a dielectric medium. For simplicity the following notation will be used to describe the fields propagating in the medium. The descriptions will be made for a steady-state sinusoidal propagating wave in the electric field but they also apply exactly to the magnetic field. The new notation for the electric field is as follows:

$$\bar{\varepsilon} = \bar{\varepsilon}_x(x,y,z,t)\bar{a}_x + \bar{\varepsilon}_y(x,y,z,t)\bar{a}_y + \bar{\varepsilon}_z(x,y,z,t)\bar{a}_z \quad (2.35)$$

where

$$\bar{\varepsilon}_x(x,y,z,t) = E_{x0}(x,y,z)\cos(\omega t + \phi_x), \quad (2.36)$$

$$\bar{\varepsilon}_y(x,y,z,t) = E_{y0}(x,y,z)\cos(\omega t + \phi_y), \quad (2.37)$$

$$\bar{\varepsilon}_z(x,y,z,t) = E_{z0}(x,y,z)\cos(\omega t + \phi_z), \quad (2.38)$$

and

E_{x0} , E_{y0} , and E_{z0} are real functions of position.

Using the real part of the following complex relation:

$$e^{j(\omega t + \phi)} = \cos(\omega t + \phi) + j\sin(\omega t + \phi). \quad (2.39)$$

Equation (2.36) can be rewritten as

$$\bar{\varepsilon}_x(x,y,z,t) = \operatorname{Re}[E_{x0}(x,y,z)e^{j(\omega t + \phi_x)}]. \quad (2.40)$$

By defining the variable E_x as the space part of Equation (2.40):

$$E_x = E_{x0}(x,y,z)e^{j\phi_x}. \quad (2.41)$$

Equation (2.36) then becomes

$$\bar{\varepsilon}_x(x,y,z,t) = \operatorname{Re}(E_x e^{j\omega t}). \quad (2.42)$$

Using the same procedure for ε_y and ε_z , Equations (2.37) and (2.38) become

$$\varepsilon_y(x,y,z,t) = \operatorname{Re}(E_y e^{j\omega t}) \quad (2.43)$$

and

$$\varepsilon_z(x,y,z,t) = \operatorname{Re}(E_z e^{j\omega t}). \quad (2.44)$$

Substituting Equations (2.42) to (2.44) into Equation (2.35), the simplified form of the electric field equation becomes

$$\bar{\varepsilon} = \operatorname{Re}[(E_x \bar{a}_x + E_y \bar{a}_y + E_z \bar{a}_z) e^{j\omega t}] \quad (2.45)$$

or

$$\bar{\varepsilon} = \operatorname{Re}(\bar{E} e^{j\omega t}). \quad (2.46)$$

In a similar fashion as the derivation of the electric field, the magnetic field equation is found to be

$$\bar{\mathcal{H}} = \operatorname{Re}(\bar{H} e^{j\omega t}). \quad (2.47)$$

Using Equations (2.46) and (2.47), the Maxwell's equations can be derived for a sinusoidal steady-state propagating wave in the optical fiber. By substituting these equations into the constitutive equations (Equations (2.7) to (2.9)) one finds

$$\bar{\mathcal{D}} = \varepsilon(\operatorname{Re}(\bar{E} e^{j\omega t})) \quad (2.48)$$

$$\bar{\mathcal{B}} = \mu(\operatorname{Re}(\bar{H} e^{j\omega t})) \quad (2.49)$$

and

$$\bar{J} = \sigma(\operatorname{Re}(\bar{E}e^{j\omega t})). \quad (2.50)$$

Taking the derivatives of Equations (2.48) and (2.49) with respect to time:

$$\frac{\partial \bar{J}}{\partial t} = j\omega \epsilon(\operatorname{Re}(\bar{E}e^{j\omega t})) \quad (2.51)$$

$$\frac{\partial \bar{B}}{\partial t} = j\omega \mu(\operatorname{Re}(\bar{H}e^{j\omega t})) \quad (2.52)$$

and substituting these equations into Equations (2.3) to (2.6), Maxwell's equations in a simplified form are found:

$$\nabla \times \operatorname{Re}(\bar{E}e^{j\omega t}) = -j\omega \mu(\operatorname{Re}(\bar{H}e^{j\omega t})) \quad (2.53)$$

$$\nabla \times \operatorname{Re}(\bar{H}e^{j\omega t}) = \sigma(\operatorname{Re}(\bar{E}e^{j\omega t})) + j\omega \epsilon(\operatorname{Re}(\bar{E}e^{j\omega t})) \quad (2.54)$$

$$\nabla \cdot \mu(\operatorname{Re}(\bar{H}e^{j\omega t})) = 0 \quad (2.55)$$

and

$$\nabla \cdot \epsilon(\operatorname{Re}(\bar{E}e^{j\omega t})) = \rho. \quad (2.56)$$

Since the optical fiber is assumed to be a charge-free lossless dielectric, the conductivity (σ) and the charge density (ρ) are zero so Maxwell's equations become

$$\nabla \times \operatorname{Re}(\bar{E}) = -j\omega \mu(\operatorname{Re}(\bar{H})) \quad (2.57)$$

$$\nabla \times \operatorname{Re}(\bar{H}) = j\omega \epsilon(\operatorname{Re}(\bar{E})) \quad (2.58)$$

$$\nabla \cdot \operatorname{Re}(\bar{H}) = 0 \quad (2.59)$$

$$\nabla \cdot \operatorname{Re}(\bar{E}) = 0. \quad (2.60)$$

These are the equations for a charge-free, lossless, linear isotropic material with a sinusoidal steady-state propagating wave.

Using Equations (2.57) to (2.60) and applying the same procedure used to find the wave equation for any type propagation (Equations (2.22) and (2.23)) the wave equations for a sinusoidal steady-state wave are found:

$$\nabla^2(\text{Re}(\bar{E})) + \mu\epsilon\omega^2(\text{Re}(\bar{E})) = 0 \quad (2.61)$$

and

$$\nabla^2(\text{Re}(\bar{H})) + \mu\epsilon\omega^2(\text{Re}(\bar{H})) = 0. \quad (2.62)$$

By letting $k^2 = \mu\epsilon\omega^2$ and substituting back into Equations (2.61) and (2.62), the wave equations for a sinusoidal steady-state are found. These are also known as the Helmholtz equations:

$$\nabla^2(\text{Re}(\bar{E})) + k^2(\text{Re}(\bar{E})) = 0 \quad (2.63)$$

and

$$\nabla^2(\text{Re}(\bar{H})) + k^2(\text{Re}(\bar{H})) = 0 \quad (2.64)$$

where

$$k = \omega\sqrt{\mu\epsilon} = \frac{\omega}{v}. \quad (2.65)$$

By giving the scalar value k a direction, a propagating vector can be defined such that

$$\bar{k} = k\bar{n} = \frac{\omega}{v}\bar{n} \quad (2.66)$$

where \bar{n} defines the direction of propagation of a wave. Now with \bar{k} in place of k , the solutions of Equations (2.63) and (2.64) are propagating waves. An example of the electric field component in x is

$$\text{Re}(E_x) = \text{Re}(E_x^+ e^{-j\bar{k} \cdot \bar{r}}) + \text{Re}(E_x^- e^{+j\bar{k} \cdot \bar{r}}). \quad (2.67)$$

The actual component solutions for Equations (2.63) and (2.64) have the form:

$$\psi = A^+ \cos(\omega t - k \bar{n} \cdot \bar{r}) + A^- \cos(\omega t + k \bar{n} \cdot \bar{r}). \quad (2.68)$$

Equation (2.68) says that there are two plane waves propagating in the $\pm \bar{n}$ directions. This equation is the same as Equation (2.27) except that now the propagation of the wave is sinusoidal in form.

2.1.3 Wave Parameters

Wave parameters basically descriptive terms for how waves travel through a given medium. In most cases these parameters are referenced to constant properties found in free space conditions. Comparisons of how waves travel through different mediums are made through these parameters.

To describe how a plane wave propagates through a medium only one propagation direction needs to be studied so Equation (2.68) can be reduced to

$$\psi = A \cos(\omega t - \bar{k} \cdot \bar{r}) \quad (2.69)$$

for a plane wave propagating in the $+n$ direction. On a surface of constant phase, if the plane wave is advanced one wavelength and it is required that ψ completes one cycle as \bar{r} changes to $\bar{r} + \Delta\bar{r}$, then $\bar{r} + \Delta\bar{r} = \bar{r} + \lambda\bar{n}$ or

$$\Delta\bar{r} = \lambda\bar{n}. \quad (2.70)$$

Since the phase is constant, from Equation (2.69) it is found that

$$\omega t - \bar{k} \cdot \bar{r} = \omega t + 2\pi - \bar{k} \cdot (\bar{r} + \Delta\bar{r}), \quad (2.71)$$

and by substituting Equation (2.70) into (2.71) it is found that

$$\omega t - \bar{k} \cdot \bar{r} = \omega t + 2\pi - \bar{k} \cdot (\bar{r} + \lambda\bar{n}) \quad (2.72)$$

which, after canceling like terms and solving for k , becomes

$$k = \frac{2\pi}{\lambda} = \frac{\omega}{v} \quad (2.73)$$

where λ = the spatial wavelength in the medium,

v = Phase velocity of the wave in the medium,

and

k = the wave number.

These terms, defined in free space parameters are found to be

$$v = \frac{1}{\sqrt{\mu_0 \epsilon}} = \frac{c}{\sqrt{\epsilon_r}} = \frac{c}{n} \quad (2.74)$$

$$\lambda = \frac{2\pi v}{\omega} = \frac{2\pi c}{\omega n} = \frac{c}{f} \frac{1}{n} = \frac{\lambda_0}{n} \quad (2.75)$$

$$k = \frac{2\pi}{\lambda} = \frac{2\pi}{\lambda_0} n = nk_0 \quad (2.76)$$

where $c = \frac{\sqrt{\epsilon_0}}{\sqrt{\mu_0}}$ = speed of light in free space, m/s

$n = \sqrt{\epsilon_r}$ = index of refraction,

and

$$f = \frac{\omega}{2\pi} = \text{frequency in cycles/sec.}$$

2.1.4 Waveguide Equations

The waveguide equations are useful in describing how energy travels through a dielectric medium. From these equations various properties of light propagation can be found such as the proper conditions needed to guide energy, which "modes" of energy can propagate, and what determines whether or not they will propagate. A mode is an allowable field configuration which satisfies Maxwell's equations and the boundary conditions for the system.

For the analysis of dielectric waveguides the direction of propagation, which is the longitudinal axis of the guide, will be denoted as the z direction. Recalling that \vec{k} is the propagation vector for a general waveguide, β will be defined as the longitudinal component of this propagation vector. Since z is the longitudinal direction, the x and y directions will be perpendicular to the propagation direction and are called the transverse directions. For an optical fiber, the index of refraction usually varies in the x and y

directions due to having a cladding and a core, but is constant along the length of the fiber (z direction). Since the permittivity is related to the index of refraction, it is a function of x and y only, therefore

$$\epsilon = \epsilon(x, y). \quad (2.77)$$

From a similar notation as Equation (2.67), the fields in the waveguide can be written as

$$\bar{E} = \bar{E}_0(x, y)e^{-j\beta z} \quad (2.78)$$

and

$$\bar{H} = \bar{H}_0(x, y)e^{-j\beta z} \quad (2.79)$$

with the use of the assumptions stated above.

Substituting Equations (2.78) and (2.79) into Maxwell's equations (Equations (2.57) and (2.58)) and using the Del identity:

$$\nabla \times F = \left(\frac{\partial F_z}{\partial y} - \frac{\partial F_y}{\partial z} \right) i + \left(\frac{\partial F_x}{\partial z} - \frac{\partial F_z}{\partial x} \right) j + \left(\frac{\partial F_y}{\partial z} - \frac{\partial F_z}{\partial y} \right) k. \quad (2.80)$$

Maxwell's equations (Equations (2.57) and (2.58)) in expanded form are found to be

$$\begin{aligned} & \left(\frac{\partial E_z}{\partial y} - \frac{\partial E_y}{\partial z} \right) \bar{a}_x + \left(\frac{\partial E_x}{\partial z} - \frac{\partial E_z}{\partial x} \right) \bar{a}_y + \left(\frac{\partial E_y}{\partial z} - \frac{\partial E_z}{\partial y} \right) \bar{a}_z \\ &= -\mu \frac{\partial H_x}{\partial t} \bar{a}_x - \mu \frac{\partial H_y}{\partial t} \bar{a}_y - \mu \frac{\partial H_z}{\partial t} \bar{a}_z \end{aligned} \quad (2.81)$$

and

$$\begin{aligned} & \left(\frac{\partial H_z}{\partial y} - \frac{\partial H_y}{\partial z} \right) \bar{a}_x + \left(\frac{\partial H_x}{\partial z} - \frac{\partial H_z}{\partial x} \right) \bar{a}_y + \left(\frac{\partial H_y}{\partial x} - \frac{\partial H_x}{\partial y} \right) \bar{a}_z \\ &= \varepsilon \frac{\partial E_x}{\partial t} \bar{a}_x + \varepsilon \frac{\partial E_y}{\partial t} \bar{a}_y + \varepsilon \frac{\partial E_z}{\partial t} \bar{a}_z. \end{aligned} \quad (2.82)$$

It is a valid assumption that the electric and magnetic fields are varying with time by $e^{j\omega t}$. Using this assumption and partial derivatives from Equations (2.78) and (2.79), Equations (2.81) and (2.82) can be written in terms of the longitudinal electric and magnetic fields only. The partial derivatives used in these equations are found to be

$$\frac{\partial E_x}{\partial t} = j\omega E_x \quad \frac{\partial E_y}{\partial t} = j\omega E_y \quad \frac{\partial E_z}{\partial t} = j\omega E_z \quad (2.83a)$$

$$\frac{\partial H_x}{\partial t} = j\omega H_x \quad \frac{\partial H_y}{\partial t} = j\omega H_y \quad \frac{\partial H_z}{\partial t} = j\omega H_z \quad (2.83b)$$

$$\frac{\partial E_y}{\partial z} = -j\beta E_y \quad \frac{\partial E_x}{\partial z} = -j\beta E_x \quad (2.83c)$$

$$\frac{\partial H_y}{\partial z} = -j\beta H_y \quad \frac{\partial H_x}{\partial z} = -j\beta H_x. \quad (2.83d)$$

By substituting Equations (2.83a) to (2.83d) into Equations (2.81) and (2.82), the following equations, in component form, are found:

$$\frac{\partial H_z}{\partial y} + j\beta H_y = j\omega \varepsilon E_x, \quad (2.84a)$$

$$-\frac{\partial H_z}{\partial x} - j\beta H_x = j\omega \varepsilon E_y, \quad (2.84b)$$

$$\frac{\partial H_y}{\partial x} - \frac{\partial H_x}{\partial y} = j\omega\epsilon E_z, \quad (2.84c)$$

$$\frac{\partial E_z}{\partial y} + j\beta E_y = -j\omega\mu H_x, \quad (2.85a)$$

$$\frac{\partial E_z}{\partial x} - j\beta E_x = -j\omega\mu H_y, \quad (2.85b)$$

and

$$\frac{\partial E_y}{\partial x} - \frac{\partial E_x}{\partial y} = -j\omega\mu H_z. \quad (2.85c)$$

Using the components in Equations (2.84) and (2.85), a modified wave equation can be found which is in terms of the longitudinal electric and magnetic fields only. These equations will be used to analyze the dielectric waveguides.

The process of obtaining wave equations as a function of the propagation direction fields is as follows.

Substituting Equation (2.85b) into (2.84a) and arranging it is found that

$$(j\omega\epsilon + \frac{-j\beta^2}{\omega\mu})E_x = \frac{\partial H_z}{\partial y} + \frac{\beta}{\omega\mu} \frac{\partial E_z}{\partial x}. \quad (2.86)$$

Multiplying both sides of Equation (2.86) by $-j\omega\mu$ results in

$$(\omega^2\mu\epsilon - \beta^2)E_x = -j(\omega\mu \frac{\partial H_z}{\partial y} + \beta \frac{\partial E_z}{\partial x}) \quad (2.87)$$

and by letting $K^2 = k^2 - \beta^2$ and recalling that $k^2 = \omega^2\mu\epsilon$, Equation (2.87) becomes

$$E_x = \frac{-j}{K^2} (\omega\mu \frac{\partial H_z}{\partial y} + \beta \frac{\partial E_z}{\partial x}) \quad (2.88)$$

Similar substitutions of Equations (2.84) and (2.85) yield the other field solutions:

$$E_y = \frac{-j}{K^2} (\beta \frac{\partial E_z}{\partial y} - \omega\mu \frac{\partial H_z}{\partial x}), \quad (2.89)$$

$$H_x = \frac{-j}{K^2} (\beta \frac{\partial H_z}{\partial x} - \omega\varepsilon \frac{\partial E_z}{\partial y}), \quad (2.90)$$

and

$$H_y = \frac{-j}{K^2} (\beta \frac{\partial H_z}{\partial y} + \omega\varepsilon \frac{\partial E_z}{\partial x}). \quad (2.91)$$

By substituting Equations (2.88) to (2.91) into Equations (2.84c) and (2.85c), the wave equations are found which are functions of the longitudinal field only:

$$\frac{-j}{K^2} \beta \frac{\partial^2 H_z}{\partial x \partial y} - \frac{j}{K^2} \omega\varepsilon \frac{\partial^2 E_z}{\partial x^2} + \frac{j}{K^2} \beta \frac{\partial^2 H_z}{\partial x \partial y} - \frac{j}{K^2} \omega\varepsilon \frac{\partial^2 E_z}{\partial y^2} = j\omega\varepsilon E_z. \quad (2.92)$$

By multiplying both sides of Equation (2.92) by $jK^2/\omega\varepsilon$, the modified wave equation for the electric field is found to be

$$\frac{\partial^2 E_z}{\partial x^2} + \frac{\partial^2 E_z}{\partial y^2} + K^2 E_z = 0. \quad (2.93)$$

In a similar manner, the equation for the magnetic field is found to be

$$\frac{\partial^2 H_z}{\partial x^2} + \frac{\partial^2 H_z}{\partial y^2} + K^2 H_z = 0. \quad (2.94)$$

Equations (2.93) and (2.94) are uncoupled equations which describe the fields in a waveguide. Coupling of the fields in the two equations occurs by applying the boundary conditions. If the boundary conditions do not achieve coupling of the specific longitudinal components we can obtain solutions where the longitudinal electric component or the longitudinal magnetic component is equal to zero. These solutions define the modes which can propagate in the dielectric guide. Table 2.1 gives the types of modes and the values of their longitudinal components.

Table 2.1 Types of propagating modes in a dielectric

TEM(transverse electromagnetic)	$E_z = 0, H_z = 0$
TE(transverse electric)	$E_z = 0, H_z \neq 0$
TM(transverse magnetic)	$E_z \neq 0, H_z = 0$
HE or EH (hybrid)	$E_z \neq 0, H_z \neq 0$

The formulation up to this point was in rectangular coordinates due to the ease in understanding the simpler equations. There is no loss in generality by formulating the equations this way and then converting to cylindrical coordinates. The last part of the derivation used to find Equations (2.93) and (2.94) will be repeated using equations in cylindrical coordinates since the dielectric in question has a round cross section. The derivation in cylindrical coordinates will begin by transforming Equations (2.88) to (2.91) and then solving for the modified wave equation.

In general, when one set of axes is rotated an angle ϕ from another set, the two are related by

$$F_{x1} = F_x \cos \phi + F_y \sin \phi \quad (2.95)$$

and

$$F_{y1} = -F_x \sin \phi + F_y \cos \phi. \quad (2.96)$$

To convert from the x-y coordinate system to the r- ϕ system, x1 and y1 in Equations (2.95) and (2.96) are replaced by r and ϕ , respectively. For the electric field in a dielectric waveguide the following relations are found:

$$E_r = E_x \cos \phi + E_y \sin \phi \quad (2.97)$$

and

$$E_\phi = -E_x \sin \phi + E_y \cos \phi. \quad (2.98)$$

From trigonometry it is also found that

$$x = r \cos \phi \quad y = r \sin \phi \quad (2.99)$$

and

$$r = \sqrt{x^2 + y^2} \quad \phi = \arctan(y/x). \quad (2.100)$$

A substitution of Equations (2.88) and (2.89) into Equation (2.97) leads to

$$E_r = \frac{-j}{K^2} (\omega\mu \frac{\partial H_z}{\partial y} \cos\phi + \beta \frac{\partial E_z}{\partial x} \cos\phi + \beta \frac{\partial E_z}{\partial y} \sin\phi - \omega\mu \frac{\partial H_z}{\partial x} \sin\phi). \quad (2.101)$$

The chain rules for relating rectangular and cylindrical coordinates are

$$\frac{\partial f}{\partial x} = \frac{\partial f}{\partial r} \frac{\partial r}{\partial x} + \frac{\partial f}{\partial \phi} \frac{\partial \phi}{\partial x} \quad \frac{\partial f}{\partial y} = \frac{\partial f}{\partial r} \frac{\partial r}{\partial y} + \frac{\partial f}{\partial \phi} \frac{\partial \phi}{\partial y}. \quad (2.102)$$

From Equations (2.99) and (2.100), the proper partial derivatives are found which are used in the chain rules in order to transform Equation (2.101) to cylindrical coordinates.

These are found to be

$$\frac{\partial r}{\partial x} = \frac{x}{r} = \cos\phi \quad \frac{\partial r}{\partial y} = \frac{y}{r} = \sin\phi \quad (2.103)$$

$$\frac{\partial \phi}{\partial x} = \frac{-y}{r^2} = \frac{-\sin\phi}{r} \quad \frac{\partial \phi}{\partial y} = \frac{x}{r^2} = \frac{\cos\phi}{r}. \quad (2.104)$$

By substituting Equations (2.103) and (2.104) into Equation (2.102) and using the result in Equation (2.101), the following expression is obtained for the electric field in the radial direction:

$$\begin{aligned}
E_r = & \frac{-j}{K^2} \left\{ \omega\mu \left[\frac{\partial H_z}{\partial r} \sin \phi + \frac{\partial H_z}{\partial \phi} \left(\frac{\cos \phi}{r} \right) \right] \cos \phi \right. \\
& + \beta \left[\frac{\partial E_z}{\partial r} \cos \phi + \frac{\partial E_z}{\partial \phi} \left(\frac{-\sin \phi}{r} \right) \right] \cos \phi \\
& + \beta \left[\frac{\partial E_z}{\partial r} \sin \phi + \frac{\partial E_z}{\partial \phi} \left(\frac{\cos \phi}{r} \right) \right] \sin \phi \\
& \left. - \omega\mu \left[\frac{\partial H_z}{\partial r} \cos \phi + \frac{\partial H_z}{\partial \phi} \left(\frac{-\sin \phi}{r} \right) \right] \sin \phi \right\} \quad (2.105)
\end{aligned}$$

which simplifies to

$$E_r = \frac{-j}{K^2} \left(\beta \frac{\partial E_z}{\partial r} + \omega\mu \frac{1}{r} \frac{\partial H_z}{\partial \phi} \right). \quad (2.106)$$

Using the same procedure for the electric field in the transverse direction and for the magnetic field it is found that

$$E_\phi = \frac{-j}{K^2} \left(\beta \frac{1}{r} \frac{\partial E_z}{\partial \phi} - \omega\mu \frac{\partial H_z}{\partial r} \right), \quad (2.107)$$

$$H_r = \frac{-j}{K^2} \left(\beta \frac{\partial H_z}{\partial r} - \omega\epsilon \frac{1}{r} \frac{\partial E_z}{\partial \phi} \right), \quad (2.108)$$

and

$$H_\phi = \frac{-j}{K^2} \left(\beta \frac{1}{r} \frac{\partial H_z}{\partial \phi} + \omega\epsilon \frac{\partial E_z}{\partial r} \right). \quad (2.109)$$

In the same manner as Equations (2.88) to (2.91) were used to find the waveguide equations in rectangular coordinates, Equations (2.106) to (2.109) are used to find the waveguide equations in cylindrical coordinates. These equations are found to be

$$\frac{\partial^2 E_z}{\partial r^2} + \frac{1}{r} \frac{\partial E_z}{\partial r} + \frac{1}{r^2} \frac{\partial^2 E_z}{\partial \phi^2} + K^2 E_z = 0 \quad (2.110)$$

and

$$\frac{\partial^2 H_z}{\partial r^2} + \frac{1}{r} \frac{\partial H_z}{\partial r} + \frac{1}{r^2} \frac{\partial^2 H_z}{\partial \phi^2} + K^2 H_z = 0. \quad (2.111)$$

The waveguide equations above can now be solved for their electric and magnetic fields in order to describe the properties of light propagation through a round optical fiber.

2.1.5 Step-Index Optical Fiber

From the previous work the waveguide equations were found in cylindrical coordinates for a round dielectric medium or an optical fiber. By treating these equations as a boundary valued problem they can be solved by the use of boundary conditions. These boundary conditions are obtained from the core-cladding interface of an optical fiber. As with any boundary valued problem, by applying the boundary conditions, the characteristic equation is obtained for a specific configuration. This characteristic equation allows the formulation of the properties of the optical fiber such as the specific propagation constants and the modes of light which can propagate in the waveguide. From these, properties such as mode cutoff parameters and the number of modes which can propagate for a given fiber configuration are obtained. This allows a better understanding of the design of the optical fibers and how they are categorized.

The analysis begins by applying the method of separation of variables to Equations (2.110) and (2.111). Assuming a solution for the electric field in which r and ϕ are independent it is found that

$$E_z(\phi, r) = A \phi(\phi) F(r). \quad (2.112)$$

Since the cross section of the optical fiber has circular symmetry, a circular function is chosen for $\phi(\phi)$, specifically

$$\phi(\phi) = e^{j\nu\phi}; \quad (2.113)$$

therefore Equation (2.112) becomes

$$E_z = A F(r) e^{j\nu\phi}. \quad (2.114)$$

From Equation (2.114), the required derivatives to be used in Equation (2.110) are

$$\frac{\partial E_z}{\partial r} = A e^{j\nu\phi} \frac{dF(r)}{dr}, \quad (2.115)$$

$$\frac{\partial^2 E_z}{\partial r^2} = A e^{j\nu\phi} \frac{d^2 F(r)}{dr^2}, \quad (2.116)$$

and

$$\frac{\partial^2 E_z}{\partial \phi^2} = -A \nu^2 e^{j\nu\phi} F(r). \quad (2.117)$$

Substituting Equations (2.115) to (2.117) into Equation (2.110) and multiplying by $1/Ae^{j\nu\phi}$, the solution of the waveguide equation is

$$\frac{d^2F(r)}{dr^2} + \frac{1}{r} \frac{dF(r)}{dr} + (\kappa^2 - \frac{\nu^2}{r^2})F(r) = 0. \quad (2.118)$$

The solution is in the form of a Bessel's equation. Since there are many solutions which satisfy Bessel's equations conditions which limit the solutions must be defined. For an optical fiber, the electric and magnetic fields must be finite in the core area of the fiber. Also these fields must decay in the cladding so that they are not guided for long lengths since this is the purpose of the cladding. The constraints are therefore chosen where the fields are finite at the center of the core ($r = 0$) and that the fields decay exponentially in the cladding at large radii from the center of the fiber.

The Bessel function of the first kind, $J_\nu(x)$, is a function which is finite at the origin so it is chosen as a solution to Equation (2.118) for radii smaller than the core radius:

$$F(r) = J_\nu(\kappa r) \quad \text{for } r < a; \quad (2.119)$$

therefore the fields inside the core are given as

$$E_z = AJ_\nu(\kappa r)e^{j\nu\phi} \quad \text{for } r < a \quad (2.120)$$

and

$$H_z = BJ_\nu(\kappa r)e^{j\nu\phi} \quad \text{for } r < a. \quad (2.121)$$

For the fields in the cladding a modified Hankel function of the first kind, $H(jx)$, is chosen as the solution since it has the exponentially decaying properties required to represent the cladding. This decay is in the form of $e^{-\gamma r}$ and by letting $K = j\gamma$ for simplicity, it is found that

$$E_z = CH_{\nu}^{(1)}(j\gamma r)e^{j\nu\phi} \quad \text{for } r > a \quad (2.122)$$

and

$$H_z = DH_{\nu}^{(1)}(j\gamma r)e^{j\nu\phi} \quad \text{for } r > a. \quad (2.123)$$

Recalling that Equations (2.106) to (2.109) define the electric and magnetic fields in cylindrical coordinates, these can be used to find the unknown constants in Equations (2.120) to (2.123) and thus describe the transverse fields in the optical fiber for the core and cladding.

For the core, to get Equation (2.106) into functions of the unknown constants, Equations (2.120) and (2.121) must be differentiated with respect to r and ϕ to obtain the proper terms for substitution:

$$\frac{\partial E_r}{\partial r} = A K J'_{\nu}(Kr) e^{j\nu\phi} \quad (2.124)$$

where

$$J'_{\nu}(Kr) = \frac{\partial J_{\nu}(Kr)}{\partial (Kr)} \quad (2.125)$$

and

$$\frac{\partial H_z}{\partial \phi} = B(j\nu) J_{\nu}(Kr) e^{j\nu\phi}. \quad (2.126)$$

By substituting Equations (2.124) and (2.126) into Equation (2.106) one obtains

$$E_r = \frac{-j}{K^2} [A\beta K J'_v(Kr) e^{j\nu\phi} + B(j\nu)(\omega\mu) \frac{1}{r} J_v(Kr) e^{j\nu\phi}]. \quad (2.127)$$

In a similar manner, using Equations (2.107) to (2.109) it is found that

$$E_\phi = \frac{-j}{K^2} [j\beta \frac{\nu}{r} A J_v(Kr) - K\omega\mu B J'_v(Kr)] e^{j\nu\phi}, \quad (2.128)$$

$$H_r = \frac{-j}{K^2} [-j\omega\epsilon_1 \frac{\nu}{r} A J_v(Kr) + K\beta B J'_v(Kr)] e^{j\nu\phi}, \quad (2.129)$$

and

$$H_\phi = \frac{-j}{K^2} [K\omega\epsilon_1 A J'_v(Kr) + j\beta \frac{\nu}{r} B J_v(Kr)] e^{j\nu\phi} \quad (2.130)$$

where

$$K^2 = k_1^2 - \beta^2 \quad (2.131)$$

and

$$k_1^2 = \omega^2 \mu_0 \epsilon_1. \quad (2.132)$$

Equations (2.127) to (2.130) give the transverse electric and magnetic fields in the core of the optical fiber. A similar procedure is used to obtain the fields in the cladding.

For the transverse fields in the cladding, Equations (2.122) and (2.123) are differentiated with respect to r and ϕ and substituted into Equations (2.106) to (2.109). The results obtained from this procedure are as follows for the cladding fields ($r > a$):

$$E_r = \frac{-1}{\gamma^2} [\beta \gamma C H_\nu^{(1)}(j\gamma) + \omega \mu_0 \frac{\nu}{r} D H_\nu^{(1)}(j\gamma)] e^{j\nu\phi}, \quad (2.133)$$

$$E_\phi = \frac{-1}{\gamma^2} [\beta \frac{\nu}{r} C H_\nu^{(1)}(j\gamma) - \gamma \omega \mu_0 \frac{\nu}{r} D H_\nu^{(1)}(j\gamma)] e^{j\nu\phi}, \quad (2.134)$$

$$H_r = \frac{-1}{\gamma^2} [-\omega \epsilon_2 \frac{\nu}{r} C H_\nu^{(1)}(j\gamma) + \gamma \beta D H_\nu^{(1)}(j\gamma)] e^{j\nu\phi}, \quad (2.135)$$

and

$$H_\phi = \frac{-1}{\gamma^2} [\gamma \omega \epsilon_2 C H_\nu^{(1)}(j\gamma) + \beta \frac{\nu}{r} D H_\nu^{(1)}(j\gamma)] e^{j\nu\phi} \quad (2.136)$$

where

$$H_\nu^{(1)}(j\gamma) = \frac{\partial H_\nu^{(1)}(j\gamma)}{\partial(j\gamma)}, \quad (2.137)$$

$$\gamma^2 = \beta^2 - k_2^2, \quad (2.138)$$

and

$$k_2^2 = \omega^2 \mu_0 \epsilon_2. \quad (2.139)$$

The electric and magnetic fields in both the core and cladding are described by Equations (2.127) to (2.130) and Equations (2.133) to (2.136). The constants A, B, C, D, and β will be found by the boundary conditions for the tangential components of the fields at the core/cladding interface ($r = a$). At the interface these boundary conditions are found to be

$$E_z_1 = E_z_2 \quad E_\phi_1 = E_\phi_2 \quad H_z_1 = H_z_2 \quad H_\phi_1 = H_\phi_2 \quad (2.140)$$

at $r = a$.

Using Equations (2.120) and (2.122) and the first boundary condition in Equation (2.140) yields the first of four simultaneous equations which can be used to solve for the unknowns:

$$J_\nu(Ka)A - H_\nu^{(1)}(j\gamma a)C = 0. \quad (2.141)$$

Substituting $r = a$ into Equations (2.128) and (2.134) and equating by use of Equation (2.140) gives

$$\begin{aligned} & \left(\frac{\beta}{K^2} \frac{\nu}{a}\right) J_\nu(Ka)A + j \frac{\omega\mu_0}{K} J'_\nu(Ka)B \\ & + \left(\frac{\beta}{\gamma^2} \frac{\nu}{a}\right) H_\nu^{(1)}(j\gamma a)C - \frac{\omega\mu_0}{\gamma} H'_\nu(j\gamma a)D = 0 \end{aligned} \quad (2.142)$$

which is the second simultaneous equation.

The third equation is found by using Equations (2.121) and (2.123) and the boundary conditions

$$J_\nu(Ka)B - H_\nu^{(1)}(j\gamma a)D = 0. \quad (2.143)$$

The fourth simultaneous equation is obtained by Equations (2.130) and (2.136) with $r = a$:

$$\begin{aligned} & \left(\frac{-j\omega\varepsilon_1}{K}\right) J'_\nu(Ka)A + \left(\frac{\beta}{K^2} \frac{\nu}{a}\right) J_\nu(Ka)B \\ & + \left(\frac{\omega\varepsilon_2}{\gamma}\right) H'_\nu(j\gamma a)C + \left(\frac{\beta}{\gamma^2} \frac{\nu}{a}\right) H_\nu^{(1)}(j\gamma a)D = 0 \end{aligned} \quad (2.144)$$

Equations (2.141) to (2.144) are four simultaneous equations which provide a nontrivial solution as long as their determinant is equal to zero. The determinant of this system given by Equation (2.145) results in the characteristic equation for the waveguide.

$$\begin{aligned} & \left[\frac{\varepsilon_1}{\varepsilon_2} \frac{a\gamma^2}{K} \frac{J'_\nu(Ka)}{J_\nu(Ka)} + j\gamma a \frac{H_\nu^{(1)}(j\gamma a)}{H_\nu^{(1)}(j\gamma a)} \right] \left[\frac{a\gamma^2}{K} \frac{J'_\nu(Ka)}{J_\nu(Ka)} + j\gamma a \frac{H_\nu^{(1)}(j\gamma a)}{H_\nu^{(1)}(j\gamma a)} \right] \\ & = \left[\nu \left(\frac{\varepsilon_1}{\varepsilon_2} - 1 \right) \frac{\beta k_2}{K^2} \right]^2 \end{aligned} \quad (2.145)$$

Also Equations (2.141) to (2.144) can be combined so that the unknowns A, B, C, and D are in terms of each other. Coefficients A and C and B and D are found to be related by

$$C = \frac{J_\nu(Ka)}{H_\nu^{(1)}(j\gamma a)} A \quad (2.146)$$

and

$$D = \frac{J_\nu(Ka)}{H_\nu^{(1)}(j\gamma a)} B. \quad (2.147)$$

Using Equations (2.146) and (2.147) in Equation (2.142) the coefficient B is obtained as a function of A:

$$B = \frac{j}{\nu} \frac{aK\gamma[\varepsilon_1\gamma J'_\nu(Ka)H_\nu^{(1)}(j\gamma a) + j\varepsilon_2 K J_\nu(Ka) H_\nu^{(1)}(j\gamma a)]}{\omega(\varepsilon_1 - \varepsilon_2)\mu_0\beta J_\nu(Ka)H_\nu^{(1)}(j\gamma a)} A. \quad (2.148)$$

A relation of coefficients A and B can also be found by using Equation (2.144) instead of Equation (2.142):

$$B = j\nu \frac{\omega(\epsilon_1 - \epsilon_2)\beta J_\nu(Ka)H_\nu^{(1)}(j\gamma a)}{K\gamma a[\gamma J'_\nu(Ka)H_\nu^{(1)}(j\gamma a) + jKJ_\nu(Ka)H_\nu^{(1)}(j\gamma a)]} A. \quad (2.149)$$

Equations (2.148) and (2.149) will become important in determining which modes propagate in the optical fiber.

2.1.6 Modes in an Optical Fiber

By solving Equation (2.145) the different types of modes which propagate in the optical fiber can be obtained. For a dielectric waveguide such as an optical fiber, the cross section is circular so there are four general types of modes in which the light can propagate. These are: the transverse electric mode, the transverse magnetic mode, and two hybrid modes which contain longitudinal electric and magnetic field components. The transverse modes are denoted as TE and TM modes for the transverse electric and transverse magnetic modes, respectively. The two hybrid modes are denoted as HE and EH. A special case, where the only modes propagating are the TE and TM modes, occurs when ν is equal to zero.

From the definition of the TE mode it is known that the component of the electric field in the z direction is zero. If this is true, then from Equation (2.120), the coefficient A must also be zero. From Equations (2.141) to (2.145) it is seen that if $E_z = 0$ then Equation (2.141) is omitted since the field component is zero and the boundary condition is no longer important. Letting the coefficient A and the value of ν equal zero in the remaining simultaneous equations and solving for the determinant the characteristic equation for the TE modes is found:

$$\frac{1}{K} \frac{J_0'(Ka)}{J_0(Ka)} + j \frac{1}{\gamma} \frac{H_0^{(1)}(j\gamma a)}{H_0^{(1)}(j\gamma a)} = 0. \quad (2.150)$$

From the general relations for Bessel functions it is known that

$$Z'_0 = -Z_1; \quad (2.151)$$

therefore Equation (2.150) becomes

$$\frac{1}{K} \frac{J_1(Ka)}{J_0(Ka)} + j \frac{1}{\gamma} \frac{H_1^{(1)}(j\gamma a)}{H_0^{(1)}(j\gamma a)} = 0. \quad (2.152)$$

Equation (2.152) is the characteristic equation for the TE mode of propagation. Note that if both sides of Equation (2.152) are multiplied by $\gamma^2 a$ the second bracket of Equation (2.145) would be obtained when $\nu = 0$. In a similar manner the characteristic equation for the TM mode is found to be

$$\frac{\epsilon_1}{\epsilon_2} \frac{1}{K} \frac{J_1(Ka)}{J_0(Ka)} + j \frac{1}{\gamma} \frac{H_1^{(1)}(j\gamma a)}{H_0^{(1)}(j\gamma a)} = 0. \quad (2.153)$$

Comparing Equations (2.145) and (2.153) it is seen that Equation (2.153) is the first bracket on the left-hand side of Equation (2.145) with $\nu = 0$.

Equations (2.145), (2.152), and (2.153) are the characteristic equations used to describe the propagation of the different modes in an optical fiber. Although all of the different modes can propagate in the optical fiber, there are limitations which determine what modes will be guided and which will be lost. These limitations are called the cutoff parameters and they apply to all modes propagating in the optical fiber.

2.1.7 Cutoff Conditions for Propagating Modes

Each mode in the optical fiber is subject to certain conditions which determine whether or not it will be guided. These are called cutoff conditions. Although a mode is guided, the energy is not confined to the core of the fiber. There is a field which enters the cladding and decays with increasing radius. This part of the guided mode is due to the total internal reflection at the core/cladding interface and is called an "evanescent field" due to its decaying nature.

A mode is said to be cutoff when the field in the cladding is no longer evanescent and will not decay. In other words the mode cannot be guided by the fiber and becomes a radiating mode into the cladding which keeps the cladding field from decaying. The rate of decay in the cladding is determined by the parameter γ since the modified Hankel functions are a function of it and the fields in the cladding are dependent of the Hankel function. For large values γ the Hankel function has a small value so the fields in the cladding are small. This means that the fields are concentrated around the center of the core. As the value of γ is reduced, the exponential nature of the Hankel function increases its value so the fields in the cladding are increased. At $\gamma = 0$ the modified Hankel function is infinite so the fields in the cladding are infinite and will no longer decay. This is the description of a mode which has been cutoff therefore it can be said that a mode is cutoff when $\gamma = 0$.

Using Equation (2.138) with the cutoff conditions it is found that

$$\gamma_c = 0 = \sqrt{(\beta_c^2 - k_{2c}^2)}. \quad (2.154)$$

Which, after simplification, yields

$$\beta_c^2 = k_{2c}^2 \quad (2.155)$$

where

$$k_{2c}^2 = \omega_c^2 \mu_0 \epsilon_2. \quad (2.156)$$

Similarly for the core the cutoff conditions yield

$$\kappa_c^2 = k_{1c}^2 - \beta_c^2 \quad (2.157)$$

where

$$k_{1c}^2 = \omega_c^2 \mu_0 \epsilon_1. \quad (2.158)$$

The subscripts 1 and 2 denote the core and the cladding respectively. By substituting Equation (2.155) into Equation (2.157) the following is obtained:

$$\kappa_c^2 = k_{1c}^2 - k_{2c}^2 = \omega_c^2 \mu_0 (\epsilon_1 - \epsilon_2). \quad (2.159)$$

By manipulating Equation (2.159) the relation for the cutoff frequency is found to be

$$\omega_c = \frac{\kappa_c}{\sqrt{\mu_0 (\epsilon_1 - \epsilon_2)}}. \quad (2.160)$$

From Equation (2.160) it is seen that the cutoff frequency can be equal to zero if K is equal to zero. This says there exists at least one mode which will propagate at any frequency except zero. The hybrid HE_{11} mode is this mode and it is the only mode which can propagate at any frequency greater than zero. Since all other modes have a cutoff frequency greater than zero it is possible to design an optical fiber with only one mode propagating. By choosing a specific frequency to be guided, the optical fiber is designed so that this frequency is below the lowest cutoff frequency of the modes other than the HE_{11} mode. This type of fiber is called a singlemode optical fiber.

In order to determine when only one mode is guided in an optical fiber, the cutoff conditions for the other modes must be found. This is accomplished by solving the characteristic Equation (Equation (2.145)) using the parameters for each type of mode. The equation can be written in a simplified form by using identities for the Bessel and Hankel functions and the following notation:

$$J^+ = \frac{1}{Ka} \frac{J_{\nu+1}(Ka)}{J_{\nu}(Ka)}, \quad (2.161)$$

$$J^- = \frac{1}{Ka} \frac{J_{\nu-1}(Ka)}{J_{\nu}(Ka)}, \quad (2.162)$$

$$H^+ = \frac{1}{j\gamma a} \frac{H_{\nu+1}^{(1)}(j\gamma a)}{H_{\nu}^{(1)}(j\gamma a)}, \quad (2.163)$$

and

$$H^- = \frac{1}{j\gamma a} \frac{H_{\nu-1}^{(1)}(j\gamma a)}{H_{\nu}^{(1)}(j\gamma a)}. \quad (2.164)$$

The identities for general Bessel, Neumann, and Hankel functions needed are

$$Z'_\nu = \frac{1}{2}(Z_{\nu-1} - Z_{\nu+1}) \quad (2.165)$$

and

$$Z_{\nu+1}(x) + Z_{\nu-1}(x) = \frac{2\nu}{x} Z_\nu(x). \quad (2.166)$$

By using the notation shown in Equations (2.161) to (2.166) the characteristic equation can be simplified. This equation is found to be

$$\left(\frac{\varepsilon_1}{\varepsilon_2} J^- - H^-\right)(J^+ - H^+) + \left(\frac{\varepsilon_1}{\varepsilon_2} J^+ - H^+\right)(J^- - H^-) = 0. \quad (2.167)$$

Equation (2.167) is used to evaluate the cutoff conditions for the modes propagating in the fiber. Recalling that at cutoff $\gamma = 0$, so the modified Hankel function is infinite since its argument is zero. Due to this a non zero argument for the Hankel function must be used as γ approaches zero. This is accomplished by taking the limit of the Hankel functions:

$$\lim_{\gamma \rightarrow 0} H_0^{(1)}(j\gamma a) = \frac{2j}{\pi} \ln \frac{\Gamma(ja)}{2} \quad \text{for } \nu = 0 \quad (2.168)$$

and

$$\lim_{\gamma \rightarrow 0} H_\nu^{(1)}(j\gamma a) = \frac{-j(\nu-1)!}{\pi} \left(\frac{2}{ja}\right)^\nu \quad \text{for } \nu = 1, 2, 3, \dots \quad (2.169)$$

where $\Gamma = 1.781672$.

By substituting Equations (2.168) and (2.169) into Equations (2.165) and (2.166) the limits of the modified Hankel functions with the new notation can be found:

$$\lim_{\gamma \rightarrow 0} H^+ = \frac{-2\nu}{(\alpha\gamma)^2} \quad \text{for } \nu = 1, 2, 3, \dots, \quad (2.170)$$

$$\lim_{\gamma \rightarrow 0} H^- = -\ln \frac{\Gamma(\nu)}{2} \quad \text{for } \nu = 1, \quad (2.171)$$

and

$$\lim_{\gamma \rightarrow 0} H^- = \frac{1}{2(\nu - 1)} \quad \text{for } \nu = 2, 3, 4, \dots \quad (2.172)$$

Equations (2.170) to (2.172) are used in Equation (2.167) to find the cutoff conditions for the different modes with $\nu > 0$. These modes are the HE and EH modes. Equations (2.152) and (2.153) are used to find the TE and TM modes with $\nu = 0$.

For the case where $\nu = 1$ the solution to Equation (2.167) as $\gamma \rightarrow 0$ becomes

$$J_1(Ka) = 0 \quad (2.173)$$

which describes the cutoff conditions for the $HE_{1\mu}$ and $EH_{1\mu}$ modes. The HE_{11} mode is included since it is a solution to Equation (2.167) for $\nu = 1$.

The cutoff conditions for the $HE_{\nu\mu}$ and the $EH_{\nu\mu}$ modes are found by making $\nu > 1$ in Equation (2.167) as $\gamma \rightarrow 0$. This equation has two solutions which after simplification become

$$J_\nu(Ka) = 0 \quad \text{for } \nu = 2, 3, 4, \dots \quad (2.174)$$

and

$$\left(\frac{\epsilon_1}{\epsilon_2} + 1\right) J_{\nu-1}(Ka) = \frac{Ka}{\nu - 1} J_\nu(Ka) \quad \text{for } \nu = 2, 3, 4, \dots \quad (2.175)$$

It is shown in Reference [2] that $Ka = 0$ is not a solution of Equation (2.174) since ν is greater than 1 and thus will not be a solution to Equation (2.167).

The cutoff conditions for the TE and TM modes are found using the characteristic Equations (2.152) and (2.153). For small values of γ and $\nu = 0$ Equation (2.153) becomes

$$\frac{K}{\epsilon\gamma} \frac{J_0(Ka)}{J_1(Ka)} = \gamma a \ln \frac{\Gamma\gamma a}{2} \quad (2.176)$$

The right side of Equation (2.176) becomes zero since γ approaches zero faster than the natural log approaches infinity, therefore the solution for the TM modes is

$$J_0(Ka) = 0 \quad (2.177)$$

Equation (2.177) is also the solution for the TE modes since the permittivity ratio is divided out of the solution.

From the derivations it is seen that the cutoff conditions are determined by the zeros of the different Bessel functions (Equations (2.173) to (2.177)). A plot of the Bessel functions with ν equal to 0 and 1 is shown in Figure 2.2 with the cutoff conditions for the first few modes.

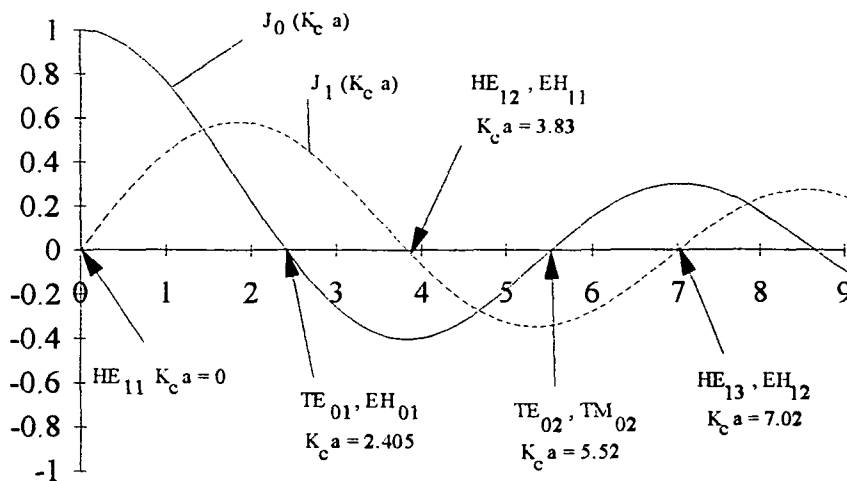


Figure 2.2. The Bessel Functions and the Mode Cutoff Conditions

From Figure 2.2 it is seen that as long as $K_c a \leq 2.405$ only one mode will propagate since there is only one mode with a cutoff value number below 2.405. Applying this and the physical parameters of the waveguide to Equation (2.160) the cutoff frequency can be obtained which defines a singlemode optical fiber.

Equation (2.160) can be rewritten into a form which is based on common physical parameters of glass fibers. Using Equations (2.10) and (2.11), after rearrangement, the equation becomes

$$K_c a = \omega_c (\sqrt{\mu_0 \epsilon_0}) (\sqrt{n_1^2 - n_2^2}) a. \quad (2.178)$$

From Equations (2.24) and (2.73) it is found that at cutoff

$$\omega_c \sqrt{\mu_0 \epsilon_0} = \frac{2\pi}{\lambda_0}. \quad (2.179)$$

Substituting Equation (2.179) into (2.178) it is found that

$$K_c a = \frac{2\pi a}{\lambda_0} \sqrt{n_1^2 - n_2^2}. \quad (2.180)$$

Equation (2.180) defines the cutoff parameters of an optical fiber based on the general physical properties of the fiber. The cutoff parameter $K_c a$ is sometimes called the "V" number of an optical fiber and is mainly used to determine the number of modes which propagate in a fiber of a certain design.

From the previous mathematical development it has been shown that there is one mode which is present at all wavelengths in an optical fiber. This mode, called the HE_{11} mode, propagates regardless of the physical design of the optical fiber. From Figure 2.2 it is seen that as long as the "V" number of a fiber is below the cutoff value of the TE_{01} or TM_{01} modes, only one mode will propagate. When this condition is met the optical fiber is called a singlemode fiber. Numerically the "V" number must be less than 2.405. From Equation (2.180) it is noted that by increasing the source wavelength, λ_0 , for a given fiber the number of modes which propagate will decrease. It is significant to note that using a singlemode fiber with a source wavelength less than the cutoff wavelength for singlemode propagation makes the fiber behave like a multimode fiber since more than one mode can propagate.

2.2 Loss Properties in Optical Fibers

Losses in optical fibers are due to four main sources, namely absorption losses, the losses due to internal discontinuities, losses due to the surroundings and losses due to fiber splicing. Absorption losses arise because the particles that make up the optical fiber

vibrate when the electromagnetic waves encounter them. The absorption losses transfer the light power to heat. Internal discontinuities are imperfections caused by manufacturing the glass fibers, small gaps between the core and cladding, presence of glass impurities, and the presence of OH ions in the glass. The disadvantage of these losses is that they are not consistent throughout the fiber therefore their contributions to the total loss of the fiber are hard to evaluate. Surrounding or environmental losses occur when the optical fiber is subjected to physical deformation. Examples of losses due to the environment are: bending with radii much larger than the radius of the fiber, axial twisting of fiber, cable laying losses which are caused by stretching the fiber as it is laid, and axial tension applied to the fiber. Splice losses where cables are connected are encountered at every point where the optical fiber is joined. Discontinuities occur where the fiber is connected to equipment, connected to fiber couplers, and where a fiber was broken and then spliced.

The total attenuation of an optical fiber can be found by relating the output power exiting the fiber to the input power entering the fiber. The relationship is shown in Equation (2.181) below and uses the logarithm of the power ratio to define a decibel loss value.

$$\alpha = 10 \log_{10}(P_{in}/P_{out}) \text{ in dB.} \quad (2.181)$$

The input and output power values used in Equation (2.181) are found by a method commonly called the "cut-back method." It is used for one way transmission loss measurements. With the cut-back method, a fiber is connected to a light source and a power reading (P_{out}) is taken for a certain length of fiber. Then the fiber is cut to a desired length, reconnected to the detection device, and the second power reading is taken

(P_{in}). Using these values of power and the length of fiber cut, a value for the attenuation per length can be found by dividing Equation (2.181) by the length cut. Attenuation can also be expressed in terms of a percentage of output power to input. The percent value of attenuation is sometimes useful in analyzing results when a percentage of a specific loss to total loss is desired.

As previously mentioned, optical fibers exhibit attenuation due to bending with bend radii much larger than the radius of the fiber. This light loss has been studied by the communications industry but the objective was to reduce the effects of bending, not to study the actual properties of the light as it is transmitted through a bend. Unlike communications, a strain measuring device requires that the fibers exhibit moderate if not severe sensitivity to bending. Also the typical length of fiber the communications industry deals with is on the order of kilometers whereas strain measurements deal with fiber lengths of meters. Bending losses are composed of two separate loss factors, transition losses and pure bend loss.

2.2.1 Transition Losses

Transition losses occur in the fiber at the point where the radius of curvature changes from infinite (straight fiber) to a prescribed radius. The abrupt change causes the light to be transformed from a longitudinal wave mode to a cladding mode. Since the cladding modes are not lost immediately, they are coupled back to the longitudinal wave at the second transition from bent to straight. Due to the different path lengths of the cladding mode and the guided mode, different fiber lengths between transition points for different bend radii, and the index differences in the core and cladding, the cladding modes can be coupled back to the guided mode out of phase. Oscillations are caused in the amount of attenuation when the phase differences form constructive and destructive

interference. The abrupt change in radius leads to an average transition loss as given in Equation (2.182) from Reference [3]

$$A_R(\text{dB}) = -10 \log[1 - k^4 n_1^4 (w_0^6 / 8R^2)] \quad (2.182)$$

where $k = 2\pi/\lambda$,

λ = wavelength of light passing through fiber,

n_1 = core refractive index,

w_0 = mode field radius,

and

R = bend radius.

The value of w_0 is given as

$$w_0 = a[.65 + 434 * \sqrt[3]{\lambda/\lambda_c} + 0149(\lambda/\lambda_c)^6] \quad (2.183)$$

where a = core radius, and

λ_c = cutoff wavelength of the fiber.

The transition loss is usually on the order of .2 dB/km. Since the phase of the coupling modes is related to the length of bend between the transitions it is therefore a function of the bend radius. The mode field radius (w_0) is always larger than the core radius and represents the area where the mode is considered guided. Beyond this radius, the mode is not guided in the fiber so the mode field radius defines a **radiation caustic**.

2.2.2 Pure Bend Losses - The Whispering Gallery Mode

The pure bend loss is caused by the constant bend radius being small enough to allow the longitudinal modes to become cladding modes. These losses only occur in the bent section of the optical fiber. For a given radius R, the average pure bend loss per unit length is given by Equation (2.184) from Reference [3]

$$\alpha_c = A_c R^{-1/2} \exp(-UR) \quad (2.184)$$

with A_c and U approximated by

$$A_c \approx 30(\Delta n)^{1/4} \lambda^{-1/2} (\lambda/\lambda_c)^{3/2} \text{ in } (dB/m^{1/2}) \quad (2.185)$$

and

$$U \approx \frac{.705(\Delta n)^{3/2}}{\lambda[2.748 - .996(\lambda/\lambda_c)]^3} \text{ in } (m^{-1}) \quad (2.186)$$

where $\Delta n = n_1 - n_2$ = index difference in the core and cladding.

By knowing the index difference and the fiber cutoff wavelength, the average pure bend attenuation can be found.

From previous experimental studies it was thought that the pure bend loss was of an exponential behavior and was completely represented by Equation (2.184) with a simple dependence on wavelength and bend radius. Experimental research presented in Chapter 4 of this thesis has shown that the pure bend loss also exhibits oscillations due to coupling of modes to the guided HE_{11} mode. These oscillations are caused by the coupling of the Whispering Gallery mode to the guided mode during the constant bend

section of the optical fiber. Although the Whispering Gallery mode is a cladding mode it is different from the cladding mode producing the oscillations mentioned in the transition losses section of the thesis.

The Whispering Gallery mode is described as a mode of light traveling between the outer surface of the cladding and a radiation caustic within the cladding. A schematic of the mode travel is shown in Figure 2.3 using ray descriptions.

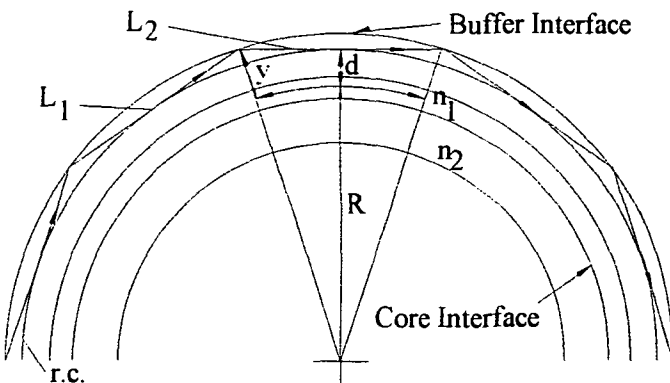


Figure 2.3. Schematic of an Optical Fiber Bent to a Radius R Showing One of the Whispering Gallery Mode Rays Between the Radiation Caustic (r.c) and the Cladding Surface

The position of the radiation caustic is defined as the radial distance from the center of the core in which the evanescent field in the cladding loses guidance and becomes a radiating field. This is the same analogy applied to an optical fiber to describe cutoff conditions when a mode ceases to be guided and becomes a radiating mode. When the ray loses guidance it will travel a path tangential to the caustic and strike the cladding/buffer interface at a point shown in the figure. Due to the difference in index of the cladding and the buffer, transmission and reflection of the ray occur. The transmission through the interface is lost to the surroundings while the reflected portion returns into the cladding and grazes the radiation caustic at a point farther along the bend. This action of transmission, reflection, and grazing occurs for the entire length of the bend until the fiber is straightened or the mode loses its field energy. From these two features it is seen that the pure bend loss is composed of the losses to the surroundings and the losses which develop into the Whispering Gallery mode.

At the radiation caustic, the phase velocities of the evanescent field of the guided mode in the cladding and the Whispering Gallery mode are the same. This also means that the phase velocity of the evanescent field from the Whispering Gallery mode in the core is

the same as the guided mode's velocity. Since the modes have the same phase velocities, coupling in the core is possible each time the Whispering Gallery mode grazes the radiation caustic. The depiction of the ray travel shown in Figure 2.3 is only one ray traveling in the cladding. In actuality many rays are grazing the radiation caustic throughout the length of the bend so there is a continuous coupling of the light between the Whispering Gallery mode and the guided mode.

With reference to Figure 2.3, the distance from the radiation caustic to the center of the fiber core is related to the bend radius of the fiber and the wavelength of the light by

$$d = R \left[\frac{\beta\lambda}{2\pi n_2} - 1 \right] \quad (2.187)$$

From Equation (2.187) it is found that for large bend radii the distance d is large which lowers coupling of the evanescent field to the mode field and reduces the power transfer. With smaller bend radii, the caustic is closer to the core so coupling is stronger. This produces higher energy transfer between the modes and raises the power guided by the fiber.

The energy coupled from the Whispering Gallery mode to the guide mode not only depends on the distance between the core and the caustic, but also on the phase difference between the modes at the point of coupling. Additive or synchronous coupling occurs when the Whispering Gallery mode which grazes the caustic is in phase with the guided mode in the core. Asynchronous coupling occurs when the modes are out of phase by 180 degrees. It was found in Reference [4] that the asynchronous coupling occurs at every other grazing point and since the coupling is constant over the bend length, the net effect

produces little attenuation change. At these points the attenuation values approach the values for the average pure bend loss.

Again referring to Figure 2.3, the phase equation for synchronous coupling is found to be

$$2\pi n_2 \frac{L_1 + L_2}{\lambda} + \phi - Z\beta = 2m\pi \quad (2.188)$$

where m = an integer value defining the different coupling radii and
 ϕ = the phase change due to the reflection at the cladding/buffer interface.

From trigonometric relations, the values for the arc length and the ray travel lengths are found to be

$$L_1 = L_2 = \sqrt{(R+y)^2 - (R+d)^2} \quad (2.189)$$

and

$$Z = 2R \tan^{-1} \left[\frac{L_1}{R+d} \right]. \quad (2.190)$$

By substituting Equations (2.189) and (2.190) into Equation (2.188) the values of bend radius corresponding to the positions of synchronous coupling are obtained. After substitution the equation used to find these positions is found to be

$$2\pi n_2 \left(\frac{2\sqrt{(R+y)^2 - (R+d)^2}}{\lambda} \right) + \phi = 2m\pi$$

$$-2\beta R \tan^{-1} \left(\frac{\sqrt{(R+y)^2 - (R+d)^2}}{R+d} \right) = 2m\pi \quad (2.191)$$

For a given fiber, all of the variables except the bend radius (R) and the integer value of m in Equation (2.191) are known. This shows that for a particular fiber, values of bend radius at synchronous coupling positions can be found by substituting the properties of the fiber and a value for m . Although the variable m has no descriptive name it is a method of describing which coupling position corresponds to a particular radius value.

2.3 Strain Sensing

Due to the optical fibers sensitivity to bending, it provides a means to detect structural bending when attached or embedded into a structure. Although this feature is the basis for optical strain sensing, little information can be found unless the orientation of the fiber on or in the structure is correct.

In order for an optical fiber to detect strain due to bending it must be curved to a degree much larger than any load bearing structure could withstand without failing. The problem is overcome by giving the fiber an initial bend of a prescribed radius and then using the pre-bent fiber in the structure. By using a pre-bent fiber, the sensor can react to structural bends immediately upon loading since the fiber is already at a high attenuating bend radius. This type of fiber orientation is called a serpentine configuration.

If a straight optical fiber was used in a structure for strain sensing the amount of bending seen by the optical fiber would be the same as the structural bending due to loading. However for a serpentine fiber this is not the case. From Reference [5] it was found that the relation for structural bending to fiber bending is given as

$$\rho(\Theta_f) = \frac{R}{\sqrt{[1 + (\frac{R}{R_{st}})^2 \sin^4(\Theta_f)]}} \quad (2.192)$$

where R = the initial pre-bend for the optical fiber,

R_{st} = Structural bend radius due to loading,

and

Θ_f = the angular orientation of the pre-bent fiber.

From Equation (2.192) it is seen that the orientation of the prebend determines the amount of fiber bending due to structural bending. Recalling that the transition points of an optical fiber are where the fiber radius goes from straight to a prescribed radius, the angle Θ_f is defined as the angle between the direction of applied moment causing structural bending to a line which crosses the transition points of the optical fiber (the right-hand rule is helpful here). Figure 2.4 is an example of a pre-bent fiber showing the various parameters used in Equation (2.192).

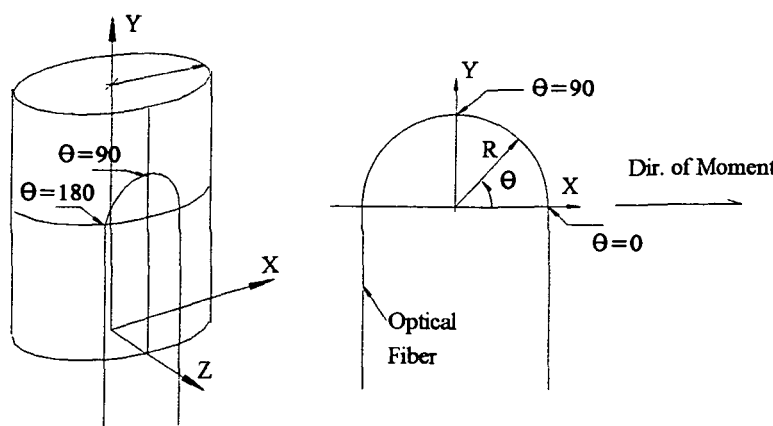


Figure 2.4. A Schematic Showing the Properties Used in Equation (2.192)

The fibers prebend radius is also affected by the stresses caused by loading the structure since it is attached to the structure and experiences the same deflections due to load. The relationship between structural stress and fiber curvature change is found to be

$$\rho(\Theta_f) = R \frac{[(1 + \frac{\sigma_x}{E_{st}} - \nu_{pr} \frac{\sigma_y}{E_{st}})^2 \sin^2(\Theta_f) + (1 + \frac{\sigma_y}{E_{st}} - \nu_{pr} \frac{\sigma_x}{E_{st}})^2 \cos^2(\Theta_f)]^{3/2}}{(1 + \frac{\sigma_x}{E_{st}} - \nu_{pr} \frac{\sigma_y}{E_{st}})(1 + \frac{\sigma_y}{E_{st}} - \nu_{pr} \frac{\sigma_x}{E_{st}})} \quad (2.193)$$

where R = Fiber Bend Radius,

E_{st} = Modulus of Elasticity of the structure,

ν_{pr} = Poission's ratio,

σ_x = Normal stress in the direction parallel to a line through the fiber transition points,

and

σ_y = Normal stress in the direction perpendicular to a line through the fiber transition points.

Using the contributions of Equations (2.192) and (2.193) the changes in fiber curvature due to structural radius changes and structural stress levels can be determined.

If a fiber is embedded into a part there is a possibility that it will be placed on the neutral plane of the structure. The neutral plane is defined as the plane at which there is no strain acting and as an example would be found at the midplane of a structure with a rectangular cross section. If the optical sensor is located on the neutral plane then Equation (2.192) relates the fiber curvature to the structural curvature since there would be no stress or strain applied to the fiber.

From Equations (2.182) to (2.186) it is found that the attenuation of the light is a function of the fiber bend radius. In Equations (2.192) and (2.193) the bend radius of the fiber is a function of structural curvature and structural stress. Since structural stress and bending are both related to strain, it is possible to develop a correlation of structural strain to optical attenuation. In general, the amount of light will vary inversely with the amount of bend, consequently the amount of strain.

CHAPTER 3

Attenuation Measurement Methods

In order to evaluate the optical fibers sensitivity to bending, the proper equipment is needed. There are two methods used to test optical fiber setups whether it is used for communications or sensor applications. These are through transmission and optical reflectometry. Two products fall under the category of optical reflectometry, these are the standard Optical Time Domain Reflectometer (OTDR), and the less common Photon Counting Reflectometer (PCR). These three methods have different advantages and disadvantages so the best method of testing depends on the constraints of the system being evaluated. An overview of the methods is presented.

3.1 Continuous Wave Through Transmission

In the through transmission method, a laser source produces a continuous wave(CW) or a modulated signal which passes into the optical fiber being tested and is detected at the other end by an optical detector. Due to the stability, compact size, and ease of coupling to optical fiber, laser diodes are typically used as the light source. The detection device is either a PIN photodiode or an avalanche photodiode (APD) connected to an amplifier. The PIN type photodiode receives its name from the layer orientation of the p-type and n-type semiconductor material. The APD is named for the process used to excite electron-hole pairs. Internal current gain occurs in the APD when electron carriers gain enough energy, while traveling through a reverse biased junction, to release new electron-hole pairs. This is accomplished by impact ionization. The repeated impacts and releases of electron pairs cause an avalanche effect, thus giving the diode its name. The amplifier for the photodiode is required since it only produces small amounts of current

which must be amplified in order to be displayed or used. This amplification leads to significant noise which may hide weak signals and must be averaged out. For CWTT testing the signal-to-noise ratio is high and averaging is used to allow small real changes in output light power to be detected that would look like noise fluctuations. Typically five to ten averages remove the noise which only requires a few milliseconds. The signal may be displayed on a sampling oscilloscope with a sampling rate that is 3 times greater than the frequency response of the detection device.

For the through transmission method, large amounts of light (relative to the noise produced by the electronics) can be sent through the fiber continuously so slight changes in output power can be easily and accurately detected. The main disadvantage of this system is that the factors which attenuate the light as it passes through the fiber are combined to produce the net change (integrated sum) of the attenuation in power detected by the photodiode. In other words, the CWTT type of detection cannot locate the position of a zone of loss along the length of the fiber or distinguish between the types of attenuation.

3.2 Optical Time Domain Reflectometry

The OTDR is essentially an optical pulse-echo system. A pulse of light (typically 5 to 10 ns width) from a laser diode is sent through the fiber and undergoes Rayleigh scattering continuously along the length of the fiber, producing low-level reflected signals. Rayleigh scattering is caused by factors such as fluctuations in fiber composition, fiber impurities, and environmental loss effects. The reflected signals are split off with an optical coupler and are detected by an APD, and through amplification and processing, the trace of the signal is displayed as a function of pulse flight time through the fiber. The signals are processed, stored, and displayed on a storage sampling oscilloscope. Other types of light reflection such as Fresnel reflections and the losses due to bending are

detectable since they also produce a reflected signal. Fresnel reflections occur at every place where the optical fiber has been spliced, connected, or broken. By knowing the speed of light through the fiber and the flight time of the pulse traveling to a point of attenuation and back to the APD, the distance from the input end of the fiber to the point of high backscatter can be found. Due to the electronic circuitry used to modulate the pulses of light, the amount of energy contained in each pulse is small, consequently the reflected signal is small. Again the signal must be amplified to be used but the noise from the circuitry may overcome the reflected signal entirely. OTDRs typically require large amounts of averaging to produce accurate displays of the attenuation of an optical fiber. Averaging techniques such as the "boxcar averager" are employed to reduce the noise level and obtain a usable signal. With a boxcar averager, a signal is repetitively sampled at a constant time interval relative to the input of the pulse for a specified number of samples and then the time is advanced and a new set of signals is repetitively sampled to produce the next boxcar average point. This is done for the entire signal and then the "boxcars" are placed end to end to display the averaged reflected signal. Higher number of samples at each time interval yield more accurate results by increasing the signal-to-noise ratio, but cause slower display regeneration which is on the order of 5 to 15 seconds.

The resolution of the OTDR is mainly based on the pulse width. The smallest detectable spacing between reflections is one-half of the pulse width. For example, if the pulse width is 300 ps (300×10^{-12} s) and light is traveling through glass with an index of 1.5, the light's velocity is 2×10^8 m/s and the maximum resolution is 3 cm. This is assuming an absolute square wave and no variation (jitter) in duration or repetition rate. Pulse widths of 5 to 10 ns require one Giga-Hertz sampling rate or higher from the circuitry, but allow the equipment to detect both Rayleigh backscatter and Fresnel reflections. Currently only sampling oscilloscopes can digitize at Giga-Hertz rates.

Fresnel reflections return a high amount of light which saturates the APD and essentially blinds the circuitry. This saturation produces a dead zone for a period of time until the APD can stabilize again. In terms of fiber length, the dead zone is on the order of several meters. In the dead zone, attenuation values for the fiber cannot be obtained.

Figure 3.1 is a screen display of a Hewlett-Packard OTDR showing the dead zone of a fiber under test.

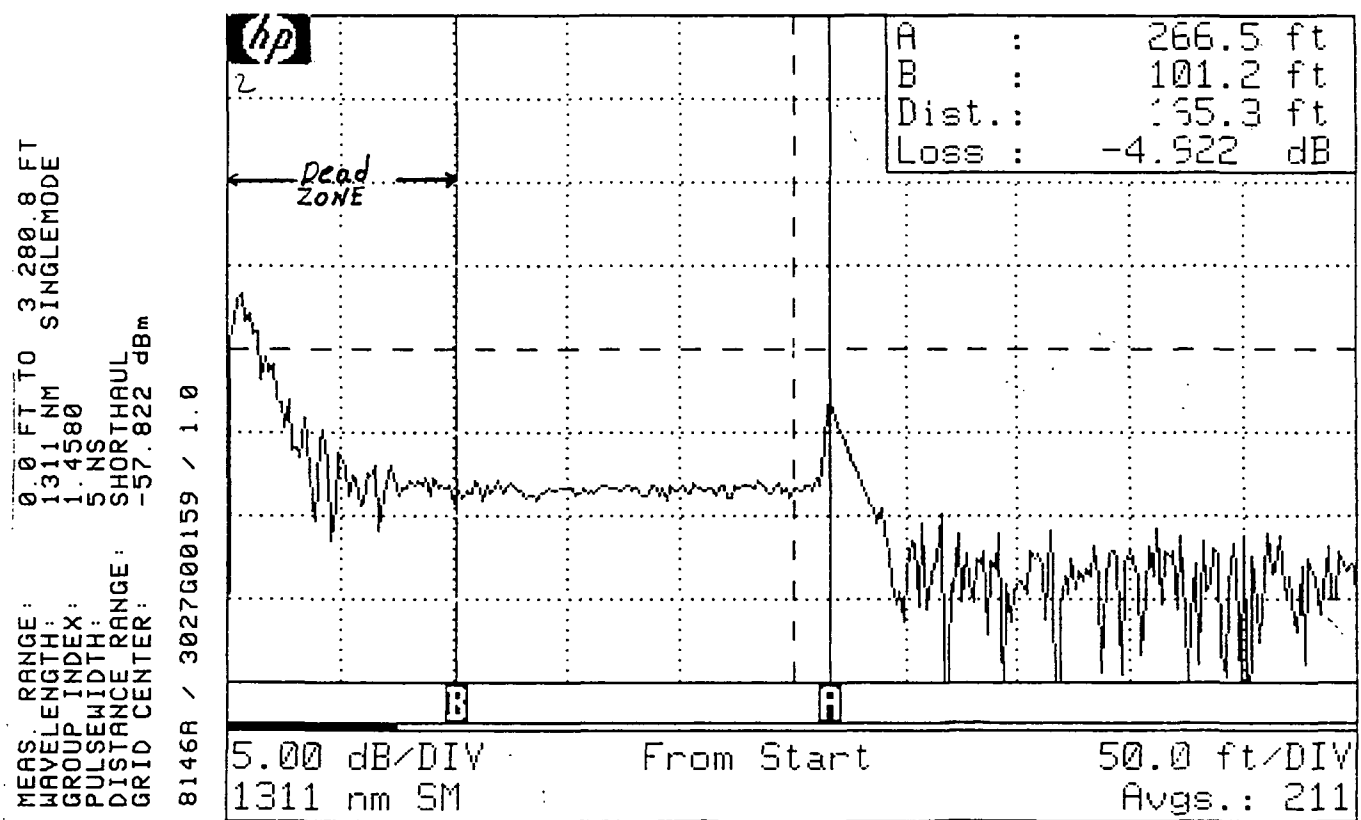


Figure 3.1. Display of an OTDR Showing the Dead Zone of the Fiber

The OTDR can be configured for a variety of fiber types and lengths. As the fiber length setting is increased, more power is transmitted through the fiber in order to detect attenuation losses at the longer length. This is accomplished by using broader pulse widths of the modulated signal. Since the pulse width is wider, the sensitivity of the equipment's position detection is reduced. These are essentially the limiting factors of the OTDR type equipment. Higher power results in lower position detection accuracy and lower power results in lower attenuation level accuracy.

3.3 Photon Counting Reflectometer

A specialized OTDR which uses a method of counting photons reflected back from points of attenuation is called a Photon Counting Reflectometer(PCR). The difference in the PCR and the typical OTDR is that, while the OTDR takes a boxcar length of light and averages the data to obtain a group of light reflection values, the PCR takes a single display resolution point and averages at this time position along the fiber by detecting whether a photon of light is reflected back at this position. This is accomplished by a highly accurate and stable time delay circuit with trigger uncertainties of pico-seconds. The detection device is still an APD but microwave circuitry is used to process the light readings. The counter detects whether or not a photon is present so it is essentially processing a 2-bit word, either on or off. Several of these 2-bit words are combined at each point and the number of "on" values are displayed as the attenuation at the display point. When two or more photons are returned at the same time, the detector still only processes that point as "on." By using this method of detection, the effects of saturation due to Fresnel reflection, when the equipment is in the Fresnel detection mode, is almost zero. This means that the dead zone is reduced to a minimum when in the Fresnel detection mode. For the Rayleigh backscattering mode, the high light intensity at splices is still present but the APD is not saturated as much as the typical OTDR since it is switched

on and off by the time delay circuitry. Thus the spatial resolution or detectable differences in attenuation points is much smaller, on the order of millimeters, for the Photon Counting Reflectometer.

CHAPTER 4

Experimental Evaluation of Whisper Modes - CWTT

The strong theoretical correlation between structural strain and optical attenuation lead to the development of testing procedures to further verify the findings. Experimental relations can, in some ways, allow for more accurate correlations since they can compensate for various discrepancies lost by theoretical approximations. The experimental procedures begin with a study of the attenuation of optical power to fiber bend radius. This is a key step in relating the attenuation to strain since the results will provide information about what the initial serpentine bend radius should be as well as determine the correlation of attenuation to bending.

The first tests involved a light emitting diode (LED) and multimode fiber tested using CW through transmission. The LED was powered by circuitry constructed at Tennessee Technological University and the output power was detected using an Optical to Electrical (O/E) converter. A DATA 6000 two channel sampling oscilloscope was used to display the results.

After it was discovered that the optical fiber would attenuate light as a function of the bend radius, a Seastar temperature stabilized laser source was purchased and used as the light source. The Seastar laser system employed a pre-pigtailed laser diode stabilized by a heat sink and a temperature controller and powered by a laser diode driver. Using this source and an O/E converter, the tests were conducted using a singlemode 850 nm fiber and a 830 nm laser diode. A schematic of the test setup is shown in Figure 4.1. The optical fiber was bent around rods of varying radius to obtain the relation. The results of these tests are tabulated in Table 1 of Appendix A and shown in Figures 4.2 and 4.3.

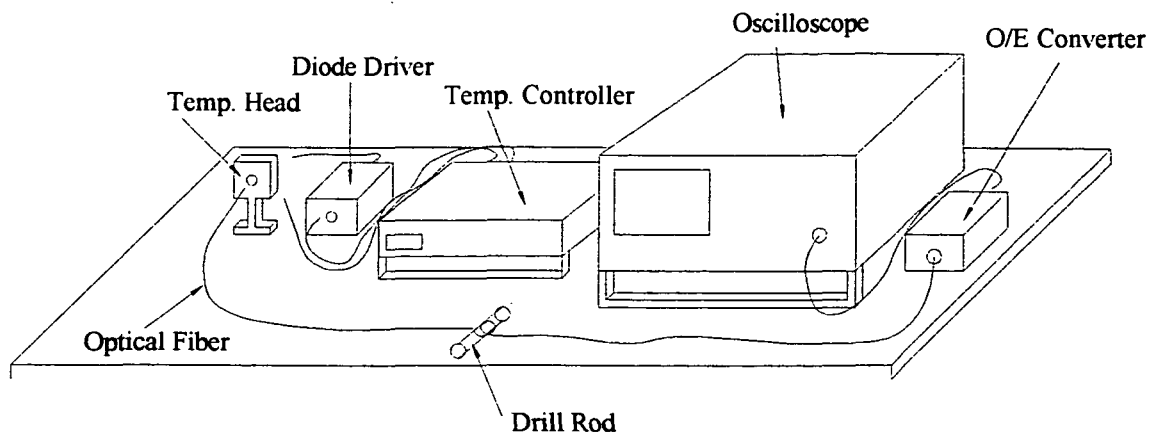


Figure 4.1 Test Setup Used to Test Attenuation vs. Bending
Using CWTT and Drill Rods

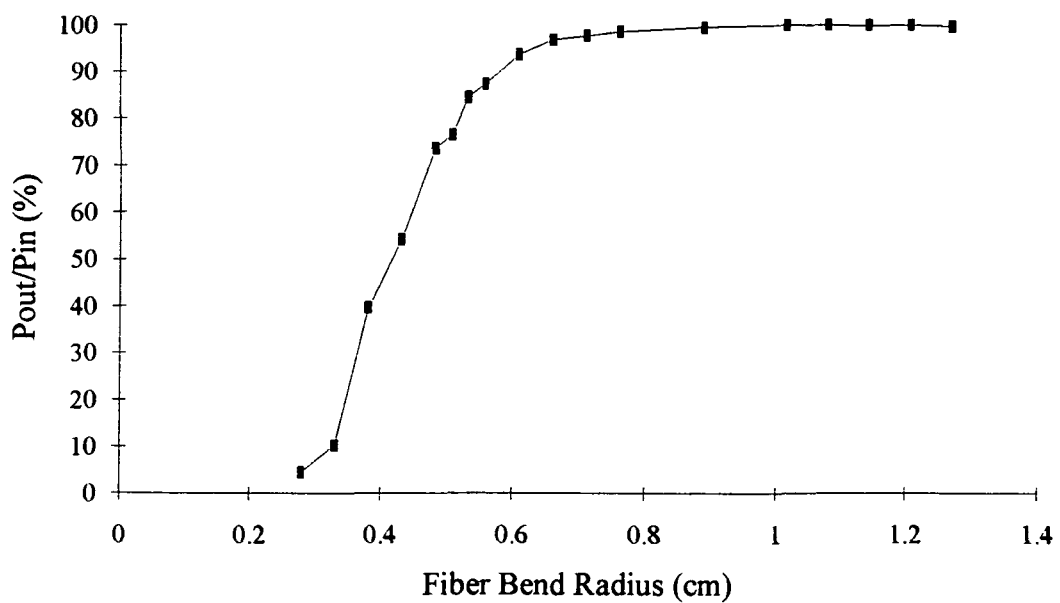


Figure 4.2. $P_{\text{out}} / P_{\text{in}}$ vs. Bend Radius For an 850 nm SM Fiber with an 830 nm Laser
(18 Data Points)

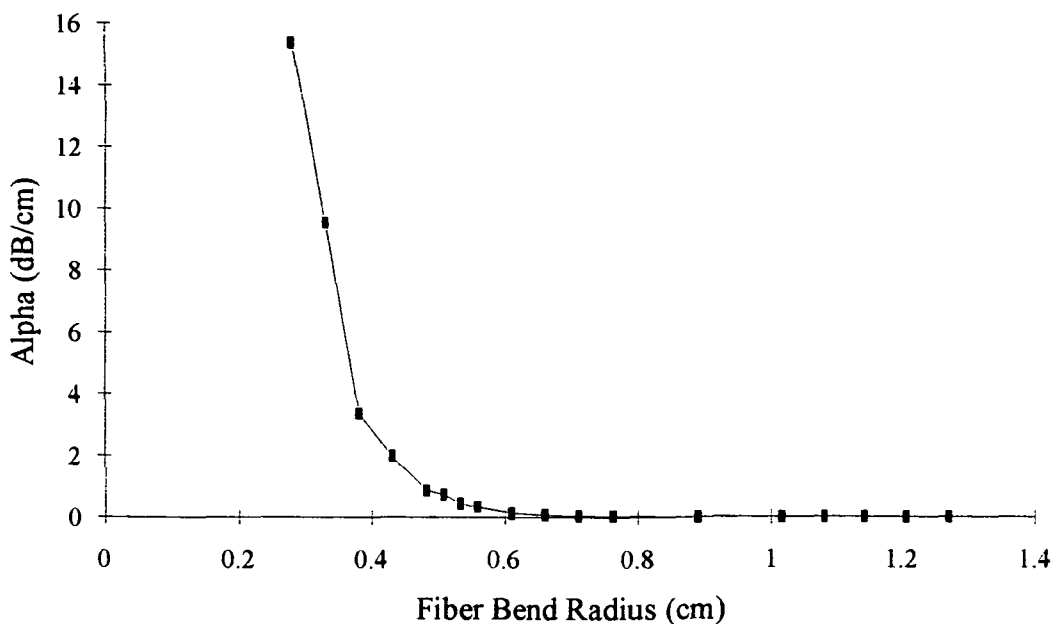


Figure 4.3. α Attenuation per Bend Length vs. Bend Radius For an 850 nm SM Fiber with an 830 nm Laser (18 Data Points)

As can be seen in Figures 4.2 and 4.3, the fiber exhibited attenuation properties as a function of bend radius. It should be noted that eighteen data points were taken over a radius change of approximately one centimeter which gives a radius increment of .0555 cm between points. Due to the large increments only a rough idea of the fiber's attenuation is presented in the figures. This small amount of data caused several important properties of the optical fiber to be hidden that were found later by using more data points and a different test design.

Although the results were promising, Figures 4.2 and 4.3 show that the amount of bend change required to cause a change in attenuation were too large to be used as a strain gage. The material that the gage was testing would most likely plastically deform or break before the fiber could detect a radius change.

It was discovered that instead of mounting a straight fiber on the material to be tested, a pre-bent fiber could be mounted which would increase the bend sensitivity. The fiber was bent to a certain radius and after mounting would be bent, due to stress, on a plane perpendicular to the prebend. This led to the development of a serpentine configuration for mounting the optical fiber [5]. From Figures 4.2 and 4.3 it is seen that the slope of the attenuation vs. radius curve increases with smaller bend radii. This shows that the sensitivity of the sensor can be adjusted to meet structural needs by simply using smaller or larger prebends for the serpentine fiber sensor. Using these correlations, the goal of a transducer can be achieved where light attenuation is related to strain.

4.1 Reduction of the Whisper Modes

In the initial tests of the singlemode fiber using the Seastar equipment the attenuation values were taken with radius increments too large to properly evaluate the fibers sensitivity to bending. To obtain more accurate results, smaller increments between test radii were needed. A test setup was designed using adjustable tapered shanks to vary the radius of the bend as shown in Figure 4.4.

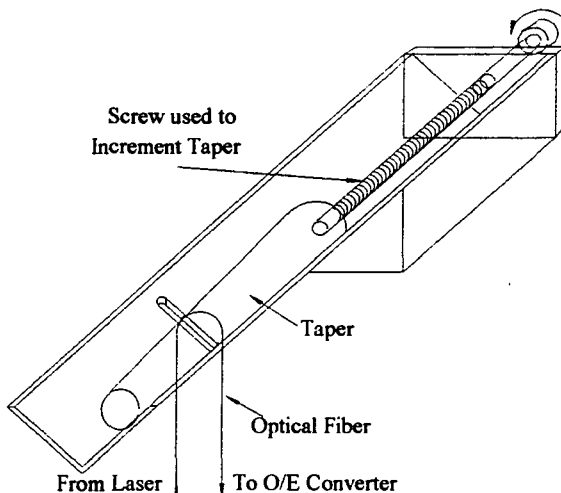


Figure 4.4. Test Setup Using Tapered Shanks to Determine Attenuation
as a Function of Bend Radius

By using tapered shanks and a fixture, the radius could be incremented by small amounts and the relation between radius change and attenuation would be more accurate.

A test was performed using this fixture and an 833 nm SM optical fiber with a 850 nm laser source. The radius increments were approximately .013 cm for the test composed of 23 data points. The results of the test varied dramatically with the first test using the radius increment of .055 cm. To insure that the test was not producing false data, two more tests were performed using increments of .0024 cm and .0016 cm, but the results stayed consistent. The results of testing the 850 nm source and the 833 nm fiber are tabulated in Appendix A.2 and shown in Figure 4.5 which relates attenuation as a percentage to bend radius.

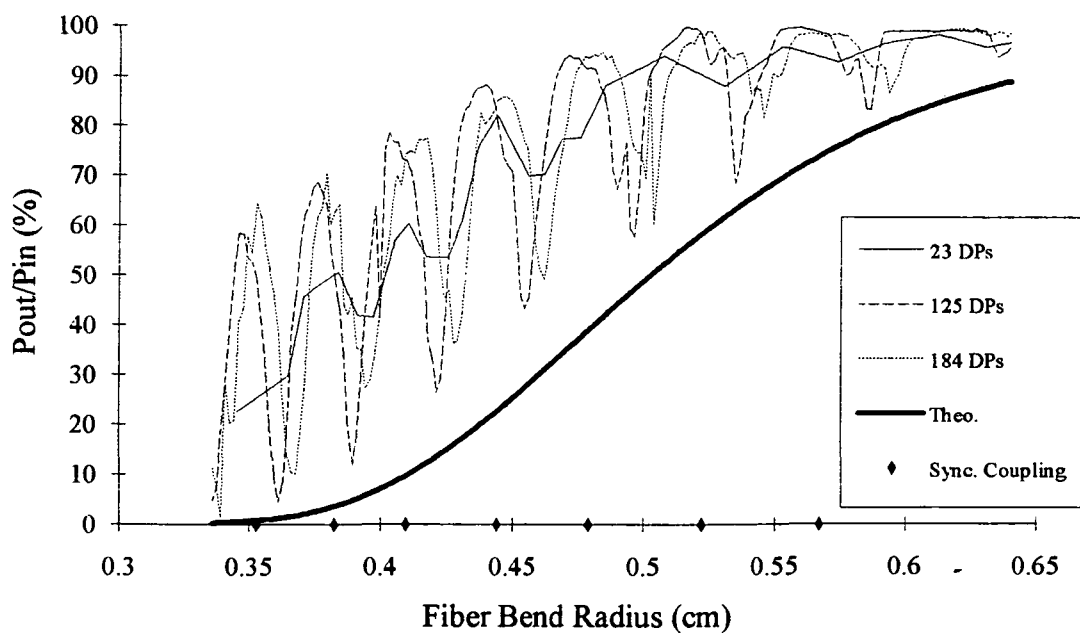


Figure 4.5. P_{out}/P_{in} vs. Bend Radius for an 850 nm SM Fiber with an 833 nm Laser
(23 Data Points, 125 Data Points, and 184 Data Points)

From Figure 4.5 the effects of an optical property called the Whispering Gallery Mode are obvious. It could be theorized that the attenuation oscillations shown in Figure 4.5 are the result of transition losses until it is seen that the percentage of power variation is too large for this type of loss. Figure 4.5 also shows the average pure bend loss theoretically predicted from previous work (Equation 2.184) and the predicted bend radii where synchronous coupling occurs (Equation 2.191). Notice that the experimental curves show a higher output power percentage than the theoretical curve and that the points of asynchronous coupling are closer to the theoretical curve. This helps to validate the findings discussed in the whisper mode section of Chapter 2 of this thesis. To further evaluate the effects of the whisper mode and its correlation to theory, a fourth test was conducted where 270 data points were taken for a radius change from approximately .325 cm to .625 cm. This gives an increment between test points of .001 cm. The results of this test along with the theoretical pure bend loss and points of synchronous coupling are shown in Figure 4.6 as attenuation in dB/cm as a function of fiber bend radius. From this type of comparison it is seen that the theoretical data is lower than the experimental curve and should not be confused with the comparison in Figure 4.5. The power is attenuated less when the percentages are higher and more when the decibels are higher. The points of synchronous coupling are the same as the ones obtained for the previous three tests since the same fiber was tested. The data for the fourth test was taken approximately one year after the first tests and used a different laser diode but by comparing Figures 4.5 and 4.6 it is seen that the whisper mode fluctuations are still stable and the points of synchronous coupling still match. This helps to validate the stability of the correlation. Data for the experimental test of 270 data points using the taper fixture, the theoretical pure bend loss curve, and the positions of synchronous coupling are given in Appendix A.3.

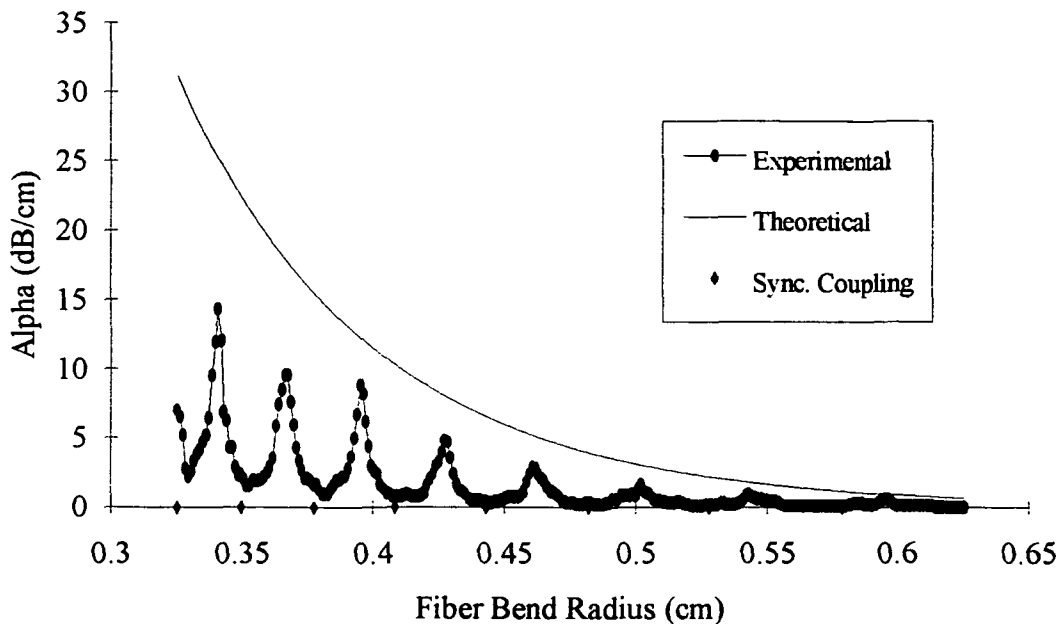


Figure 4.6. Attenuation vs. bend radius for the 270 data points with the theoretical curve and the points of synchronous coupling

The results of the previous test show that the large oscillations produced by the Whispering Gallery mode hamper the development of a strain sensor since the correlation of attenuation to bend radius is not a simple function. Also since several different bend radii have the same value for attenuation due to the whisper oscillations, it would be difficult to determine a reference of the bend radius once the sensor was placed in or on a structure. It was therefore decided to attempt to remove the whispering effects by using variations in the source and the fiber wavelengths. By using a singlemode fiber with a cutoff wavelength lower than the source wavelength, it was thought that the cladding could be filled with modes that had wavelengths too high to be guided. Then these modes would either distribute the cladding modes or disrupt the coupling of the Whispering

Gallery Modes to the guided modes. Two variations in fiber and source wavelengths were tested to determine if the fiber-source mismatch would reduce the effects of the Whispering Gallery mode.

A singlemode optical fiber with a cutoff frequency of 514 nm was tested using a 670 nm laser diode. This setup was tested to see if the large mismatch in fiber and laser would remove the whispering effects of the optical fiber. Four hundred data points were used in this experiment and the results are tabulated in Appendix A.4. Figures 4.7 and 4.8 show the effects of bending the fiber using different radii and the hidden effects found by using a larger number of data points.

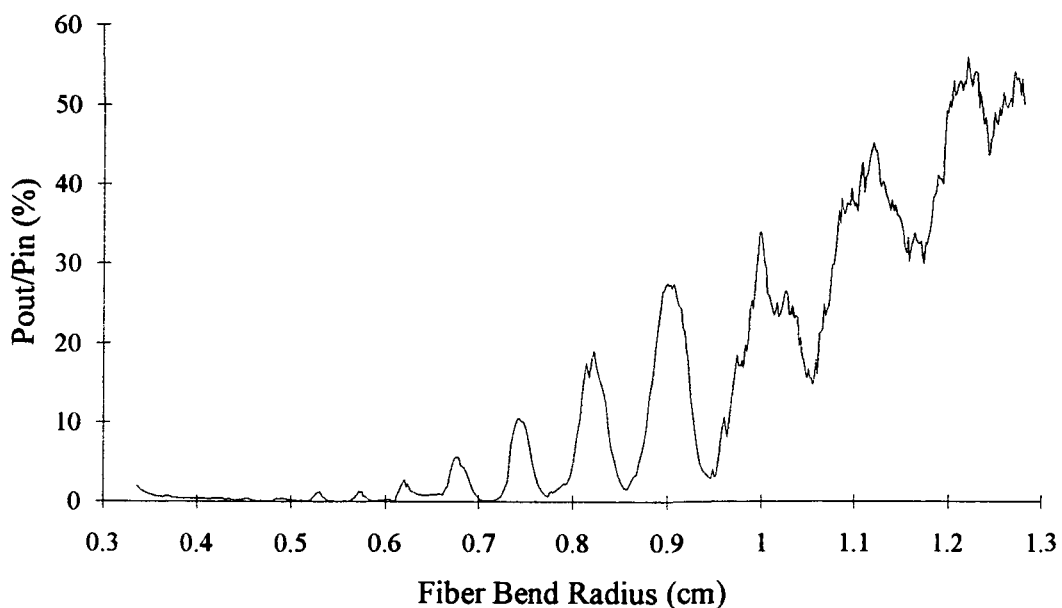


Figure 4.7. $P_{\text{out}} / P_{\text{in}}$ vs. Bend Radius For a 514 nm SM Fiber and a 670 nm Laser Diode

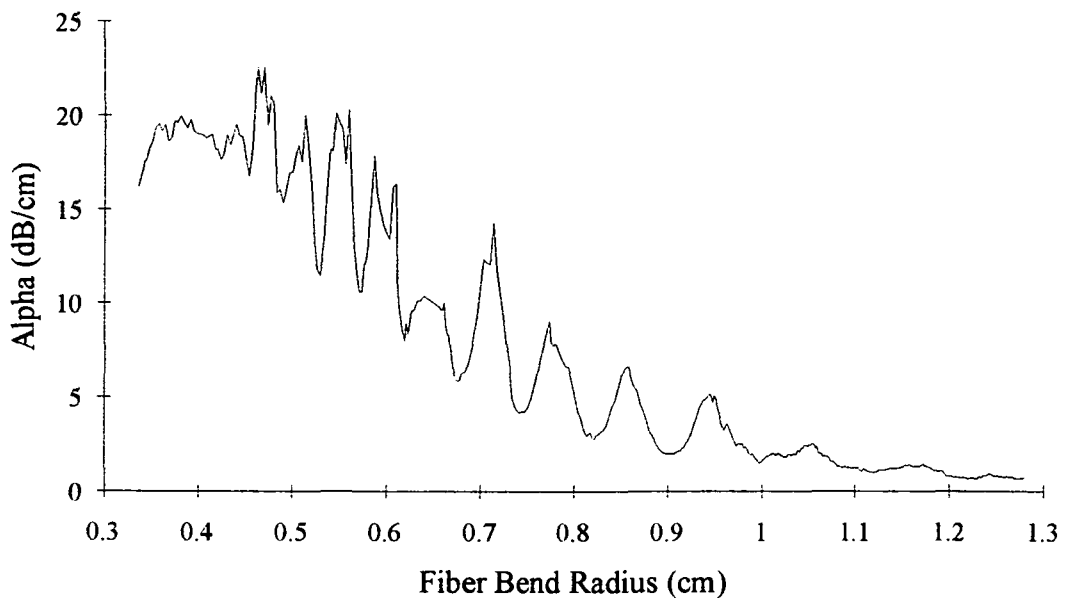


Figure 4.8. α Attenuation per Bend Length vs. Bend Radius For a 514 nm SM Fiber and a 670 nm Laser Diode

As seen in Figures 4.7 and 4.8, this fiber also showed large amounts whisper coupling modes for the case when the fiber was not matched to the laser. With the laser emitting light at a higher wavelength than the cutoff wavelength of the fiber, the light is attenuated severely at any bend radius due to the lack of mode stability in the fiber. It was concluded that this setup would not produce a usable strain gage.

A second test was performed to see if the fiber mismatch would reduce the whispering effects using an infrared laser source and a visible spectrum fiber. The effects of bending a 633 nm singlemode fiber using a 830 nm laser diode are shown in Figures 4.9 and 4.10. The data is given in Appendix A.5.

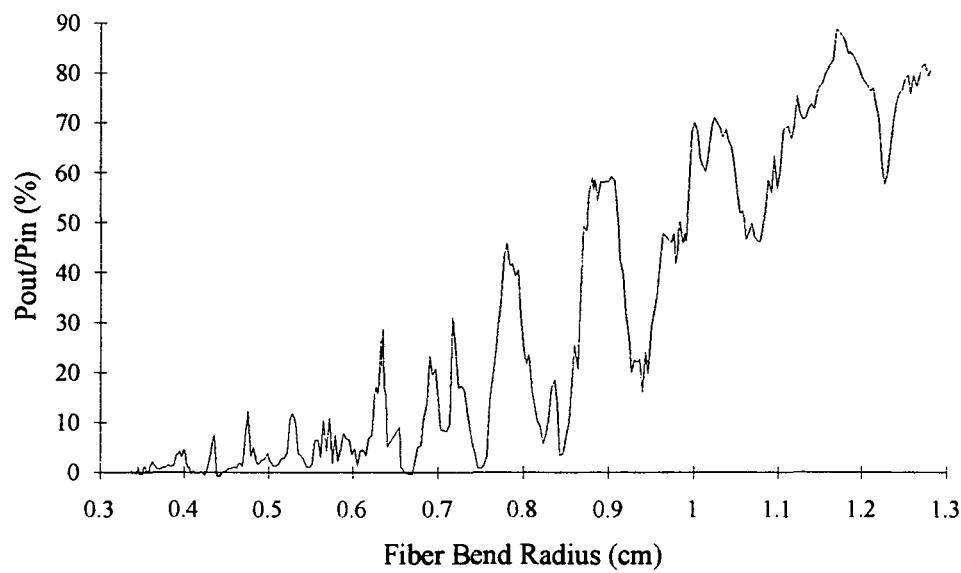


Figure 4.9. P_{out} / P_{in} vs. Bend Radius For a 633 nm SM Fiber Using a 830 nm Laser Diode

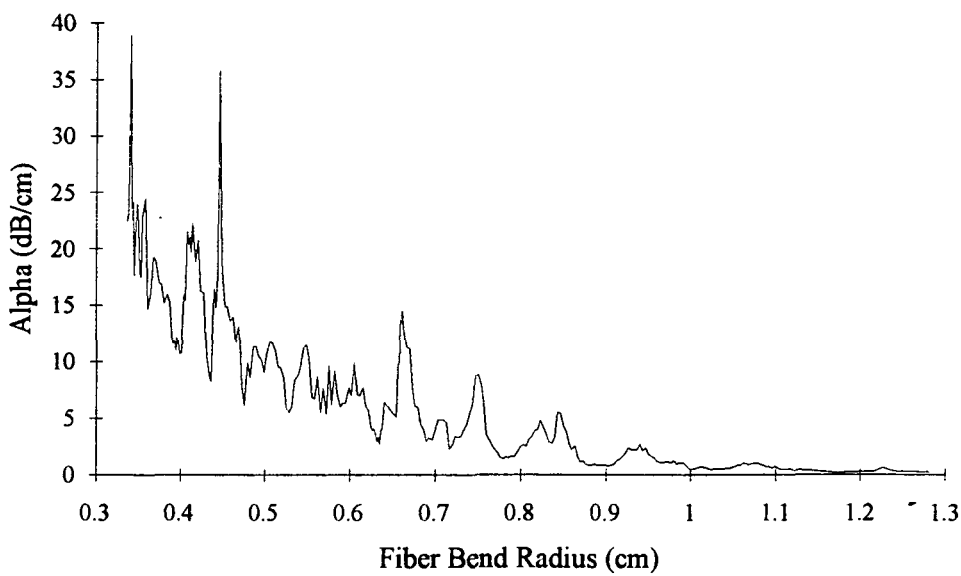


Figure 4.10. α Attenuation per Bend Length vs. Bend Radius For 633 nm SM Fiber Using a 830 nm Laser Diode

Since this setup uses a laser diode which emits light at a higher wavelength than the cutoff wavelength of the fiber, the setup shows similar results to the 514 nm fiber with the 633 nm laser diode (Figures 4.7 and 4.8). Again this did not produce acceptable results.

In comparing Figures 4.7 and 4.9 or 4.8 and 4.10 it is seen that the fiber seems to have an unstable jitter (especially notable in Figure 4.7 at a bend radius of .95 cm and above). This jitter is consistent and due to the fibers inability to sustain wavelengths higher than the cutoff wavelength. The smaller bend radii tend to strip the higher modes which is the reason the signal is cleaner at lower radii. Other than the spikes of attenuation in Figure 4.10 for the 633 nm fiber, the two tests have attenuation values of approximately equal magnitude. This relationship could be due to the difference in fiber and laser wavelengths for each test being approximately equal.

It was decided to evaluate a multimode fiber's sensitivity to bending since the manipulation of the singlemode fibers were not removing the whisper mode. Multimode fibers are capable of supporting hundreds of different modes and it was thought that if the gallery modes were present, their effects would be eliminated due to the different propagation constants and phase differences of the multiple modes.

Using continuous wave through transmission, a 850/1300 nm Multimode fiber was tested using an 830 nm laser diode source. The test was conducted using 100 data points. As shown in Figures 4.11, 4.12 and Appendix A.6, the whispering mode was not encountered.

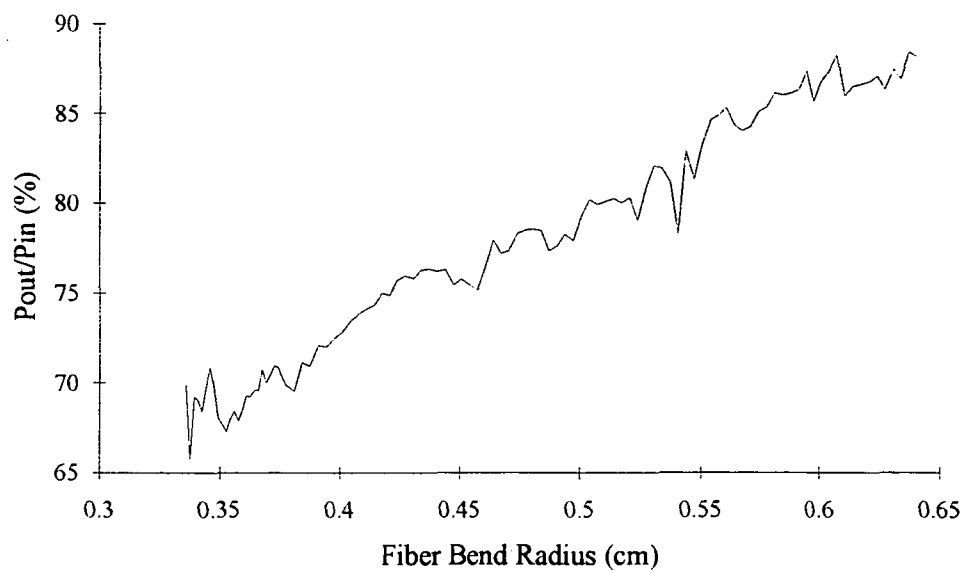


Figure 4.11. $P_{\text{out}} / P_{\text{in}}$ vs. Bend Radius For a 850/1300 nm MM Fiber Using a 830 nm Laser

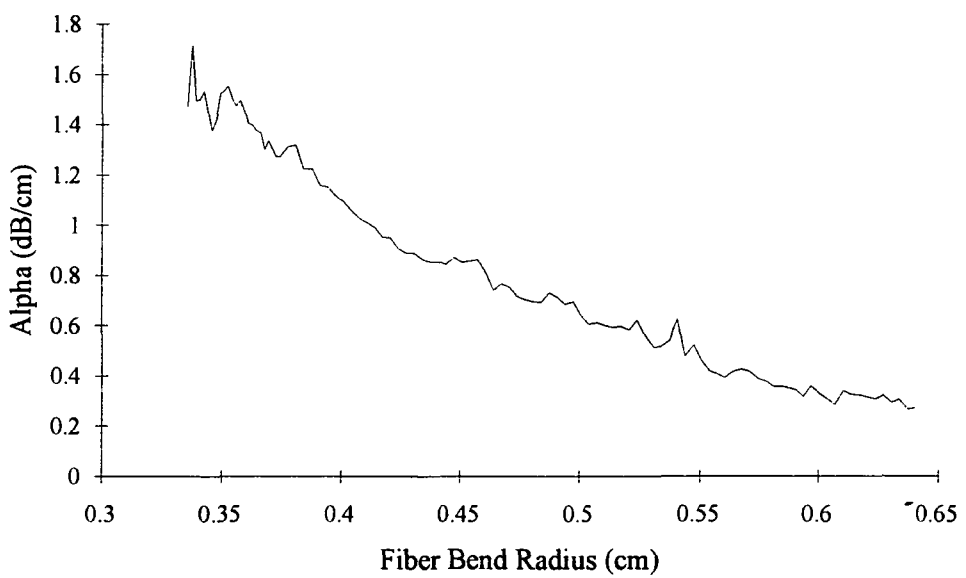


Figure 4.12. α Attenuation per Bend Length vs. Bend Radius For a 850/1300 nm MM Fiber Using a 830 nm Laser

Although the whispering effects were not encountered in the multimode fiber, the fiber does have pronounced jitter in the results. These light jitters are fluctuations in the output power over the time taken to obtain each point of data. It was noticed that if the individual points of data were taken at increments of three to five minutes, the light was able to stabilize and the attenuation jitter was reduced. For a fiber imbedded or mounted to the surface of a structure, the initial serpentine bend would show stable attenuation values but the bend changes due to strain would be inaccurate since they would change as the time increment in sampling was changed. Due to this instability it was determined that multimode fiber would not produce a usable strain sensor. It should be noted that the light could not be fully attenuated in the multimode fiber. Apparently the large core allowed some light to pass through the fiber as long as the fiber was not broken.

4.2 Characterization of Whispering Gallery Modes

After it was found that the whisper modes could not be significantly reduced using the variations in the singlemode optical fibers and that the multimode fiber lacked a consistent attenuation to strain correlation it was decided to characterize the whisper modes. By characterizing the effects of the whisper modes in the singlemode fiber it was thought that the usable strain sensor could be produced which included the attenuation oscillations.

In preliminary tests of the singlemode fiber it was noticed that the level of attenuation varied slightly with surrounding test temperatures at constant bend radii. A test setup was designed to allow for heating of the optical fiber while it was subjected to a known bend radius. A schematic of the heat testing setup is shown in Figure 4.13.

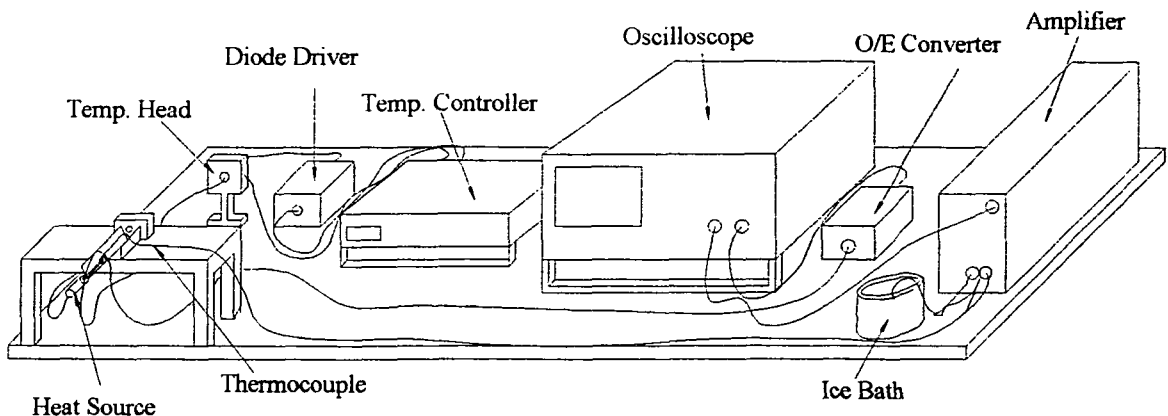


Figure 4.13. Schematic of the setup used to test the optical fibers sensitivity to heating

From this test, values of attenuation as a function of temperature could be found for specific bend radii. The initial test setup used the original tapers from the tests of attenuation as a function of bending radius. These tapers were manufactured from 2024-T6 aluminum. The fiber tested was an 850 nm singlemode fiber attached to an 833 nm laser source. It was thought that if the taper was heated, the radius would change due to the thermal expansion of the taper material. This would mean that if a test was conducted, the levels of attenuation might vary as a function of the fiber bend radius changing due to the taper expanding. Another taper was constructed from a steel rod and a second test was performed to determine if the thermal expansion was causing any variations in the attenuation levels. Tests were performed on the steel taper at the same radius used on the aluminum taper. Since the thermal expansion is different for the two materials, it could be determined if the radius change due to the expansion was causing the attenuation or if the temperature change was. In Figures 4.14 and 4.15, the results of the two tests are overlaid for comparison. The data for the tests is given in Appendix A.7.

c-2.

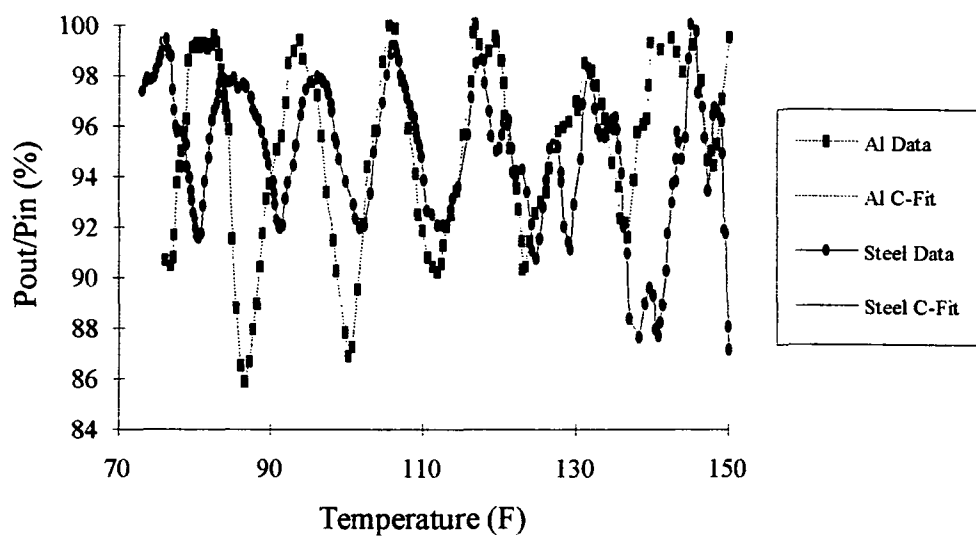


Figure 4.14. Heat tests of the Aluminum and the Steel Taper Showing Attenuation vs.
Actual Temperature Change

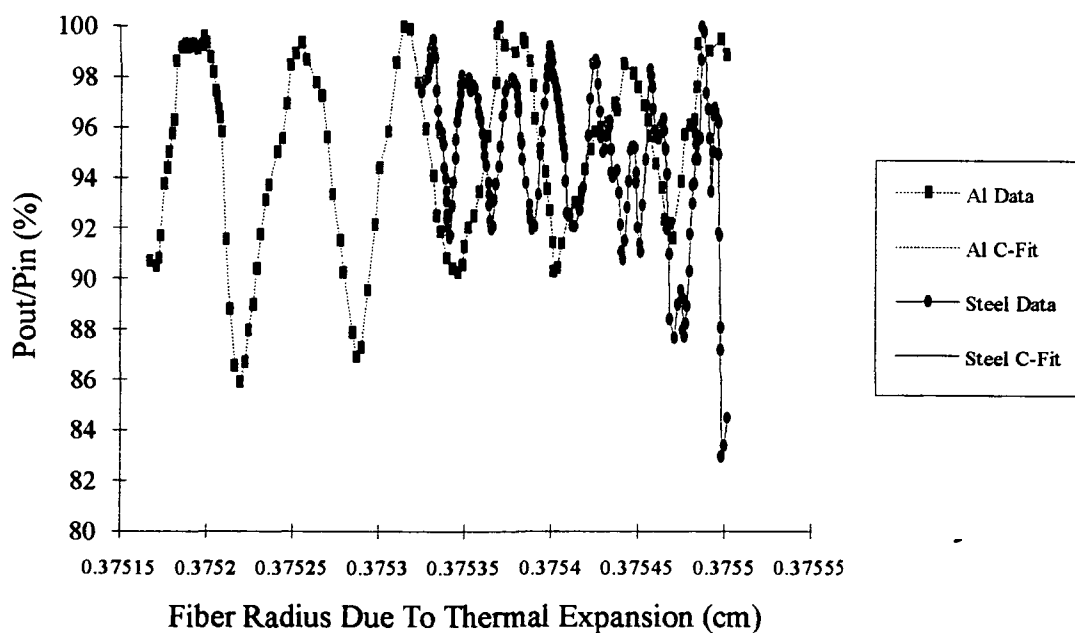


Figure 4.15. Heat tests of the aluminum and steel taper showing the attenuation vs. radius
change caused by thermal expansion of the taper

If the thermal expansion was causing the attenuation changes, the curves in Figure 4.15 would be similar since this figure shows attenuation as a function of radius change due to thermal expansion. If the attenuation was caused by actual temperature changes of the fiber, Figure 4.14 would show similarities because this figure depicts attenuation as a function of fiber temperature.

From Figures 4.14 and 4.15 one can see that the curves are very similar if the attenuation due to temperature changes are compared. However, the attenuation comparisons assuming that the thermal coefficient of expansion is causing radius change have few similarities. It is concluded that the largest factor causing attenuation due to heating the fiber is the actual temperature changes, not the radius changes from thermal expansion. The exact percentage of contribution of each factor is not known but the temperature effects greatly outweigh the expansion effects.

Based on the knowledge that the fiber exhibited attenuation as a function of temperature change a test was performed to see if different bend radii produced different correlations between attenuation and temperature. These correlations could then be used as a temperature "footprint" for a specific radius.

With reference to Figure 4.6, certain bend radii were selected at specific locations on the curve where there were maximum or minimum levels of attenuation. These test points are shown below in Figure 4.16 which is the same data in Figure 4.6 except that the y-axis is now attenuation as a percentage of output power.

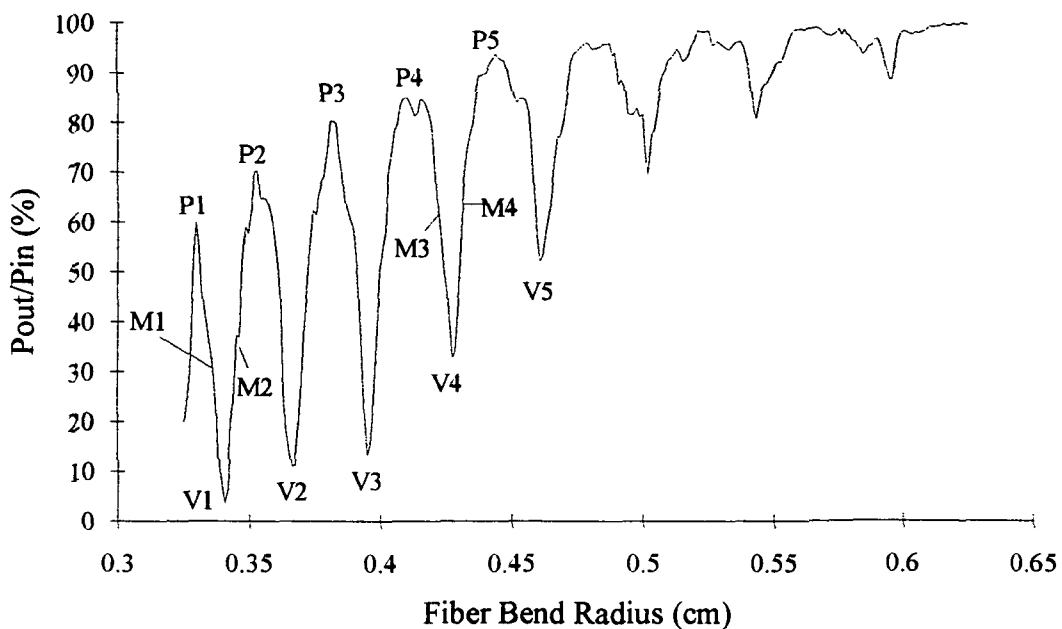


Figure 4.16. Attenuation vs. Bend radius for the singlemode 850 nm fiber showing the test points used in the heat test

The test to find the radius footprints was made using a taper manufactured from monolithic graphite. This material was used in order to minimize any effects of thermal expansion since, although found to be small, the exact contribution is not known. The monolithic graphite also produces an extremely smooth surface when machined which increases the accuracy of locating the specific test radii. Figure 4.16 indicates that five values for the radius were chosen at points of synchronous coupling of the whisper mode, two values were chosen to the left of synchronous coupling points, two were chosen to the right, and five were at points of asynchronous coupling.

The optical fiber was heated from room temperature to approximately 110 degrees F. The glass of the optical fiber could withstand temperatures much higher than the

maximum test temperature but this cutoff temperature was chosen to avoid any deformation of the plastic buffer surrounding the glass fiber.

The results of the temperature testing at the specified points shown in Figure 4.16 for the 850 nm singlemode fiber are shown in Figures B.1 to B.14 of Appendix B. The data for these tests is tabulated in Appendix C.1 to C.14.

From the figures of attenuation vs. temperature in Appnendix B, it is seen that the fiber also exhibits an oscillation as the temperature is varied. These oscillations are small compared to the ones due to the whisper gallery mode. Due to the complex nature of the relation it is unclear what effect the different temperatures have at the particular bend radii by viewing these figures alone. The only usable values found from these figures is the mean value of attenuation for the oscillations. This value can be used to determine what level of attenuation the fiber is seeing and therefore defines a line on the attenuation vs. bend radius curve which crosses the whispering gallery mode oscillations.

In order to obtain more data from the tests, a Fourier transform is employed which converts the attenuation as a function of temperature into attenuation as a function of temperature rate. This is similar to converting data in the time domain to the frequency domain. Using this conversion, the rate of the attenuation oscillations can be found in the temperature domain. Since the data was not approaching zero at the maximum and minimum values of temperature, a Hamming window was used to avoid incorrect data conversion. Also since the data taken was not in exact incremental values of temperature, a linear interpolation curve fit was used and the Fourier transform was taken from the numerical fit. The requirement that the number of data points be multiples of 2^n , with n being an integer value, was avoided by taking a Complex Fast Fourier Transform(CFFT). The CFFT allows data vectors of any size to be transformed from the time domain to the

frequency domain since it returns a two-dimensional Fourier transform. The results of the Fourier transforms for the positions tested are shown in Appendix D.

By finding the values of the large frequency peaks from Figures D.1 through D.14, the initial fiber bend radii can be characterized for the tests. In Table 4.1, the values for the prominent peaks from the tests are presented along with the mean attenuation value. These will be used to describe the "footprint" of the radius so the fiber bend can be found.

Table 4.1. The Mean and Frequency Values from Temperature
Characterization of Optical Fiber

Position Type	Radius (cm)	Mean (%)	1st Freq. (1/Deg F)	2nd Freq. (1/Deg F)	3rd Freq. (1/Deg F)	4th Freq. (1/Deg F)
Peak 1	.329569	.40846	.0763	.178	.2289	.3307
Peak 2	.352924	.54546	.07734	.1547	.232	.3094
Peak 3	.381840	.73849	.07744	.2323	.3098	.3872
Peak 4	.409644	.76799	.07385	.1477	.2708	.32
Peak 5	.444121	.89458	.07704	.1541	.2825	.3595
Middle 1	.334017	.27914	.06454	.1613	.2259	.3872
Middle 2	.347363	.52248	.03154	.09462	.1577	.2839
Middle 3	.419654	.48689	.06061	.1818	.2424	.5455
Middle 4	.435019	.59581	.03202	.1281	.2241	.3522
Valley 1	.340690	.07279	.07265	.1453	.2422	.3875
Valley 2	.366270	.11214	.08352	.167	.2506	.3341
Valley 3	.395186	.20867	.08453	.1691	.2536	.4226
Valley 4	.427439	.34498	.08472	.1412	.2259	.3671
Valley 5	.460804	.49691	.08686	.1448	.2606	.3764

An example of determining the fiber bend radius from a temperature test is illustrated as follows. In Figure 4.17, the whisper fluctuations for attenuation vs. bending are shown. This is the same data used to plot Figure 4.16. Assume that Figure 4.17 is the attenuation correlation for the type of fiber under test. Also assume a table similar to Table 4.1 was previously obtained for the fiber.

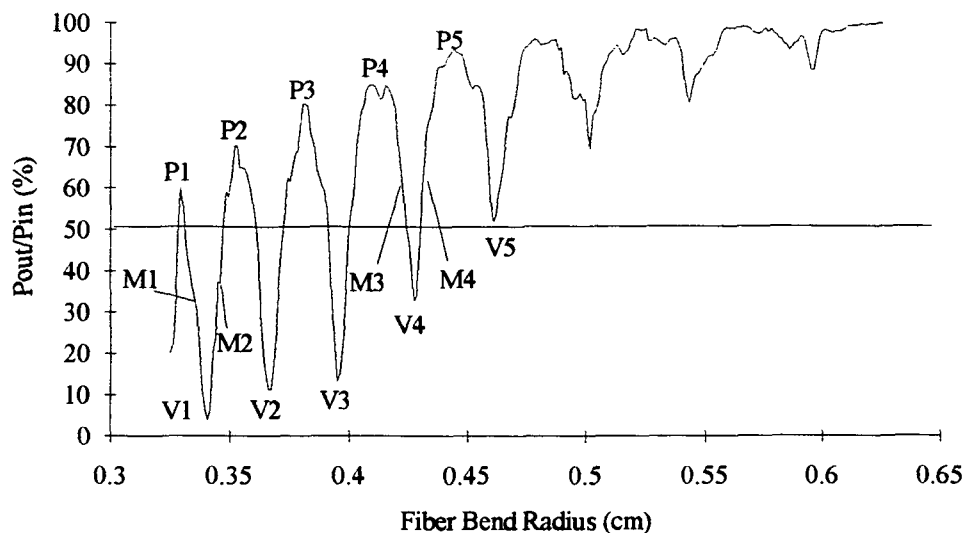


Figure 4.17. Example Figure Used in Determining the Fiber Bend Radius from Temperature Testing

With the background of the fiber known, a heat test is performed on the structure with the same fiber embedded and a mean value of the attenuation along with the major frequencies are found. For the example a mean value of fifty percent is used with first, second, and third frequency values of .080, .140, and .260, respectively. With the mean value known a line representing this value is drawn on the attenuation vs. bend radius plot for the fiber. This is depicted in Figure 4.17 at a value of fifty percent. As seen, the line crosses the data curve at ten locations; four towards the top of a peak, three around the middle of a peak, two towards the bottom of a peak, and one point located at a valley. With the positions of crossing known, a comparison of the frequency values can now be made. In Table 4.1 there are three positions which have a mean value close to the example value of fifty percent. In an actual test there would be eight, one for each crossing. By comparing the first, second, and third frequency values for each of the "known" positions to the example position it is easily seen that the example position is Valley 5 with a radius of .4608 cm.

For the actual characterization of an optical fiber, many positions of attenuation as a function of temperature would have to be found to fully describe the fiber. After the footprints of a particular fiber were found, these would be used for the entire fiber regardless of how many sensors were made from it. This is because each fibers footprint is based on the physical properties of the fiber and they would remain constant for the entire length of fiber pulled from a single glass ingot.

CHAPTER 5

Experimental Evaluation of Whisper Modes-Reflectometry

The majority of testing of the optical fibers sensitivity to bending and the effects of the Whispering Gallery mode have been done using Continuous Wave Through Transmission. This is because larger amounts of energy can be used and the levels of attenuation can be easily detected. With the higher energy levels the experimental error is significantly lower than the error involved in using the reflectometry methods. However, due to the need of equipment capable of detecting multiple positions of bend attenuation, the OTDR and similar equipment have an important role in the development of a strain sensor.

In the process of defining and characterizing the effects of the whisper mode using reflectometry, one is also determining how well this method of testing can detect the parameters needed to fully describe the strain sensor. The CWTT method of testing would be the preferred method of strain sensing if there was only one test point and both ends of the optical fiber were accessible, but this would not be the case in an actual application of the optical fiber sensor. For structural applications, multiple bends would be made down the length of one optical fiber serving as individual strain sensors and the only way to determine individual levels of attenuation would be to use the OTDR method. For this reason the effects of the Whisper mode on the fibers attenuation must also be found using an OTDR.

A comparison of attenuation vs. radius change for the singlemode optical fiber was made using two brands of OTDRs. A Hewlett-Packard OTDR Model 8146A and an Ando OTDR Model AQ-7130 were both equipped with 1300/1550 nm singlemode plug-in

modules. A 1300/1550 singlemode communications optical fiber was tested using the Rayleigh backscatter method of OTDR detection. Although the cutoff wavelength of this fiber was different from the fiber used to develop the whisper mode effects with CWTT, theory predicts that this fiber will also exhibit fluctuations due to the whisper mode. Figure 5.1 and Appendix E.1 show the results of testing the 1300/1550 nm singlemode optical fiber using the two OTDRs.

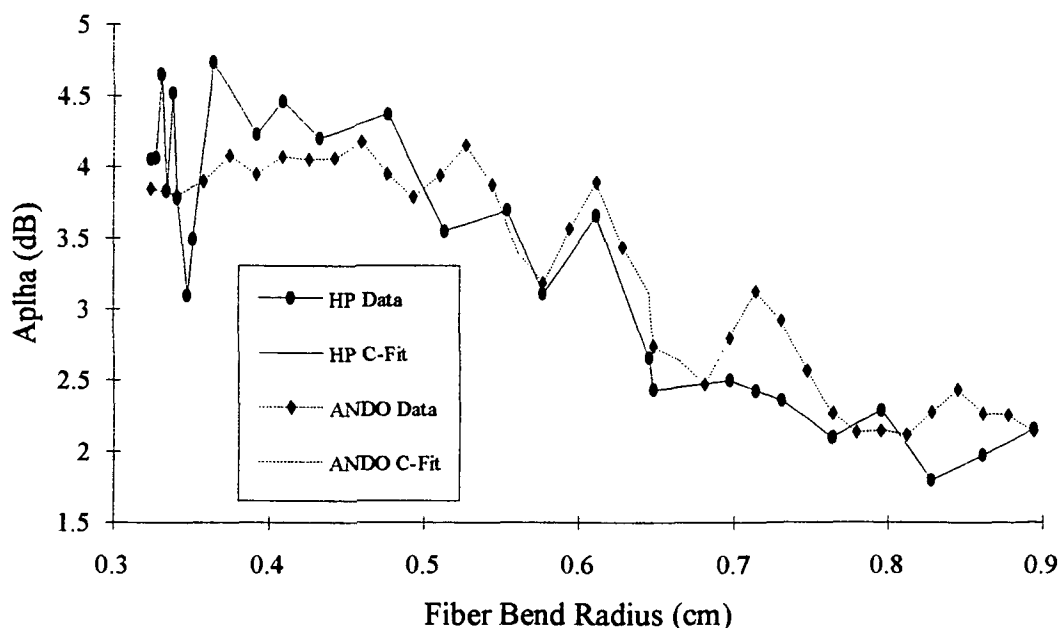


Figure 5.1 α Attenuation vs. Bend Radius for 1300/1550 nm SM Fiber Using the Hewlett Packard and the Ando OTDRs

As seen in Figure 5.1 the tests of the OTDRs compared favorably. The oscillations in attenuation due to the effects of the Whispering Gallery mode are present in both tests but the accuracy and smoothness of the tests using the CWTT have been lost. This is mainly due to the reduction in optical energy that can be used in the OTDR method, the low signal-to-noise ratio, and the smaller number of data points taken. Note that 2 dB/km of attenuation was added to the results of the Ando OTDR for comparison. It was assumed that differences in splicing of the fibers and calibration of the OTDRs led to the increase in attenuation for the Hewlett-Packard OTDR so a linear correction factor could be added without any loss of accuracy.

Another type of OTDR was tested to determine its abilities in sensing the attenuation losses due to bending. This was the Opto-Electronics Photon Counting Reflectometer. The equipment was described as having a better ability in detecting attenuation than the typical OTDRs. This is due to microwave technology and an advanced detection method. The specific piece of equipment used was unable to test singlemode fibers since it was configured to test 850 nm multimode fibers only. For this reason, a test was conducted on an 850 nm multimode optical fiber to determine the performance characteristics. The equipment was also not able to detect Rayleigh backscatter since the data sampler was not taking data at a very high rate (Fresnel detection mode only) so the attenuation of the free end reflection would be used to find the attenuation levels due to bending.

Figure 5.2 and Appendix E.2 show the results of testing the 850 nm MM fiber using the PCR.

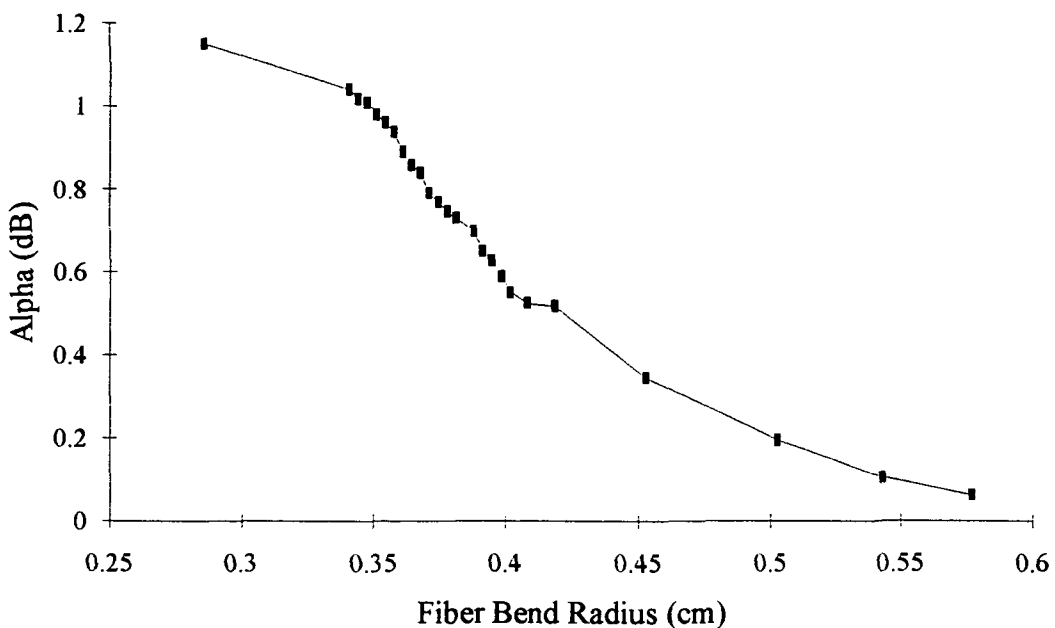


Figure 5.2 α Attenuation vs. Bend Radius for the 850 nm MM Fiber Using the PCR

In comparing Figures 4.12 and 5.2 it is seen that the Photon Counting Reflectometer produced a smoother curve than the tests using the CWTT on the multimode fiber. This is partially due to the smaller number of data points tested and the lower signal-to-noise ratio of the PCR.

The tests of attenuation as a function of bending using the reflectometry methods show that the lower power levels transmitted through the fiber and the lack of accurate attenuation position detection reduce the effectiveness of this type of equipment. It is virtually impossible for the OTDR type equipment to obtain the accuracy found by using CWTT. This is a problem which must be overcome before a multiple bend strain sensor can be properly implemented.

CHAPTER 6

Applications of the Optical Fiber Strain Sensor to Test Parts

The characterization of the singlemode optical fiber leads to the assumption that, with more extensive testing of the fibers sensitivity to temperature, a usable strain sensor can be obtained which will yield satisfactory attenuation as a function of strain. From this, test structures capable of utilizing the strain sensor are needed. Through research between Tennessee Technological University and NASA-MSFC, test structures were designed and fabricated which could incorporate the optical fiber strain sensor. The strain sensor was applied to three configurations of test structure, namely a filament wound tube, a filament wound flat panel, and a polycarbonate (Lexan) flat panel. The design of the parts and the application of the strain sensor are described in the following sections.

6.1 Application of the Strain Sensor to a Filament Wound Graphite Tube

A graphite fiber tube was fabricated on a filament winding machine at NASA-MSFC. The tube was wrapped on a 75 mm diameter mandrel and had a length of approximately 300 mm. The optical sensor was embedded into the tube since this would be a typical configuration for sensor applications. A problem is encountered at the places where the optical fiber exits the structure since the ends of the tube must be machined in order to remove the part from the mandrel. This means that the optical fiber can not exit the tube from the ends because the optical fiber would be cut when the tube is machined. The only other option is for the optical fiber to exit through the surface of the graphite tube by crossing the graphite layers which cover the sensor. This too presents a problem because the places where the optical fiber cross the graphite layers would cause fiber

bends much smaller than the sensors serpentine bend so the light would be highly attenuated at the crossings and the sensor would not detect attenuation due to strain. The problem was solved by developing a fiber optic exit terminator which allowed the optical fiber to pass through the graphite layers without experiencing bend losses due to the layer induced bends. A discussion of the development of the terminator is presented in Appendix F for reference.

A schematic view of the Graphite filament wound tube is shown in Figure 6.1.

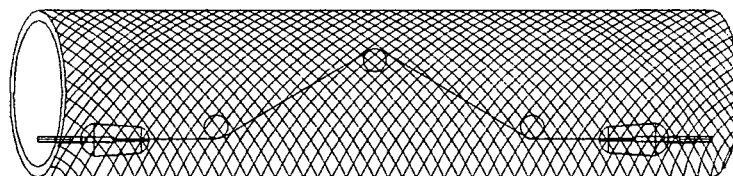


Figure 6.1. Schematic View of The Graphite Mandrel Wrapped Tube

As seen, the strain sensor is composed of a length of fiber bent at three locations and exiting the tube by use of the terminators. The entire sensor is mounted on a sheet of uncured pre-preg fiber graphite by a high bond double sided tape manufactured by 3-M Corporation. The thinness of the tape and the fact that it has no plastic backing make it ideal for the sensor mounting. Curing of the pre-preg patch will occur when the tube is cured to avoid unnecessary delaminations in the structure. The center bend is the area of the fiber which will sense the strain levels and is bent to a prescribed radius. The two secondary bends serve to orient the optical fiber so that the exit connectors mount flush with the curved surface of the tube.

The tube is composed of five individually wound layers, each alternating from a hoop orientation to a helical one. The fiber lay-up for the tube is as follows: (1) the inside layer is of helical pattern, followed by (2) a hoop, (3) a helical, (4) the transducer patch, (5) a hoop, and finally (6) a helical layer. The tube with the embedded sensor is cured by rotating the part in an oven at 350 Degrees F. After the part is cured, machined, and any excess resin is cleaned from the optical fiber terminators, the sample structure is complete.

6.2 Application of the Strain Sensor to a

Filament Wound Flat Panel

For the application of the sensor to a flat panel the design of the structure is changed, but the sensor remains the same as the one used in the graphite tube. This will be the case for most applications involving the strain sensor once the proper design is found. The flat panel is fabricated on the same equipment as the graphite tube, but the shape of the mandrel is changed. For the flat panel, the mandrel is a 300 mm by 300 mm flat sheet of aluminum coated with a release agent. The graphite fibers are wrapped around the square mandrel so the fiber plies are zeros and nineties (Zero degrees from a

reference direction and ninety degrees from the same reference direction). Due to the square nature of the mandrel these are the only fiber directions obtainable.

Figure 6.2 shows the orientation of the sensor in the panel.

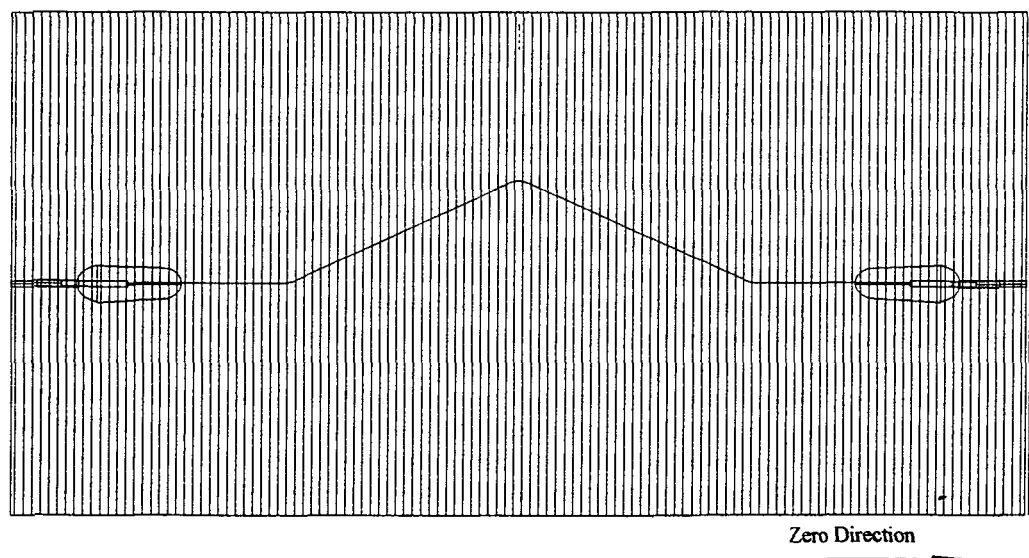


Figure 6.2. Schematic View of The Graphite Mandrel Wrapped Flat Panel

The flat panel consists of five layer of graphite with the sensor embedded three layers from the bottom. The lay-up of the structure is as follows: (1) the bottom layer is oriented in the zero direction followed by, a (2) ninety degree layer, (3) a zero, (4) the sensor patch oriented in the zero direction, (5) a zero, and finally (6) a ninety. The panel was wound using this configuration and then it was bagged, depressurized, and cured. In order for the optical exit connectors to withstand the pressure applied to the surface by the bag, sheets of high temperature rubber were fit over the connectors so they would not experience the pressure needed to cure the graphite but the rest of the part would. The sample structure was then cured in an Autoclave at 350 Degrees F.

6.3 Application of Strain Sensor to a Four Layer Polycarbonate Flat Panel

A multi-sensor test was designed to further study the optical fiber sensor's ability to detect strain. Since it has been shown that the sensor can be embedded into structural components such as graphite tubes and panels with relative simplicity, a less sophisticated structure was fabricated so that the sensor's properties could be more accurately evaluated. The four layer sample structure was constructed of a polycarbonate plastic (Lexan) and contained two separate optical fibers each with two prebends to detect strain. The panel layup and fiber configuration are shown in Figure 6.3.

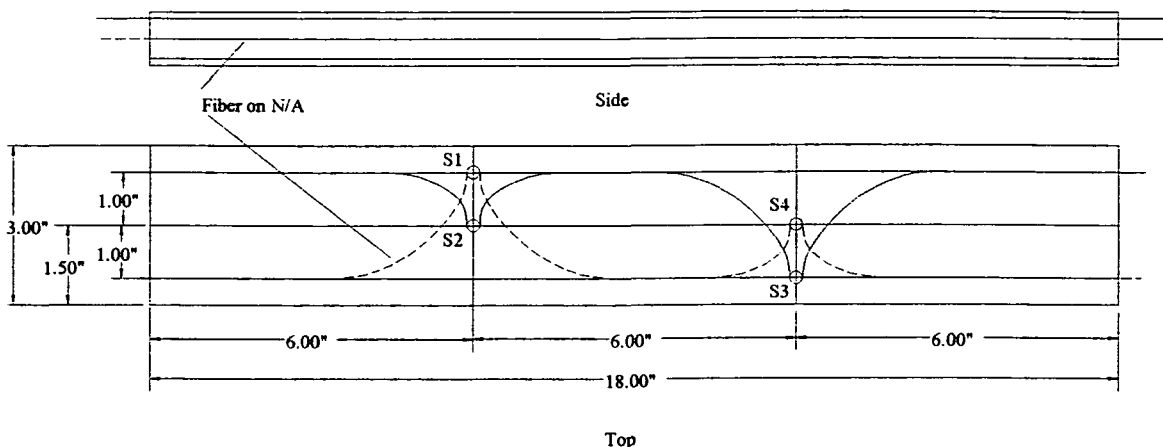


Figure 6.3 Configuration of Lexan specimen with Optical Sensors Embedded

As seen, one fiber is located on the neutral axis of the structure between two 3/8" pieces of Lexan and will be denoted as Fiber 1. A second fiber is placed 3/8" from the neutral axis of the structure and covered by a 1/8" piece of Lexan which is Fiber 2. Each optical fiber has two prebends of .375 cm radius, therefore each fiber has two areas which can detect strain. The individual prebends are considered separate strain gages so there are four gages embedded within the part. The sensors are denoted as S1, S2, S3, and S4 as shown in Figure 6.3. Sensors S2 and S4 are located at the midplane of the width of the part while S1 and S3 are at positions one inch from the midplane. Sensors S1 and S4 are on the neutral axis fiber while S2 and S3 are above the N/A. This type of configuration allows several different tests to be performed by simply changing the load position and direction of the three point bend fixture.

The layers of polycarbonate used to form the structure are bonded with methylene chloride instead of an epoxy type adhesive. The methylene chloride acts to melt the plastic which creates a homogenous structure after drying. It should be noted that methylene chloride is a chemical which can be used to dissolve the plastic buffer which surrounds the

optical fiber so a coating must be applied to the optical fiber before embedding to avoid changing the physical properties of the fiber. Once the optical fibers are mounted, the sheets of Lexan are brushed with methylene chloride, assembled, and clamped for drying.

The graphite filament wound tube, the graphite flat panel, and the Lexan flat panel will be used to study the capabilities and limitations of the embedded strain sensor.

CHAPTER 7

Evaluation of The Strain Sensor Embedded in a Test Structure

The analysis of the optical fibers sensitivity to bending leads to the need of testing the strain sensor in an actual manufactured part. The graphite tube, graphite flat panel, and the Lexan flat panel previously discussed are used as the sample structures to simulate how the sensor will behave in real loading conditions. Since it was found that the OTDRs tested could not produce the required accuracy only one bend will be used so that the maximum accuracy can be found by using CWTT testing.

Temperature tests to determine the radius of the serpentine bends embedded in the test structure were made on the graphite flat panel. The setup is similar to the one shown in Figure 4.13 except that the sample structure replaces the taper fixture. A heat source is applied to the surface of the part and temperature readings are taken on both the top and bottom surface. Two temperature readings are required since it would be difficult to experimentally determine the temperature at the center of the structure where the sensor is without damaging the optical fiber or weakening the structure. The two temperatures are used to find an average temperature which is a good approximation of the center temperature.

The tests of attenuation vs. fiber bending were performed using the three point bend fixture shown in Figure 7.1.

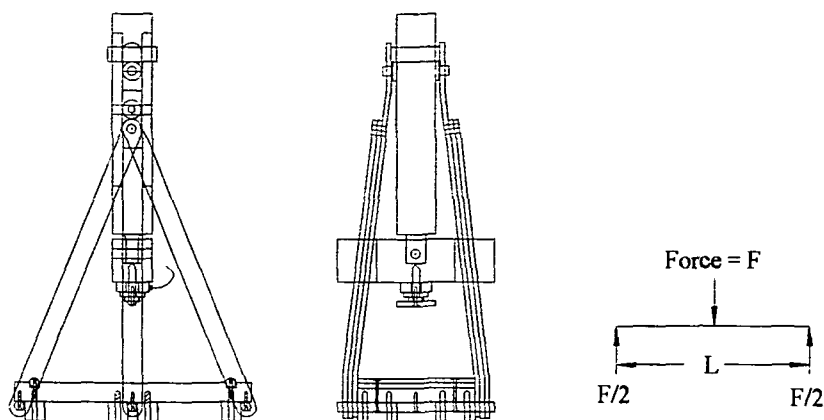


Figure 7.1. Three Point Test Fixture Used to Find the Attenuation vs. Bending for the Sample Structures

The three point bend fixture was fitted with a force transducer and deflection sensing gauges therefore stress and strain could be found for use in Equations 2.192 and 2.193 to determine the attenuation as a function of fiber radius change. The Seastar equipment was used as the laser source and the optical output power was displayed on a LeCroy sampling oscilloscope. Figure 7.2 shows the setup of the test bed for detecting attenuation as a function of fiber bend radius in the sample structures.

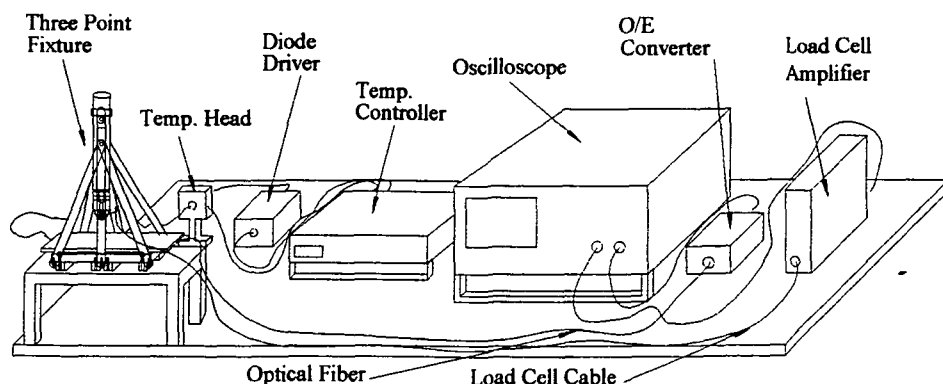


Figure 7.2. Test Setup for Determining the Relation of Attenuation to Fiber Bend Radius using a Sample Structure

Using this setup and the three sample structures, test were performed to determine the attenuation to fiber bend relations. From the temperature testing, the serpentine bend radius would be found which allows the attenuation as a function of bend radius for the structure to be compared to the theoretical attenuation values found from the taper test.

The results are outlined in the following sections.

7.1 Temperature Testing of The Flat Panel to Determine The Serpentine Bend Radius

The flat graphite panel was tested using CWTT and a heat source to determine the sensor's temperature characteristics. In the process of fabricating the serpentine sensor, a 3/8" Diameter mandrel was used to produce the bends. It has been found that the bends in the optical fiber tend to drift slightly in the curing process of the graphite material, therefore the actual fiber bend radius is slightly larger than the mandrel radius. Without the ability to determine the exact bend radius, the accuracy of the sensor would be reduced since the attenuation to strain relation is based on experimental results obtained from an unmounted fiber. The results obtained from this temperature test will be compared to the ones found in Chapter 4 of this thesis.

Figures 7.3, 7.4, and Appendix G.1 show the results of the temperature test performed on the flat graphite panel.

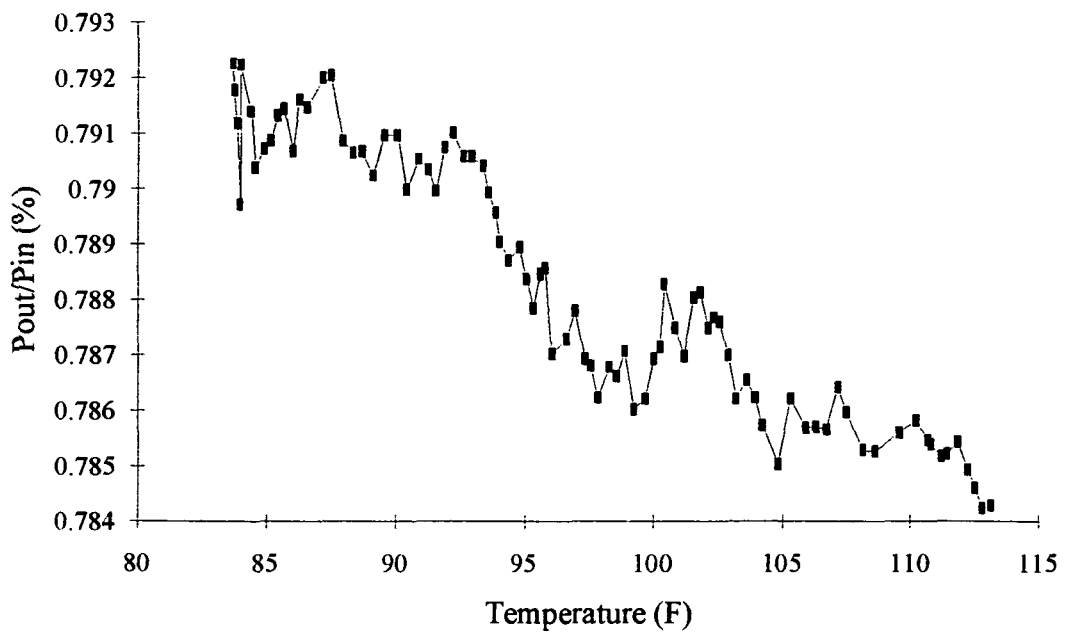


Figure 7.3 Attenuation as a Function of Temperature For the Flat Panel Sample Structure

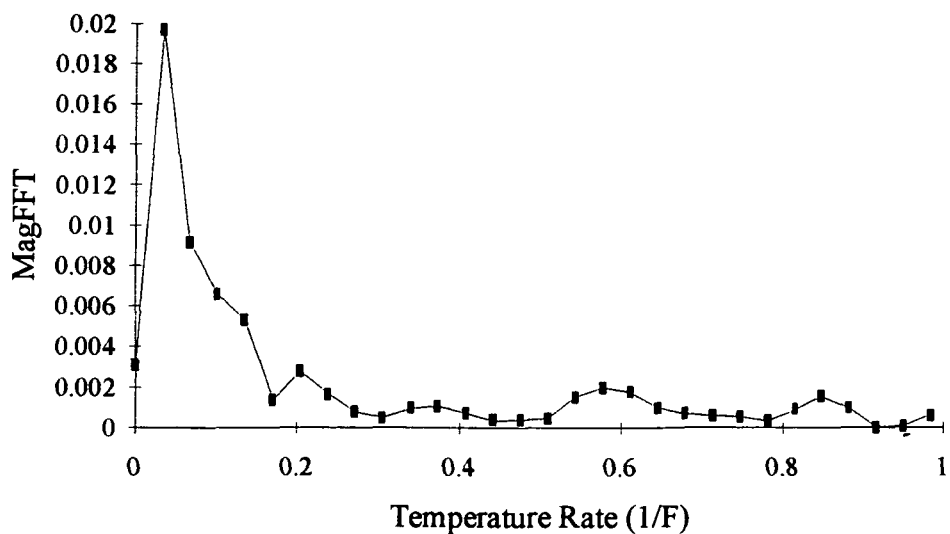


Figure 7.4 Complex Fourier Transform of the Flat Panel Temperature Data

From the temperature testing of the flat panel the mean value of attenuation is found to be .78824 with the first, second, and third temperature rates of .03395, .2037, and .3734 respectively. These values would normally be compared to a table similar to Table 4.1, but upon viewing this table it is seen that data was only taken at major locations such as Peaks, Middles, and Valleys. Also the temperature tests using the taper were not taken at radii larger than .4608 cm so the initial bend of the serpentine due to the mandrel is larger than any radii tested. Although the temperature testing presented in this thesis serves only as a guide line to the complete characterization of an optical fiber, it should be noted that the temperature test performed on the flat panel produced a mean value of .78824 with a first frequency of .03395. From the values shown in Table 4.1, the first frequency suggests that the fiber bend radius is at a position to the left of a point of synchronous coupling and at the middle of a whisper mode oscillation (see Middle 2 and Middle 4). Using the attenuation level of 78.8 percent obtained from the mean and the first frequency position, it is seen that from the theory of the temperature characterization, the bend radius should be at the center of the whisper oscillation between Valley 5 and Peak 6. From Table A.3 it is found that the mid point of this particular whisper oscillation is at a fiber bend radius of .47136 cm. This value compares very well with the radius of the mandrel used to mount the fiber which was .47625 cm.

7.2 Graphite Tube under Three Point Loading

The filament wound graphite tube with the embedded optical strain sensor was tested using the three point bend fixture. The optical fiber embedded in the tube was a 1300 nm single-mode fiber. A test of attenuation vs. fiber bend radius using the taper test was performed on the same fiber that was embedded in the graphite tube. Although the taper test is experimental in nature its results can be considered a semi-theoretical relation

of the attenuation of the fiber in the tube since the test is not actually of the fiber while in the sample structure. Since the characterization of the optical fibers sensitivity to bending was not done in enough detail, an actual serpentine bend radius is unable to be found. Because of this, the initial bend radius of 4.7625 mm made from the mandrel is used to find the semi-theoretical attenuation levels and compare the semi-theoretical and experimental data. Figure 7.5 and Appendix G.2 show the results of the attenuation vs. fiber bend radius change for the tube test.

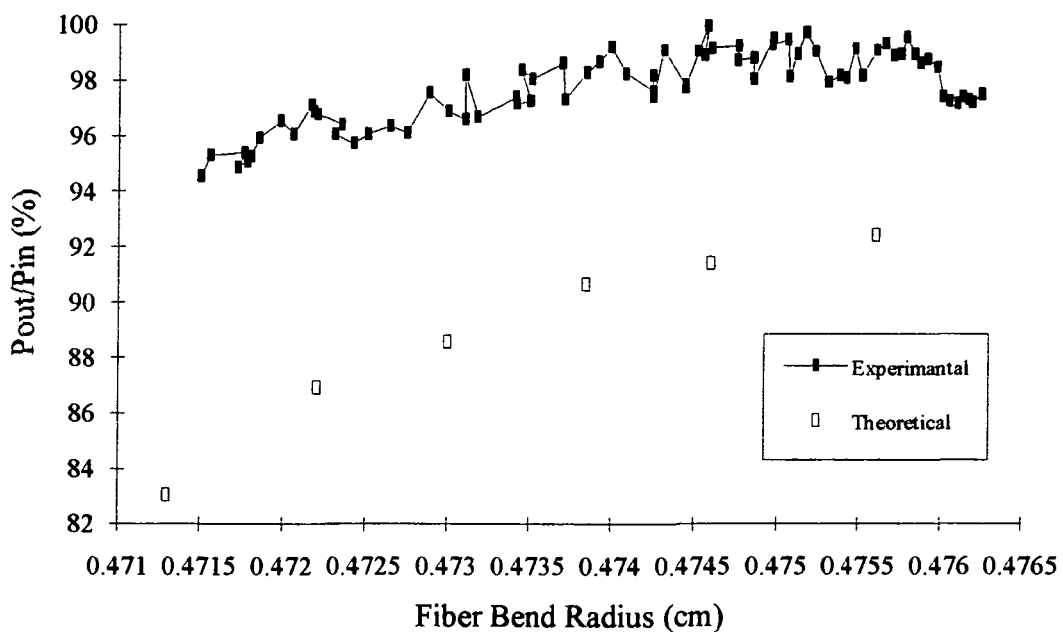


Figure 7.5. Theoretical and Experimental Results for Attenuation vs. Radius Change due to Three Point Loading of the Graphite Tube

As seen, the incremental radius changes obtainable are much smaller for the three point bending test (experimental) than for the taper test (semi-theoretical). This is simply because the radius changes using the taper can not be accurately incremented on such a small scale since the optical fiber is moved from one bend radius to another. The fiber in the graphite tube is stationary and the bending is causing the radius changes of the structure. From Figure 7.5 it is also noted that the bend radius is reduced as the structure is loaded. This is because the sensor was located at the top of the graphite tube under bending and the fiber experienced compression due to the deformation. The tube was loaded from zero lbf to approximately 1300 lbf. Both the tube and the test fixture could withstand much higher forces but since the load was not distributed across a large area, the center load point delaminated the composite and depressed into the tube.

The experimental and theoretical data for the graphite tube test show several comparisons. Although only six semi-theoretical data points are within the experimental radius change region, the maximum attenuation values are around the same bend radius for both. From Figure 7.5 it is seen that the semi-theoretical data has a lower attenuation percentage than the experimental data. If the actual serpentine bend radius was slightly larger than the approximation used to find the semi-theoretical values, the semi-theoretical data would have higher attenuation percentages since they would be closer to the top of the whisper oscillation. This suggests that the serpentine bend drifted slightly to a larger radius in the sample structure as pointed out in previous comments.

7.3 Flat Graphite Panel under Three Point Loading

The fabricated graphite panel was tested using the same setup as the graphite tube except that the source and receiver were of a different wavelength. The fiber embedded in the graphite panel was the same 850 nm single-mode optical fiber used to obtain the first correlations of attenuation as a function of bend radius with the pronounced whisper

effects (Figure 4.5). Again the theoretical comparisons are made with respect to experimentally obtained values of attenuation vs. bend radius using the taper test. Figure 7.6 and Appendix G.3 show the results of the testing flat panel with three point loading.

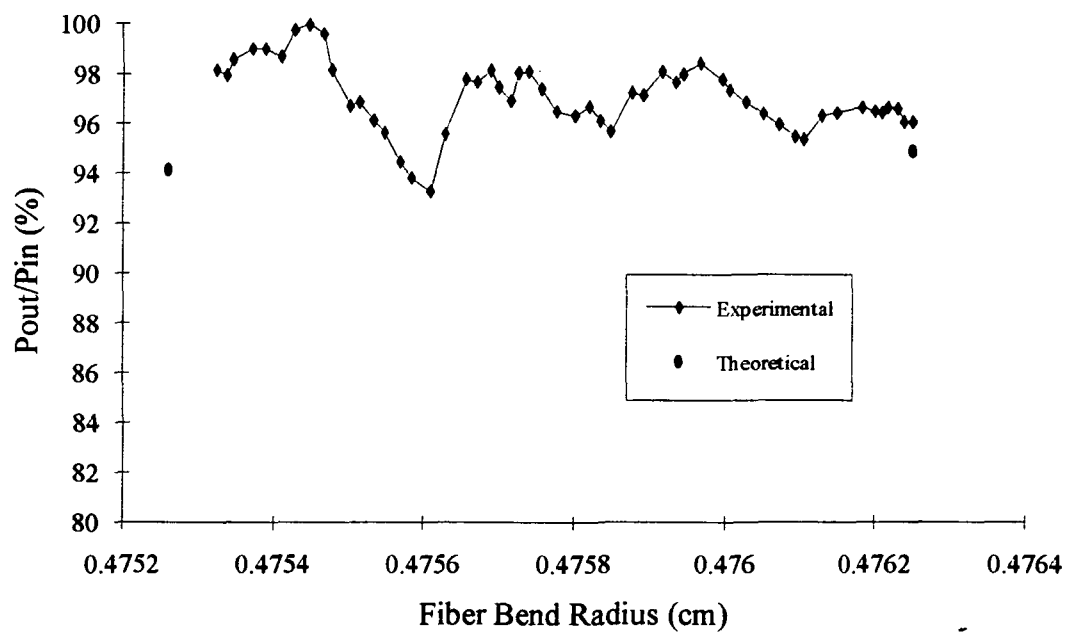


Figure 7.6. Theoretical and Experimental Results of Attenuation vs. Radius Change Due to Three Point Loading of the Flat Panel

The panel was loaded from zero lbf to approximately 50 lbf. The three point fixture was setup where there was a 10 mm spacing between the bottom two load points. This allowed for maximum deflection and accuracy while minimizing delamination due to over loading.

The results from this test have several important points. Again the theoretically obtained values using the taper test have large incremental radius changes compared to the three point bend values. This shows that characterization of the attenuation properties of the optical fiber need to be more accurate in order to describe the sensing abilities. The fluctuations noted in this test are very pronounced. Upon examination of the points of high and low attenuation it was found that the bend length due to the specific bend radii were increasing by one wavelength between each attenuation fluctuation. This suggests a wavelength dependent phase interference between two rays of light. Referring to the theory describing the Transition losses we see that these fluctuations are very similar to the descriptions of this type of loss. This idea is further supported by noting that the difference in attenuation levels for the peaks and valleys of the oscillations are on the order of the ones found by preceding researchers.

7.4 Lexan Flat Panel Subjected to Three Point Loading

The 4 layer Lexan sample structure was tested using the same setup as the graphite tube and panel. The same type of 850 nm SM optical fiber that was embedded in the flat graphite panel is also used for this test. The optical fibers were prebent to a radius of .375 cm at the test points and exited the structure as pigtailed instead of by the boot connectors to reduce any inadvertent attenuation from removable type fiber splices. Due to the multiple gage configuration of the strain sensors, different loading configurations were used to study individual sensor responses. Eight tests were performed on the Lexan structure and are labeled as T1 through T8 as shown in Figure 7.7.

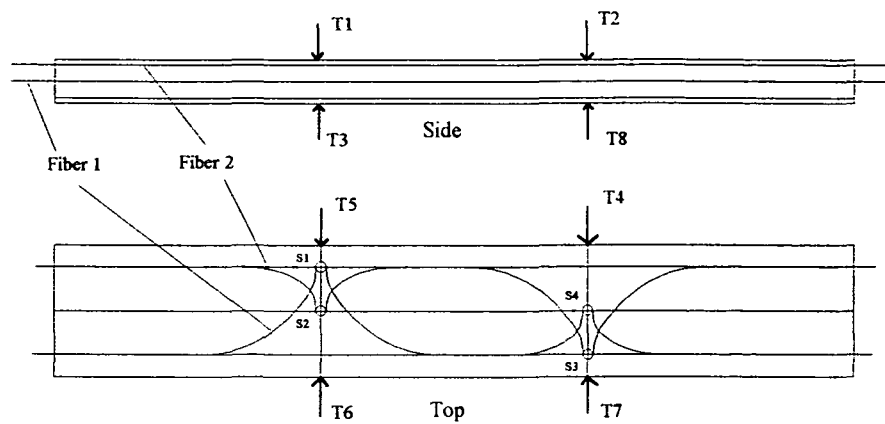


Figure 7.7 Schematic of Lexan Specimen Showing Load Test Points

For the three point tests, the center load point is directly above the serpentine prebends for each sensor. The span for the two lower bend points is eight inches so for any particular test, only one strain sensor experiences stress. Table 7.1 shows the tests performed, which sensor was active, and the type of stress seen by the sensor.

Table 7.1. Descriptions of the Tests Performed on the Lexan Specimen

Test #	Active Sensor	Fiber #	Type of Stress	Distance from Sensor to N/A
T1	S2	F2	Compression	3/8"
T2	S3	F2	Compression	3/8"
T3	S2	F2	Tension	3/8"
T4	S3	F2	Tension	1"
T5	S1	F1	Compression	1"
T6	S1	F1	Tension	1"
T7	S3	F2	Compression	1"
T8	S3	F2	Tension	3/8"

A line in Table 7.1 would read as follows: For Test 1 (T1), Sensor 2 (S2) of fiber 2 (F2) experienced compressive stress since it is above the neutral axis, N/A, of the part by 3/8 of one inch while Sensor 1 (S1) on fiber 1 saw no stress. From these tests, the behavior of the optical strain sensor will be evaluated to determine attenuation characteristics for a controlled structure.

The Lexan panel was tested using eight positions and configurations. The results will be used to make several comparisons. These are: attenuation as a function of structural loading for both the stressed and unstressed fibers at one position, Attenuation as a function fiber bend radius which will be used to compare to the whisper mode taper testing, and finally a correlation of attenuation to structural strain to show the sensors ability to detect strain. These results are presented in the following section.

7.4.1 Lexan Specimen Tests Relating Attenuation To Structural Loading

Using the three Point bend fixture from the previous testing, the Lexan specimen was tested and a correlation of optical attenuation to structural loading was developed. Figures 7.8 to 7.15 and Appendices G.4 to G.11 show the results of the three point tests performed on the Lexan specimen relating attenuation to structural loading. These appendices also contain data that will be used relate attenuation to fiber bend radius and attenuation to structural strain.

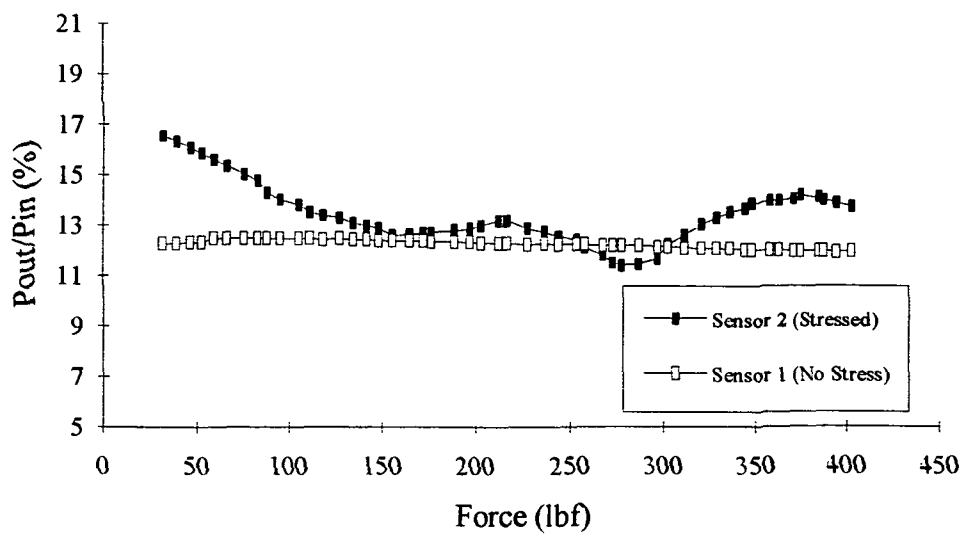


Figure 7.8 Three Point Loading of the Lexan Specimen for Test 1

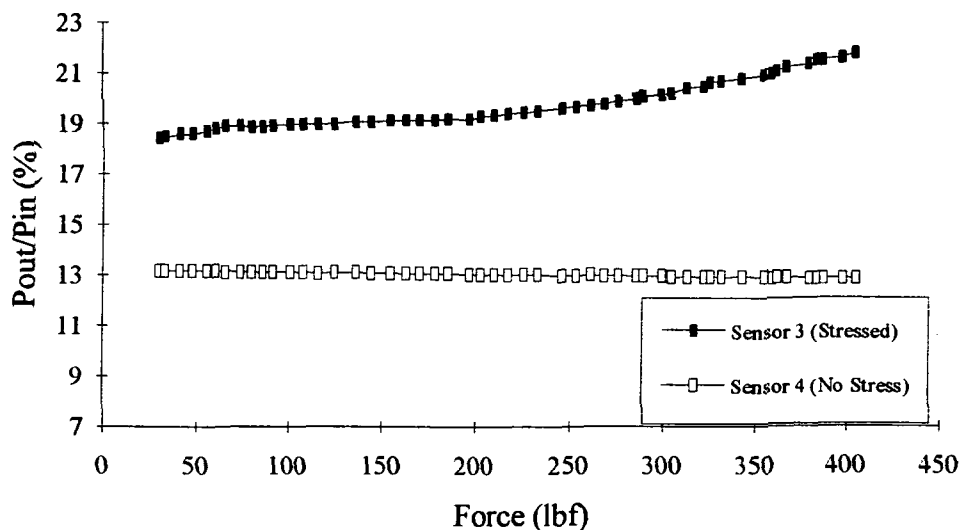


Figure 7.9 Three Point Loading of the Lexan Specimen for Test 2

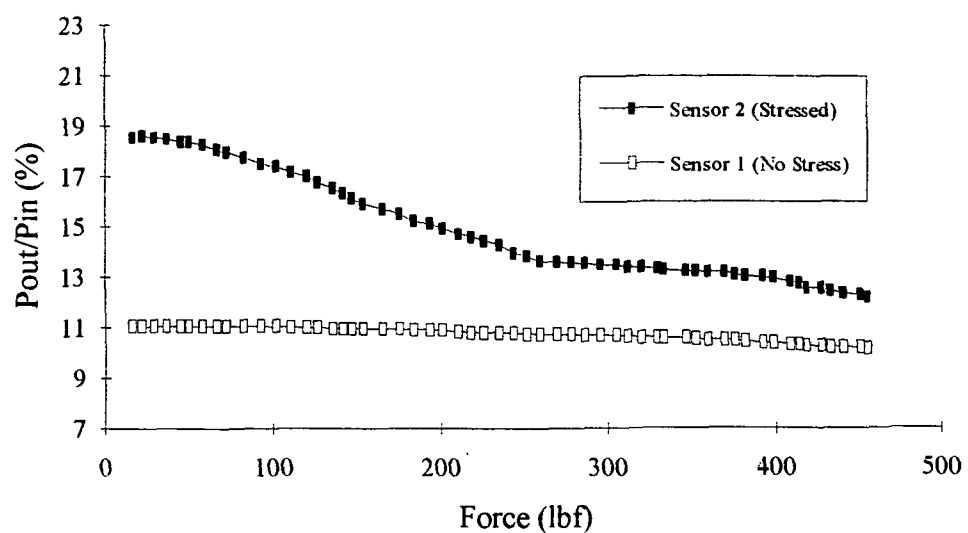


Figure 7.10 Three Point Loading of the Lexan Specimen for Test 3

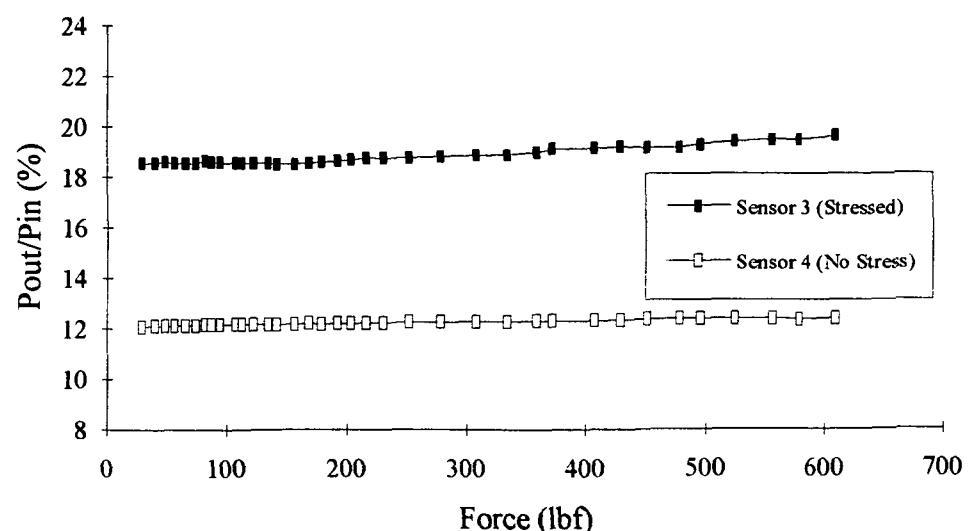


Figure 7.11 Three Point Loading of the Lexan Specimen for Test 4

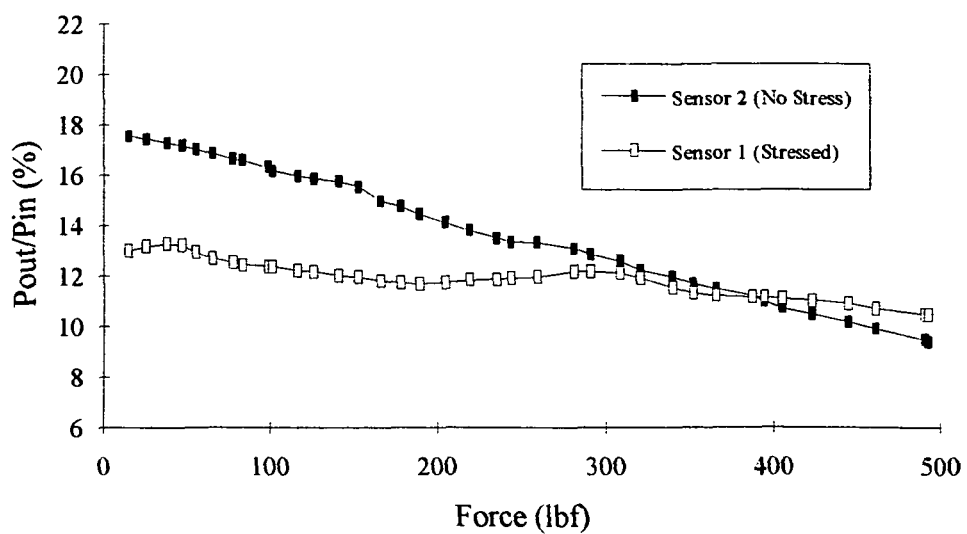


Figure 7.12 Three Point Loading of the Lexan Specimen for Test 5

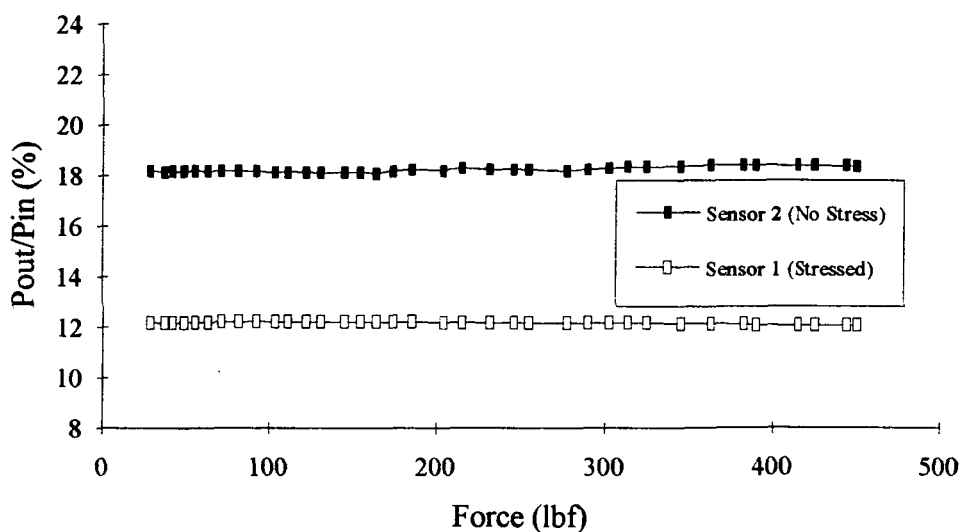


Figure 7.13 Three Point Loading of the Lexan Specimen for Test 6

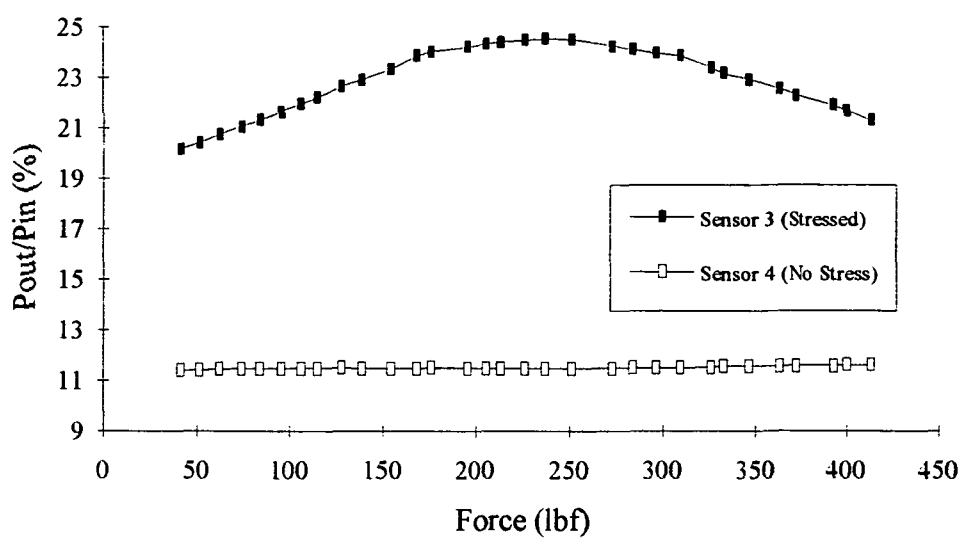


Figure 7.14 Three Point Loading of the Lexan Specimen for Test 7

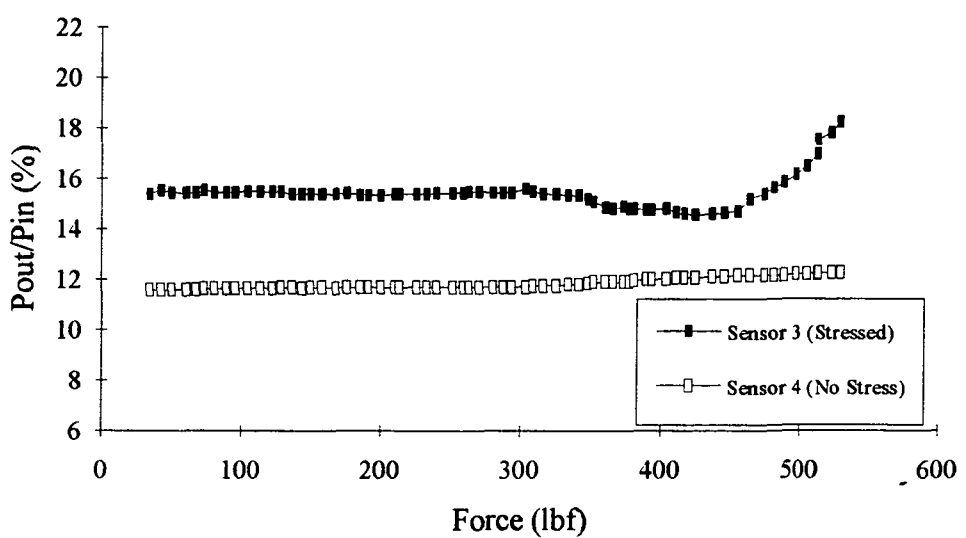


Figure 7.15 Three Point Loading of the Lexan Specimen for Test 8

As seen from Figures 7.8 to 7.15, the Lexan panel was loaded above 400 lbf in all cases but did not exceed 600 lbf. This was because previous tests of a similar Lexan specimen showed that, although theory suggested a yield strength of over 8000 ksi, the structure failed at approximately 5000 ksi. These figures show how the light in the optical fiber is attenuated as the structure is loaded. For each test, there is one optical sensor which is at a strain location and one which receives no strain. If there is no strain on the optical fiber there is no fiber curvature change. Upon viewing the setup of the bending test and the amount of load applied, it is seen that the structural radius change is too large to contribute to attenuation in the optical fiber. Thus it can be concluded that the unstrained optical fiber should not show attenuation effects due to structural bending of the sample.

The reasoning of the strain-attenuation relation mentioned in the previous paragraph can be used to determine to validity of the tests performed on the Lexan structure. In Figures 7.8 to 7.15 it is seen that both optical fibers are shown with a correlation of attenuation to load. For the sensor which is unstrained, there should be a horizontal curve indicating that there is no attenuation change due to load. In Figure 7.12, the unstrained sensor shows a significant attenuation change as the structure is loaded and therefore shows that the loading was not performed correctly. Tests 4, 5, 6, and 7 were performed with the structure loaded on the thin side parallel with the laminate layers. Due to the strength of the Lexan and this type of loading configuration, the panel was prone to tilt while under loading so the neutral axis was no longer at the center of the structure and the optical sensor experienced strain. For this reason, Test 5 is considered invalid and will not be studied further. The facts that omit Test 5 should be noted since they also lessen the accuracy of the other side loaded tests.

7.4.2 Lexan Specimen Tests Relating Attenuation to Fiber Bend Radius

Figures 7.16 through 7.22 show seven of the eight tests performed on the Lexan panel and compare optical attenuation to optical fiber bend radius. As mentioned, Test 5 was considered invalid due to poor loading conditions. For these figures, only the stressed sensor is shown. The fiber bend radius is based on the structural stress at the load point.

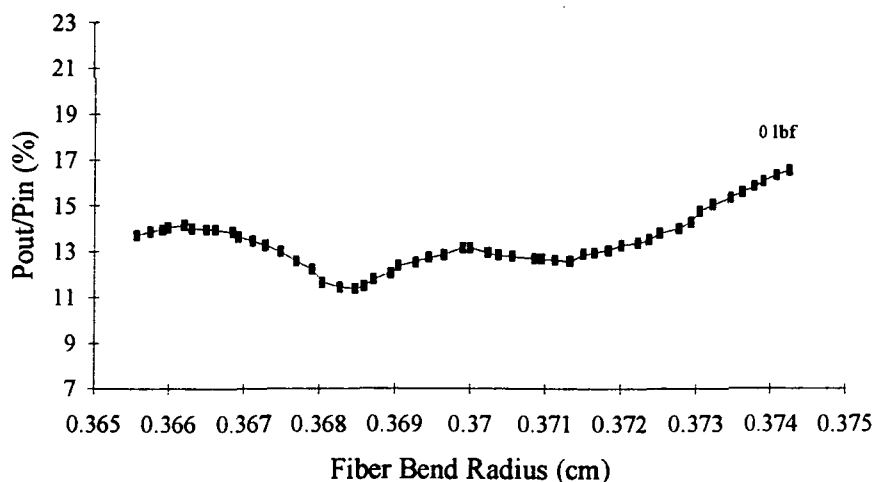


Figure 7.16 Attenuation as a Function of Fiber Bend Radius for Test 1

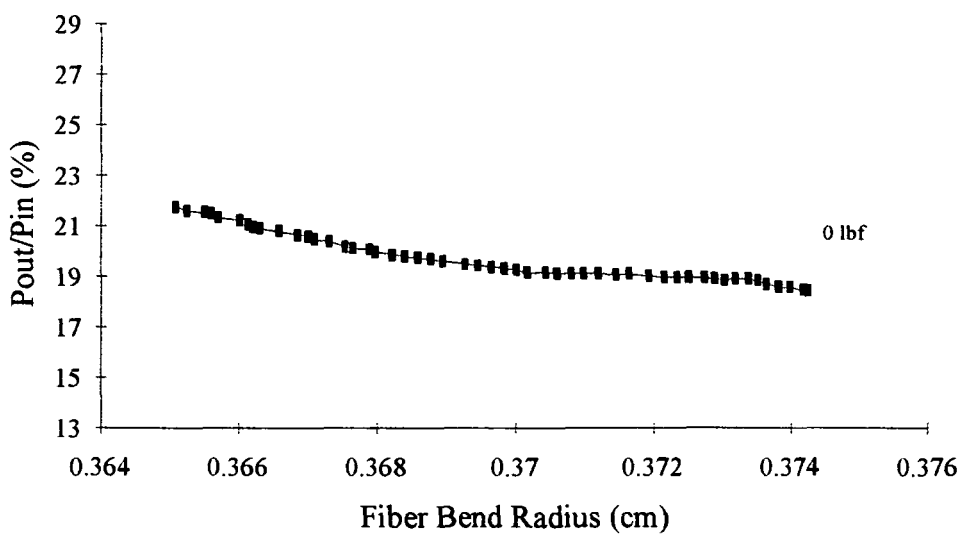


Figure 7.17 Attenuation as a Function of Fiber Bend Radius for Test 2

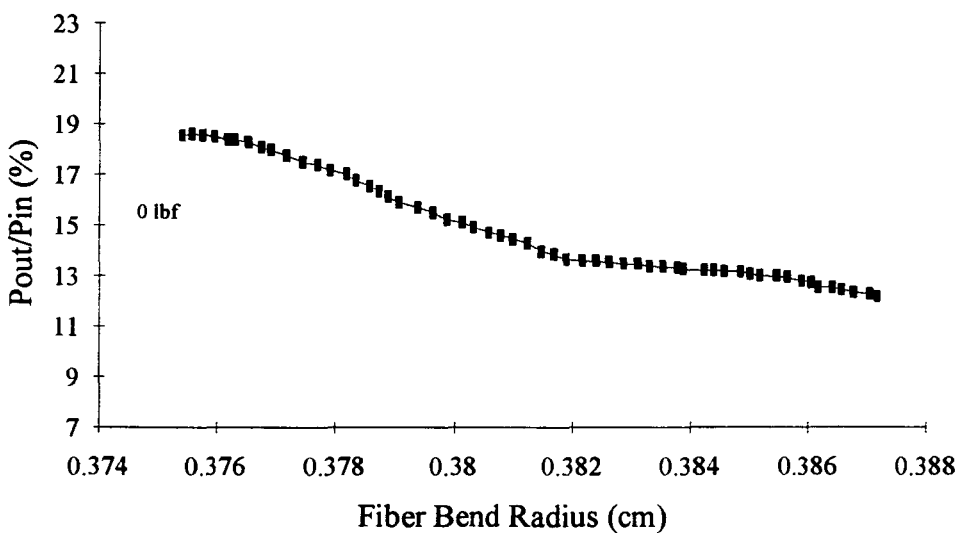


Figure 7.18 Attenuation as a Function of Fiber Bend Radius for Test 3

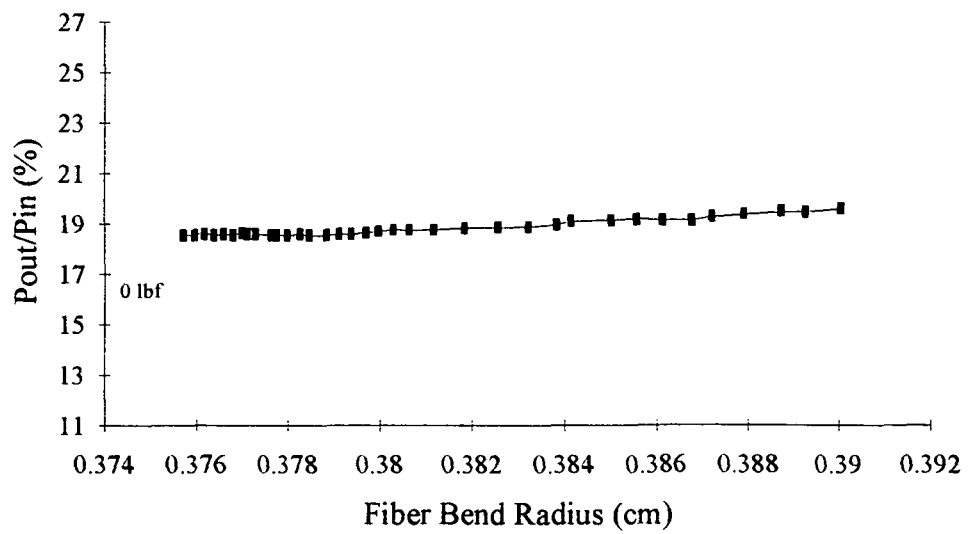


Figure 7.19 Attenuation as a Function of Fiber Bend Radius for Test 4

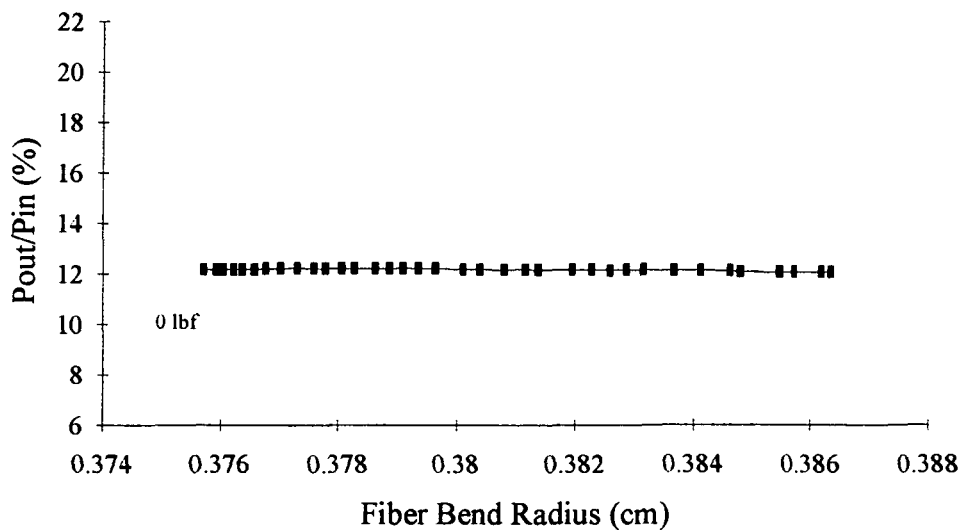


Figure 7.20 Attenuation as a Function of Fiber Bend Radius for Test 6

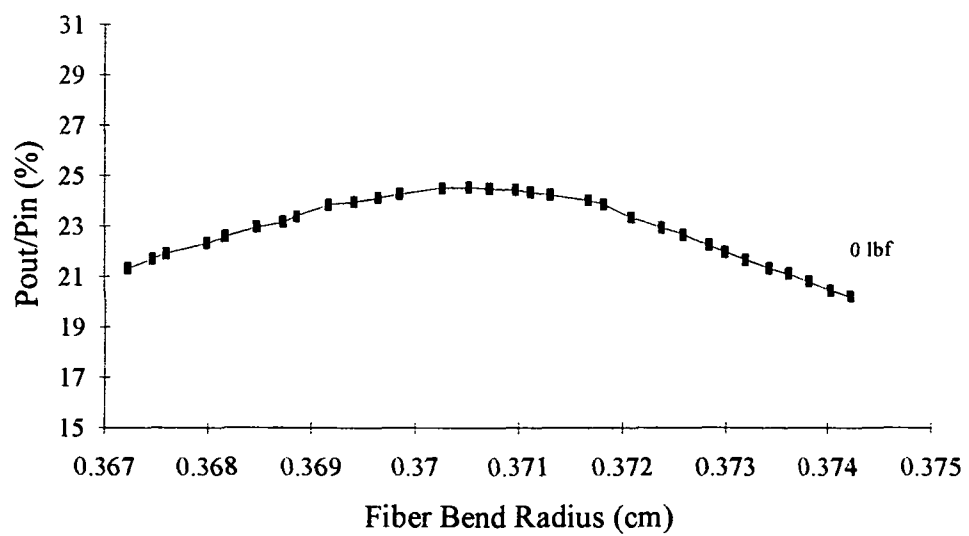


Figure 7.21 Attenuation as a Function of Fiber Bend Radius for Test 7

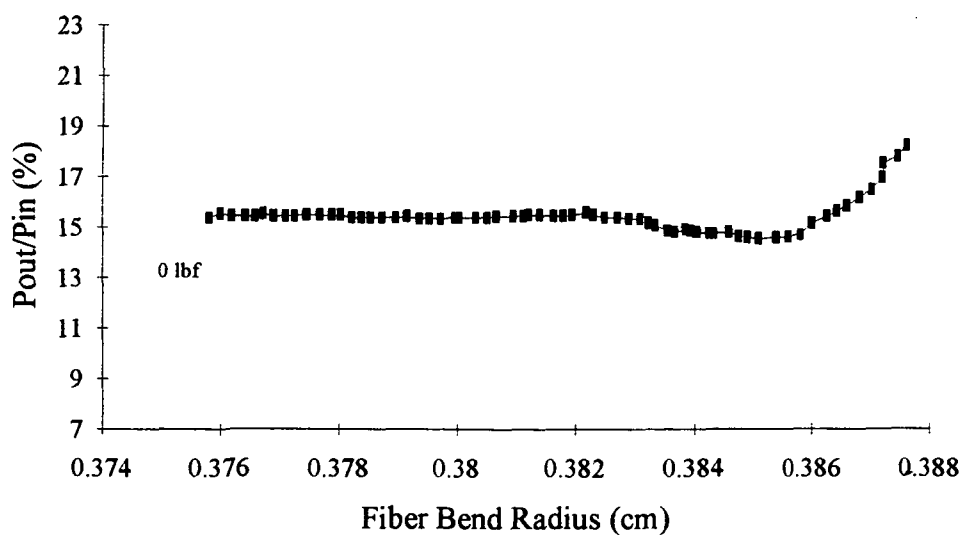


Figure 7.22 Attenuation as a Function of Fiber Bend Radius for Test 8

From these figures it is seen that the optical fiber experiences attenuation as the structure is stressed. Tests 1, 2, and 7 are stressed in compression so the fiber bend radius decreases while tests 3, 4, 6, and 8 are in tension so the bend radius increases. For all of the tests, the initial bend radius of .375 cm is used.

7.4.3 Lexan Specimen Testing Compared to Taper Test Data

Figures 7.16 through 7.22 can be compared to the semi-theoretical results of the taper test since both relate attenuation to fiber bend radius. From the layout of the optical fibers and their strain sensitive bends in the Lexan structure (see Figure 7.7) it is seen that different tests produce results on the same sensor. One test will produce tension results while another will give compression data for the same sensor. For this reason, certain tests can be shown together for a comparison of taper test and Lexan experimental data.

In Figure 7.23, Tests 1 and 3 from the Lexan specimen and the results of the taper test from Chapter 4 of this thesis (Figure 4.16) are overlaid for comparison. Tests 1 and 3 are the Compression and Tension tests respectively for Sensor 2. In order to enhance details, only a portion of the chart is shown.

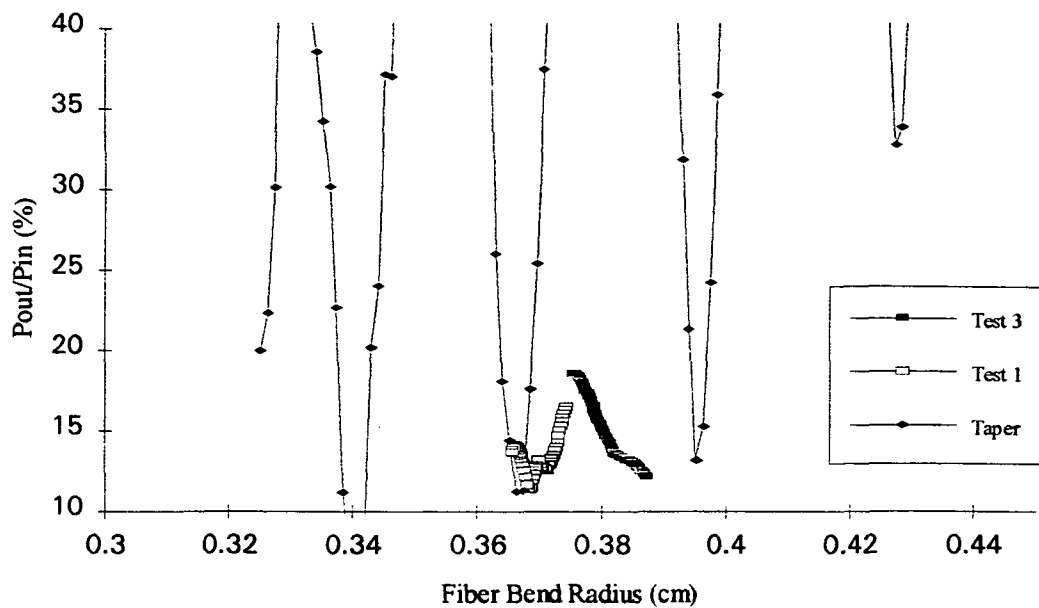


Figure 7.23 .Tests 1 and 3 from Lexan Specimen Overlaid onto Taper Test Data

Figure 7.24 shows the comparison of the taper test and Tests 2 and 8 of the Lexan Sample. Tests 2 and 8 are compression and tension respectively for Sensor 3. Figure 7.25 shows the results of Tests 4 and 7 compared to the taper test.

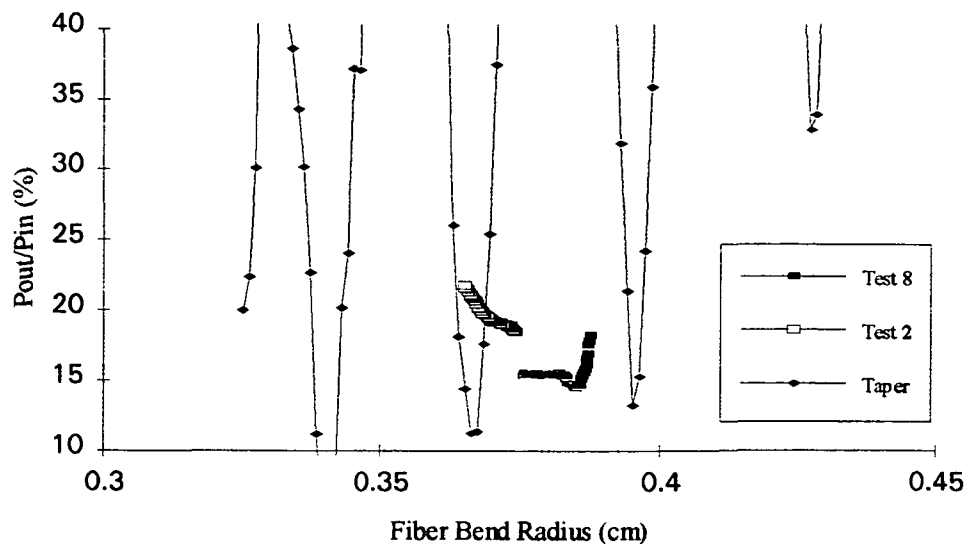


Figure 7.24. Tests 2 and 8 From Lexan Specimen Overlaid onto Taper Test Data

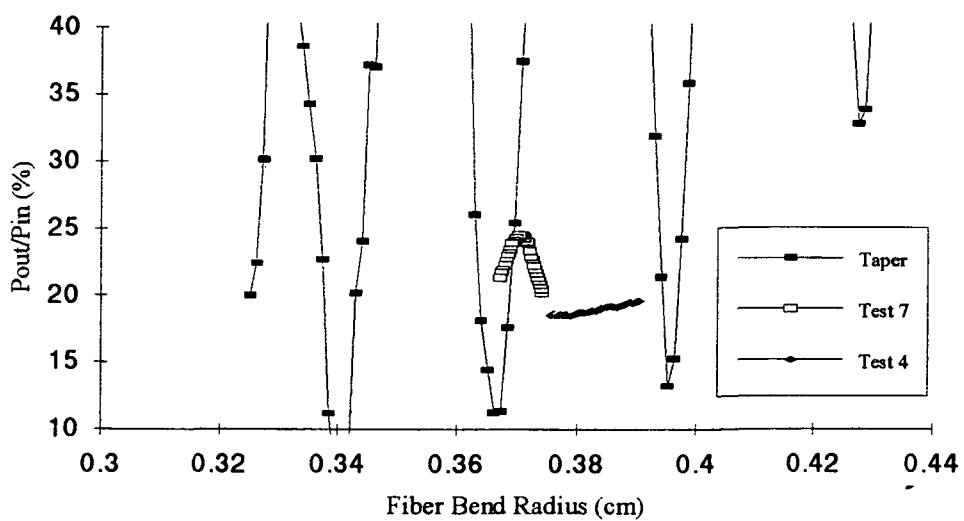


Figure 7.25. Test 4 and 7 Overlaid onto Taper Test Data

The final tests to be compared to the taper test data are numbers 5 and 6 which are Compression and Tension tests respectively and are shown in Figure 7.26. Due to the inaccuracy of test number 5 the data is not presented for comparison.

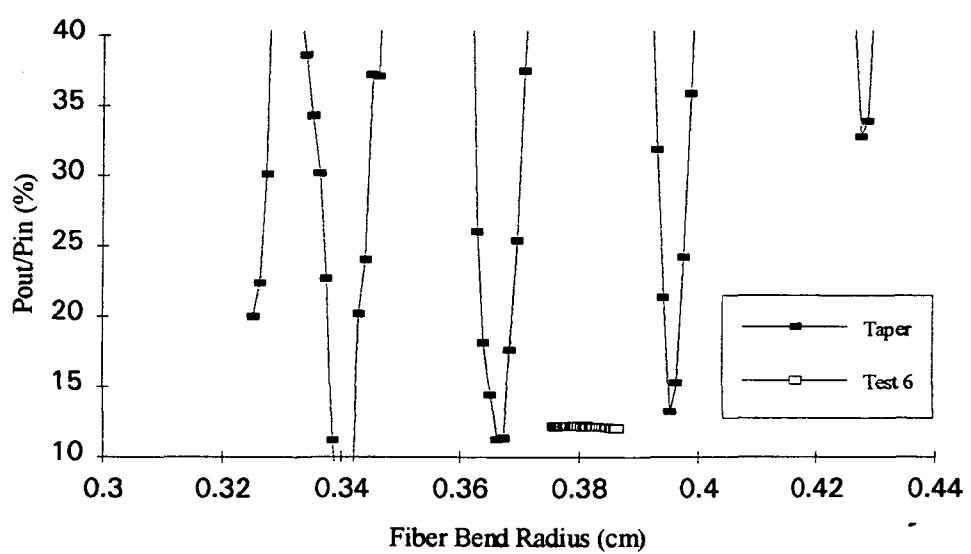


Figure 7.26. Lexan Test 6 overlaid onto The Taper Test Data

From the comparisons shown in Figures 7.23 through 7.26 it is seen that the data for the taper test has few similarities to the data collected from the Lexan specimen tests when presented in raw form. The whisper modes present in the taper test far out weigh the fluctuations shown in the specimen testing but there is still some fluctuation present.

Upon examining the physical differences between the taper test and the Lexan test it is seen that the only difference is that the buffer of the optical fiber in the taper test is surrounded by air while the Lexan test fiber is surrounded by Lexan. This difference seems to lack significance until it is realized that the interface between the optical fibers cladding and the buffer is an important factor in the Whispering Gallery mode theory (See Chapter 2 Section 2.2). Upon reviewing the structure of the Lexan specimen used in the test it is seen that the individual layers of Lexan are bonded using Methylene Chloride, a plastic solvent which softens the plastic and allows the layers to weld together. Since the optical fibers buffer is composed of a thin plastic coating, it too would be softened by the Methlyene Chloride used to bond the layers of Lexan. This would lead to a change in buffer composition which would effect the cladding buffer interface. If the interface is altered, the constructive and destructive interference between Whisper modes and the guided modes would be affected and the attenuation properties of the optical fiber would not be the same.

Since the Lexan specimen is made in separate layers and the optical fibers are bonded to the layers before assembly, optical transmission readings were taken before the specimen was assembled in order to assess the quality of the fiber placement. Upon comparing the transmission powers before and after layer bonding it was noticed that the power was dramatically reduced after curing. Comparing the values for optical attenuation for the two cases it was found that the differed by a factor of approximately 9.

Upon reviewing the laws of Reflection and Refraction it is found that a change in index of a material which interfaces another material will not affect the direction of a reflected ray but will change the amount of energy reflected. If the amount of energy reflected is reduced, the contribution of the energy from the Whisper mode to the guided mode would be reduced, thus lowering the effects of the mode interference. This would mean that the variations in attenuation over the whisper modes would be reduced and a more stable signal would be obtained.

From the previous discussion it was stated that the difference in media surrounding the optical fiber might play an important role in determining the effects of the Whispering Gallery Mode. By altering the cladding/buffer interface, the constructive and destructive interference of the whisper mode to the guided mode could be changed which might reduce the attenuation fluctuations. Referring to Figures 7.23 through 7.26 it is seen that this could be the case with the Lexan tested optical fibers but, the details are hidden by the attenuation differences.

Since it was decided that the only effect of changing the interface would be the change in attenuation level, an attenuation correction factor was applied to the data for the Lexan tests. This factor, which will be referred to as the interface correction factor, is used to compare embedded optical fibers with an optical fiber surrounded by air. The correction factor is not used to scale the level of attenuation, it is used to scale the effects of the whisper mode. Therefore if there were no whisper modes present in a set of data, the correction factor would not greatly affect the data. This is accomplished by subtracting the attenuation offset from the data, multiplying the correction factor by the whisper fluctuation, and then adding the offset back to the data.

In the following figures, an interface correction factor of 9 was applied to the data from the Lexan tests. Appendix G.12 provides the numerical data of the tests both with

and without the correction factor applied. Using this method, the whisper attenuation levels obtained in the Lexan tests are multiplied by 9 in order to compensate for the energy lost due to the interface change. Figure 7.27 shows the corrected data for Tests 1 and 3 of the Lexan specimen compared to the taper test. Figures 7.28 through 7.30 show the results of applying the interference correction factor to the Lexan tests 2, 8, 4, 7, and 6.

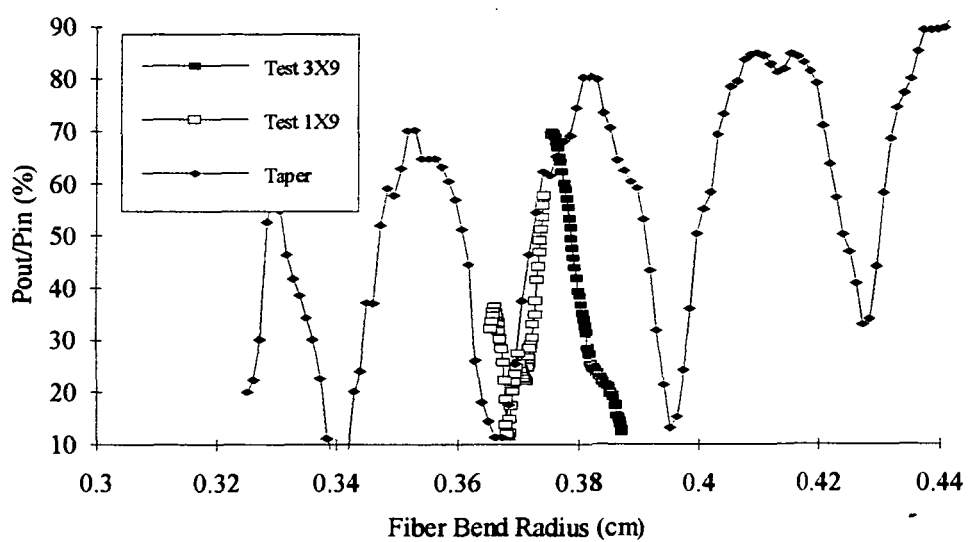


Figure 7.27. Comparison of Taper Test With Corrected Data from Lexan Tests 1 and 3

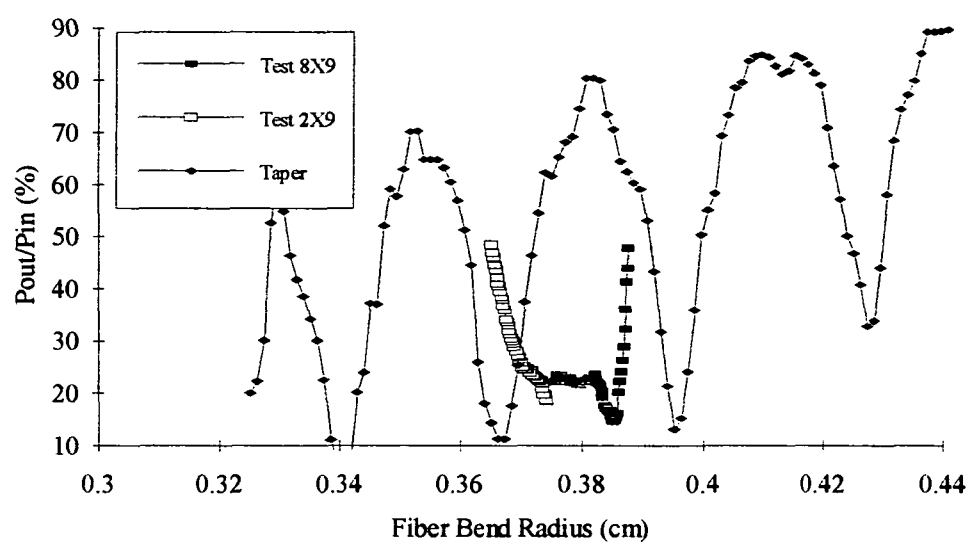


Figure 7.28. Comparison of Corrected Lexan Tests 2 and 8 to The Taper Test

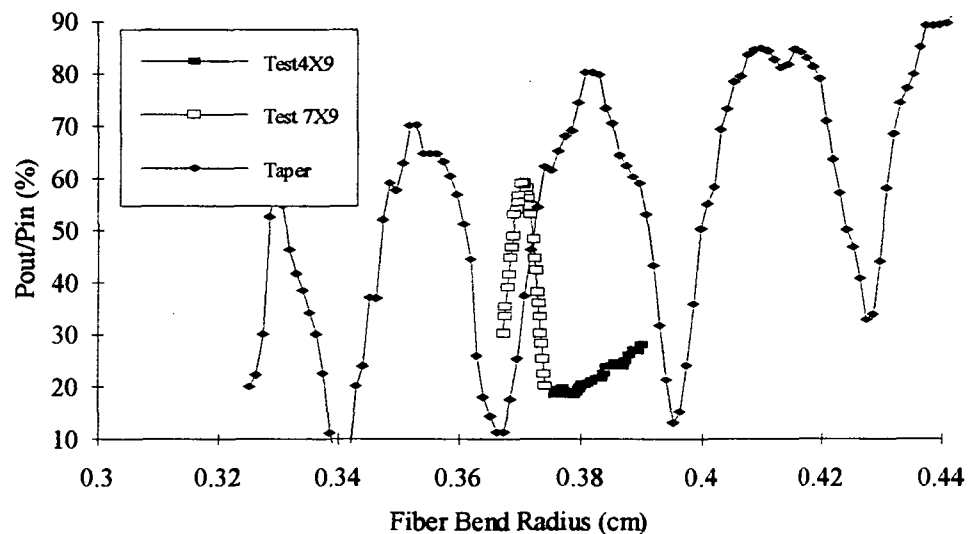


Figure 7.29. Comparison of Lexan Tests 4 and 7 to Taper Test

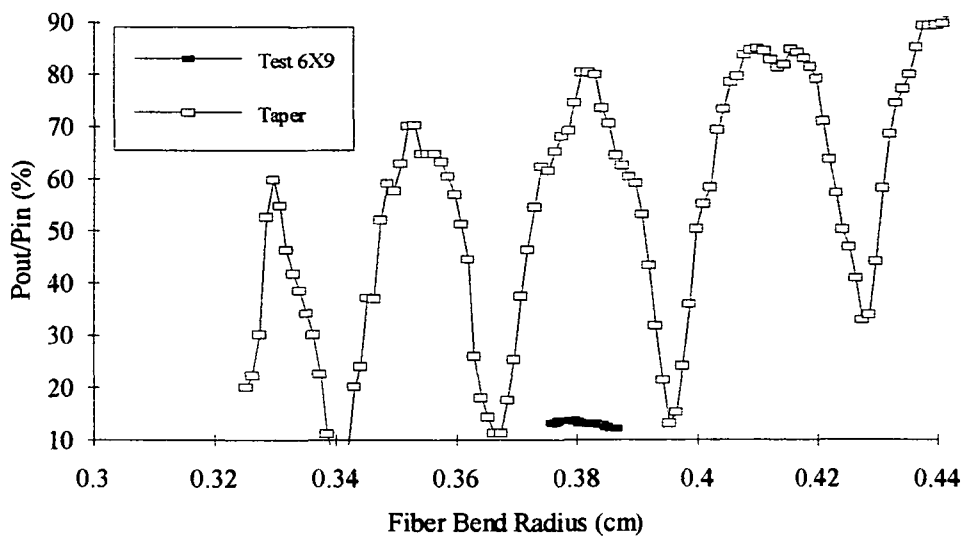


Figure 7.30. Comparison of Lexan Test 6 and Taper Test

From Figures 7.27 through 7.30 it is seen that by applying the interface correction factor to the data from the Lexan tests, the effects of the whisper modes are more pronounced and compare better with the initial taper tests of an exposed fiber. Figures 7.27 and 7.28 show excellent comparisons between the taper test data and the Lexan test data. The notable differences between the tests are: the radius values which correspond to peaks of the whisper mode, the height of the whisper mode fluctuations, and the radius increment between peaks of the whisper mode. These differences will be discussed in Chapter 8 of this thesis.

7.4.4 Lexan Specimen Tests Relating Attenuation To Structural Strain

Using a controlled test such as the Lexan panel testing , a good approximation of the structural strain can be formulated from the physical properties of the structure even with the addition of an embedded optical fiber. This is because the method of bonding the layers of the polycarbonate produces a uniform bond without the introduction of bonding

agents. Also the Methylene Chloride softens the polycarbonate so that the optical fiber embeds into the layers as the specimen dries so the layers are not separated by the fiber.

Since the final result of the characterization of optical attenuation is to produce a strain sensor, the structural strain of the Lexan specimen is compared to the optical attenuation of the sensor. Figures 7.31 through 7.37 show how the optical attenuation correlates with structural strain.

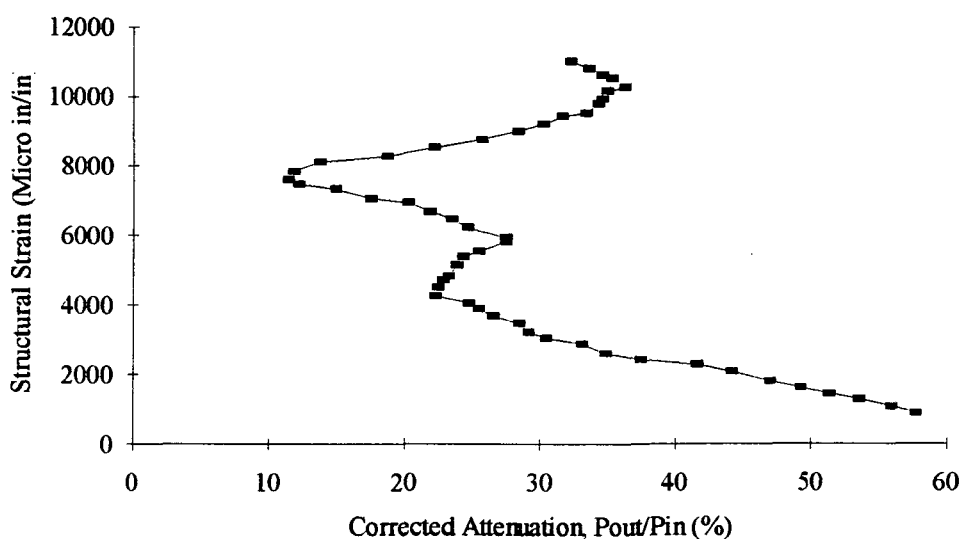


Figure 7.31. Structural Strain vs. Attenuation For Lexan Test 1 (Compressive Stress)

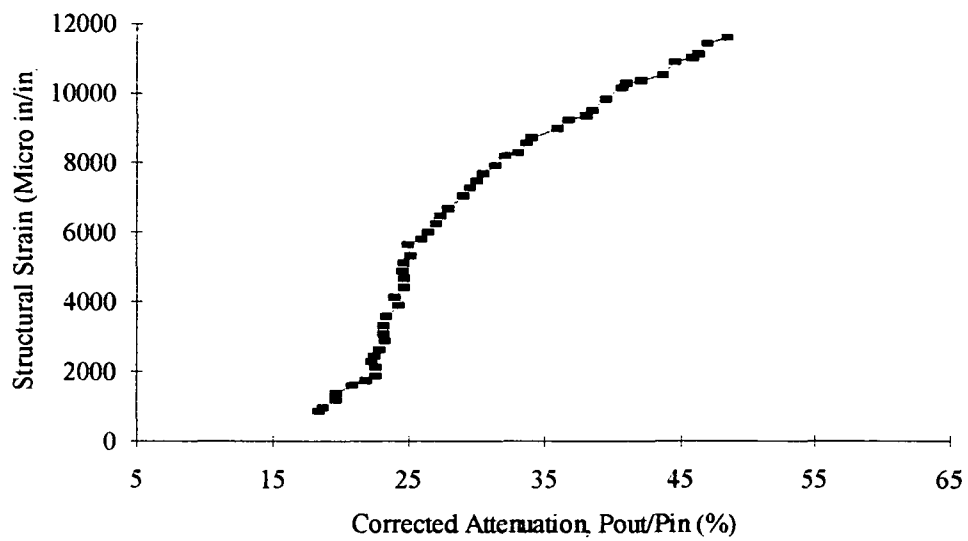


Figure 7.32. Structural Strain vs. Attenuation For Lexan Test 2 (Compressive Stress)

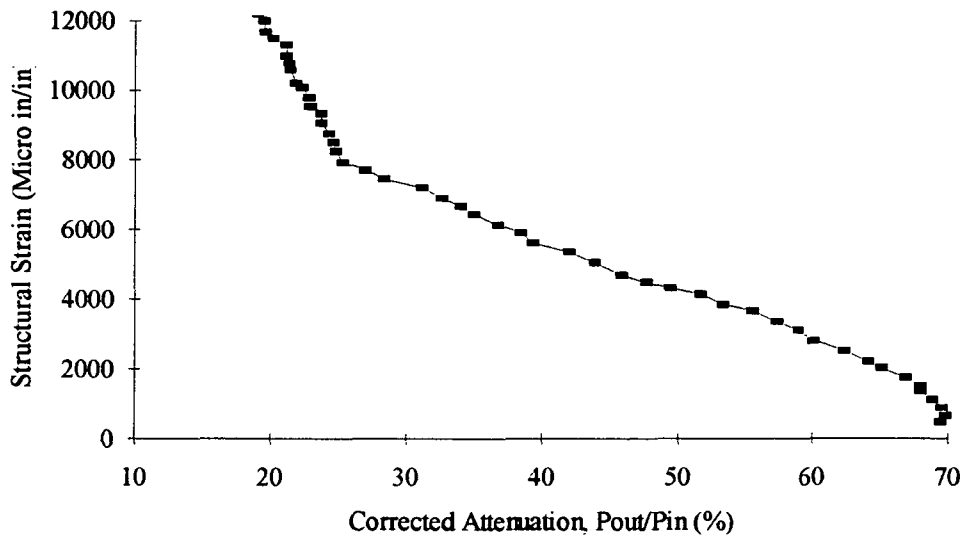


Figure 7.33. Structural Strain vs. Attenuation For Lexan Test 3 (Tensile Stress)

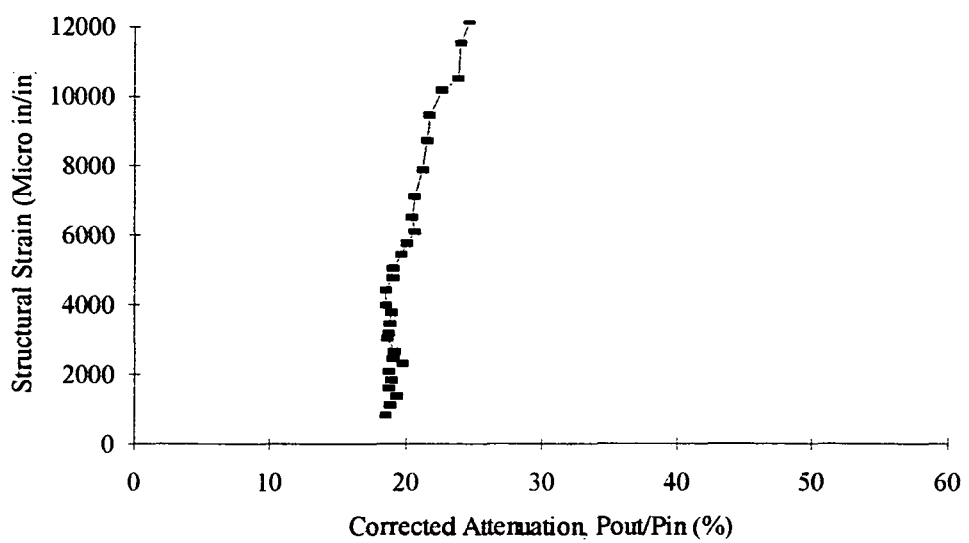


Figure 7.34. Structural Strain vs. Attenuation For Lexan Test 4 (Tensile Stress)

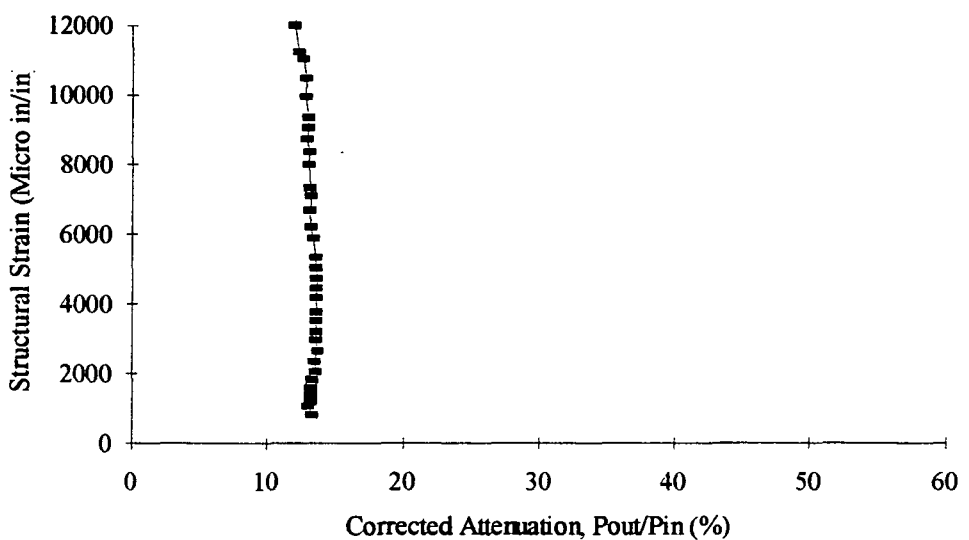


Figure 7.35. Structural Strain vs. Attenuation For Lexan Test 6 (Tension)

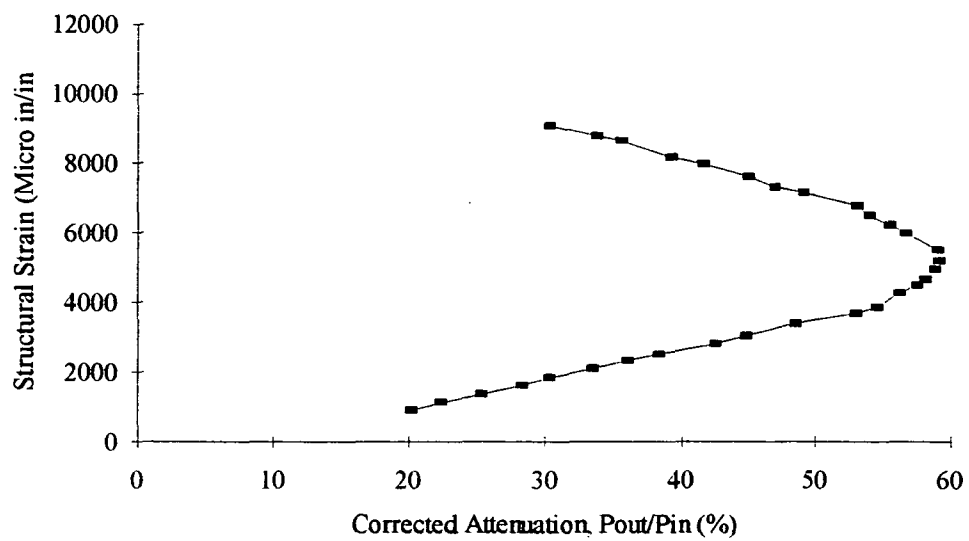


Figure 7.36. Structural Strain vs. Attenuation For Lexan Test 7 (Compression)

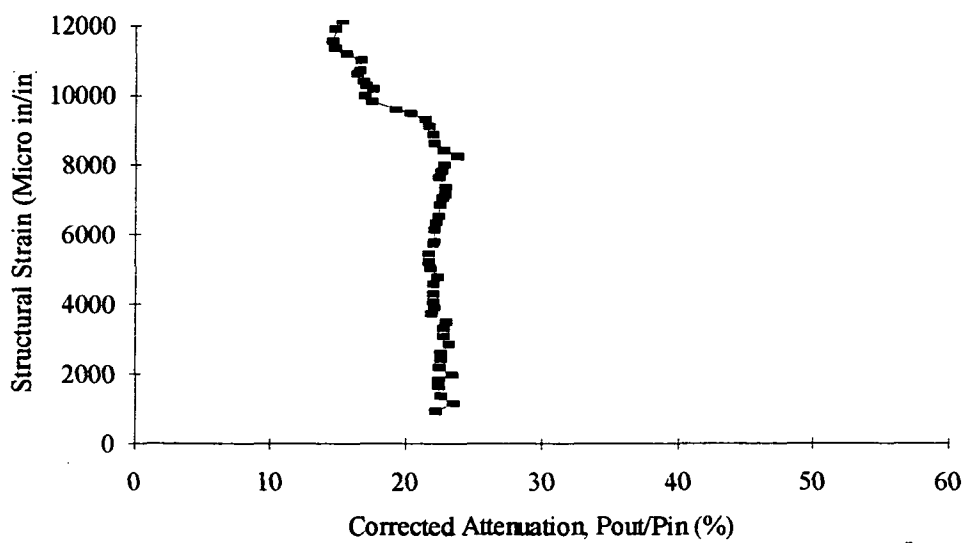


Figure 7.37. Structural Strain vs. Attenuation For Lexan Test 8 (Tension)

Figures 7.31 through 7.37 show the relation of strain to optical attenuation. The data shows a range of strains from 0 to 12000 micro strain (micro in/in). In Figure 7.31 it is seen that the optical attenuation varies linearly with strain up to approximately 4000 micro strain. If viewed on an attenuation versus bend radius chart, this area would correspond to the side of a whisper mode fluctuation. Figure 7.32 shows a correlation which is not as linear as test 1 but still possesses a simple function through 12000 micro strain and it is interesting to note that this range of strain detection is much larger than typical strain gauges can withstand without failure of the strain detector. Similar results were obtained for Test 3, which is the same sensor as Test 1 but loaded in tension. Tests 4 and 6 did not provide useful correlations between strain and attenuation since the optical power was not greatly attenuated over the strain range tested. Tests 4 and 7 use the same sensor as Tests 2 and 8 so these tests can be compared. Tests 4 and 8 produced little attenuation changes until high strain levels were reached. This leads to the conclusion that the sensor was either not responding due to mounting errors or that the initial bend radius was at a position where the whisper mode has a peak or valley and would not attenuate the light. In comparing Tests 2 and 7 it is seen that Test 2 is exponential shaped while Test 7 is parabolic in nature. Since the loads applied to the structure were not high enough to deform the specimen and the optical fiber did not lose transmission, the loading conditions must have been poor for test 7 which is a side loading condition. This problem was previously addressed in this thesis and should be taken into consideration when studying the results of Tests 4, 5, 6, and 7.

From the testing of the Lexan specimen it is seen that although the optical attenuation is not a linear function over the complete load range tested, there are ranges of strain which have simple linear correlations to the optical attenuation.

CHAPTER 8

Conclusions and Recommendations For Future Research

In the study of optical fibers as strain sensors, both the descriptions of energy propagation and the results of sensor testing are very complex. For this reason, the discussion of the mathematical models, analytical derivations, and the experimental development were started from basic principles. Descriptions of test procedures and example scenarios, setups, and types of equipment were also used to simplify the procedures involved in the thesis. Some of the conclusions that can be made from the testing are presented in this chapter along with research recommendations that will bring further insight into the problems of the whispering gallery mode and transition losses and eventually lead to the development of a usable strain sensor.

From Chapter 2 it was found that the attenuation of light as a optical fiber is bent is composed of two separate losses, namely transition losses and pure bend losses. Since the strain sensor is based upon the optical fibers sensitivity to bending, detailed evaluation of these losses was made and the result was that both possessed oscillatory attenuation functions as the fiber was bent. The transition losses produce attenuation oscillations on the order of .2 dB while the oscillations present in the pure bend loss were much larger. Due to the extreme nature of the pure bend oscillations they have been studied in detail [4] and found to be caused by a whispering gallery mode combining with the guided mode in the optical fiber. Both types of bending losses were found in experimental research for this thesis. The whispering gallery modes found in Reference [4] were not experimentally tested as thoroughly by Harris and Castle as the testing for this thesis therefore details of the mode are much clearer now. Although more experimental data was collected for this

thesis, all of the properties theorized in [4] were still in excellent agreement with the test results presented in this thesis.

Several tests were reported in Chapter 4 and used to evaluate the bending losses. Singlemode and multimode fibers were tested with both matching and non-matching fiber and source. It was found that for the singlemode fiber, as the number of data points taken for a test was increased, the whispering effects were more pronounced. The whisper modes were present in all of the tests to the same degree, but the increments of the data points determine how much of the fluctuation will be detected. The tests conducted using 125 and 184 data points shows that, although the mean of the attenuation curve is logarithmic, the whisper modes yield unsatisfactory results. The test using 125 data points shows the oscillations higher in magnitude than the test with 184 data points because the peaks of the oscillations occur at radii closer to the test values for the 125 data point test. Note that if the initial test data (Figures 4.2) were overlaid onto Figures 4.5, it would be seen that the data corresponds to the curves at the near centers of each whisper peak. This shows that the initial tests were accurate, but were not conducted with a small enough increment to detect the whispering effects. The test conducted on the 850 nm SM fiber using 270 data points showed the same effects of the whisper mode even though the test was performed almost a year later using a different laser diode. This helps to validate the stability of the mode coupling and shows that there is not a dependence on the laser source but a dependence on the fiber.

From Figures 4.5 through 4.10 it can be concluded that the whispering modes occur consistently at certain radii for separate configurations of fiber and laser and that they are dependent upon the selection of fiber and laser combinations.

The tests performed on various fibers using the different laser sources provide the following conclusions:

(1.) When the fiber wavelength is less than the laser source used, the light is not uniformly transmitted through the fiber. A bend in the fiber acts to strip the higher modes of the laser source and allow a moderately stable signal to be transmitted, but in the absence of bends the fiber transmits light erratically.

(2.) A large number of data points at different radii are required to accurately test the effects of bending the SM optical fiber. The whispering effects are overlooked when the increments between the data is large.

(3.) The singlemode fiber exhibits higher attenuation than the multimode fiber for all of the bend radii tested.

(4.) The MM fiber did not seem to exhibit the whispering mode found to be present in all of the SM fibers, but the many modes present in the MM fiber caused the light to experience an unstable jitter.

(5.) A bend in the MM fiber, no matter how small, could not fully attenuate the light transmitted through the fiber. The attenuation in the MM fiber was due to mode stripping caused by bending the fiber and the higher modes being lost to cladding modes.

Table 4.1 shows several useful properties of the optical fiber from the frequency analysis of the heat test. It is noticed that the different whisper mode position types have a different 1st frequency. The 1st frequency values for the Peak positions are all very similar. This is also the case for the Valley positions. If the Middle positions are separated into two groups, each group has similar 1st frequency values. One of the Middle groups corresponds to the positions to the left of a synchronous coupling point while the other is to the right of a synchronous coupling point.

Comparing the 2nd frequencies for the Middle position it is seen that the value of the frequency increases as the bend radius increases for both of the types of Middle positions. This is also true for the 3rd and 4th frequency values. This comparison can

also be made for the test of the flat panel since the bend radius was found to be close to the middle of a whisper oscillation. Although the bend radius of the fiber embedded in the flat panel was higher than any radius tested in the temperature correlation study, the fiber still had a first frequency which matched the ones found in the testing. Also the second and third frequencies were larger than the ones obtained for smaller fiber bend radii which helps to confirm that these frequencies increase with increasing fiber bend radius.

From the correlation between attenuation and temperature change and the temperature rates, information can be obtained which defines what the initial radius is for the serpentine fiber mounted in or on a structure. Specifically, the temperature frequencies define what part if the whisper oscillations the radius of bend is on (Peak, Middle, or Valley) and the mean value of the temperature oscillations describe a line which crosses the whisper oscillations. With reference to Figure 4.17, when these two criteria are met the initial bend radius of the optical fiber for the strain sensor has been identified and quantified. The test of the temperature footprints are only preliminary research used to describe a method of calibration, but the temperature testing performed on the flat panel showed accurate results in both mean and frequency values when compared to the fiber bend radius produced by the mandrel. A complete mapping of the whispering gallery mode effects on attenuation as a function of fiber bending would be needed to fully describe the optical fibers behavior.

From the testing in Chapter 5 of the reflectometry methods of attenuation sensing it is seen that there is still a need for equipment development which can produce the required accuracy for strain sensing. Due to the design of the typical OTDRs, they lack the ability to sense the minute variations in the attenuation as a function of bending needed to correctly describe the relationship. The PCR equipment is theorized to posses better accuracy in attenuation response and also has the advantage of higher position resolution

down the length of the fiber. Although the configuration of the PCR tested could not produce the required results, equipment design suggests that this is the type of equipment that would be needed to sense the small changes in attenuation found for this type of strain sensing.

The use of the PCR and CWTT in conjunction would be a means of more accurately describing the strain of a structure. The CWTT method could be used to obtain a summed dynamic strain for the series of sensors on one fiber while the PCR would be the means for locating residual damage after a dynamic event. The CWTT method could also be used as a trigger to tell the PCR when to determine the strain of the structure.

From Chapter 6 it was found that the optical strain sensor can be easily configured for use in a variety of structures. The sensor can be embedded into any structure which is composed of layers. The sensor can be configured to exit from virtually any surface of a structure by means of the exit terminator/connector developed (See Appendix F for more information).

In Chapter 7 it was found that the optical sensor possesses a correlation between temperature and attenuation when embedded in a structure. Although the work performed on the temperature characterization in this thesis was preliminary research, the flat graphite panel was tested experimentally and the results of the temperature testing agreed well with the semi-theoretical results.

The three point load testing performed on the various sample structures provided interesting results which compared well with previous research and theory. The testing performed on the graphite filament wound tube and the graphite flat panel showed that more research needs to be performed on the structures in order to evaluate the effects of embedding optical fibers within the multilayered graphite structures.

Testing performed on the Lexan sample structure provided insight into how the optical fiber reacts to being embedded into structures. With multiple sensors embedded into the structure, a variety of information was obtained which correlated well with theory and semi-theoretical results. Although the validity of some of the tests, specifically Tests 4, 5, 6, and 7, were questionable due to the equipment used and the load conditions, several tests had only a few sources of error and the results were in agreement with theory. The Lexan testing showed that the optical fiber was very responsive to strain but each sensor had different strain to attenuation correlations although the sensors were embedded with approximately the same initial bend radius. This shows the need for an initial bend determination using a method such as the temperature characterization.

It was also found that the optical fibers levels of attenuation varies with different surroundings. For the Lexan specimen the sensitivity of the optical fiber was reduced by a factor of 9 by embedding the fiber into the Lexan structure. The interface correction factor can be used to compensate for the different surroundings, but this function has not been evaluated to determine its validity or its value for different materials. The comparisons made between the semi-theoretical taper testing and the Lexan specimen testing were in good agreement, but some differences were worth noting. The positions of whisper peaks and valleys were slightly different for the taper testing and for the Lexan testing. Part of this discrepancy is due to the pre loading of the force transducer needed to level the load head on the three point equipment. The preload was not compensated for so the load is slightly larger than the load used to calculate stress. This is evident in the tables of Appendix G. This causes the compression data to show a larger initial radius than it actually has and tension data to show a lower radius than actual. If the data had been properly corrected, the peaks of the Lexan tests would be separated more and would compare better with the taper test data. Since it was found that none of the optical

sensors provided the same correlations of attenuation to strain it is evident that the radii were different for each sensor. Since the temperature characterization is only preliminary work, an accurate initial bend radius could not be found so the assumed bend radius from the mandrel was used for the data. This leads to errors in the positioning of the data overlaid onto the taper test data.

Using the material properties of the Lexan specimen, a correlation of structural strain to optical attenuation was made. The results of this testing showed that if the initial configuration of the sensor (initial bend radius, surrounding material effects, and temperature effects) could be controlled, a usable strain sensor could be developed. In several cases the optical fiber exhibited strain sensing abilities with ranges of 10000 micro strain or more.

An important note should be added about the effects of the Whispering Gallery mode fluctuations. If an optical fiber was developed which lacked the mode fluctuations present in the singlemode optical fibers it might actually produce a less effective strain sensor. This is because the oscillations of attenuation due to the Whispering Gallery mode are increasing the ratio of attenuation to bend radius which increases the sensitivity over the oscillation area. From the test of the optical fiber in sample structures it is seen that the changes in the fibers bend radius are much smaller than the changes required to cause the attenuation to cross multiple synchronous coupling points. Therefore if the sensor is designed correctly, the attenuation values will follow only one side of a Whispering Gallery mode oscillation and the sensitivity of the sensor will be large. Without the aid of the whisper mode oscillations, the attenuation as a function of fiber bend radius would have almost undetectable changes for the small radius changes. Due to this, the sensor would be very inaccurate. If the whispering Gallery mode effects could be properly characterized, a highly sensitive strain sensor can be produced.

There are several recommendations for future research which can be made since some of the research for this thesis was preliminary. A more in-depth study of the temperature characterization for the optical fibers is needed. Once properly evaluated, this method could possibly be used to determine the initial bend radii of the serpentine optical sensors. The effects of embedding the sensors in different materials is need to determine the attenuation to strain correlation. Without knowing the initial attenuation scaling, accurate strain readings would be impossible. Coatings applied to the optical fiber might be one solution. A more in-depth analysis of the whisper mode should be made in order to better understand the optical power issues. This would include using smaller radius increments between test points until the maximums of the fluctuations are found.

REFERENCES

- [1] K. C. Kao and T. W. Davies, "Spectrophotometric studies of ultra low optical glasses I: Single beam method," J. Sci. Instrum. 1, 1063-1068, 1968.
- [2] A. H. Cherin, An Introduction To Optical Fibers, McGraw-Hill, NY, 1983.
- [3] L. B. Jeunhomme, Single-Mode Fiber Optics, 2nd ed., rev. and expanded, Marcel Dekker, Inc., NY, 1990.
- [4] A. J. Harris and P. F. Castle, "Bend Loss Measurements on High Numerical Aperture Single-Mode Fibers as a Function of Wavelength and Bend Radius," J. Lightwave Tech., Vol. LT-4 NO. 1, Jan. 1986.
- [5] A. C. Demirdogen, J. R. Houghton, A. K. Tay, and D. A. Wilson, "Serpentine Optical Fiber Bending Transducer for Distributed Strain Measurements in Smart Structures," ASTM Symposium on Damage Detection and Quality Assurance in Composites, Nov. 13, 1990, San Antonio, TX.

APPENDIX A

Tabular Data For Attenuation as a Function of Optical Fiber Bending

Data is Tabulated as Sub-directory APPEND_A in disk Format

APPENDIX B

Results of Temperature Characterization Using Attenuation as a Function of Temperature

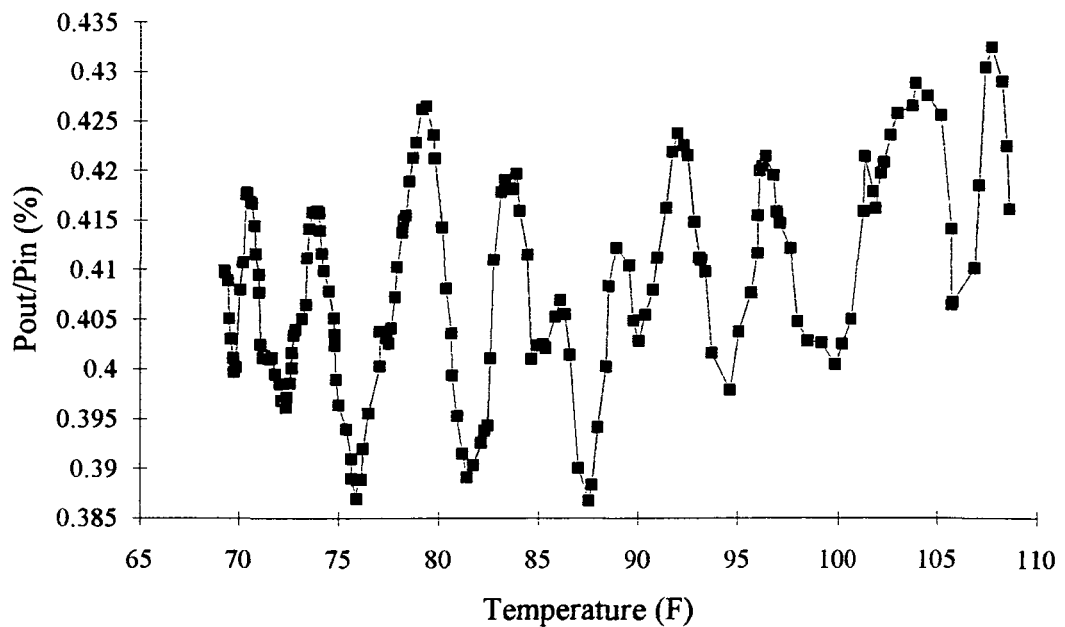


Figure B.1. Attenuation vs. Temperature at a Bend Radius of .329569 cm (Peak 1)

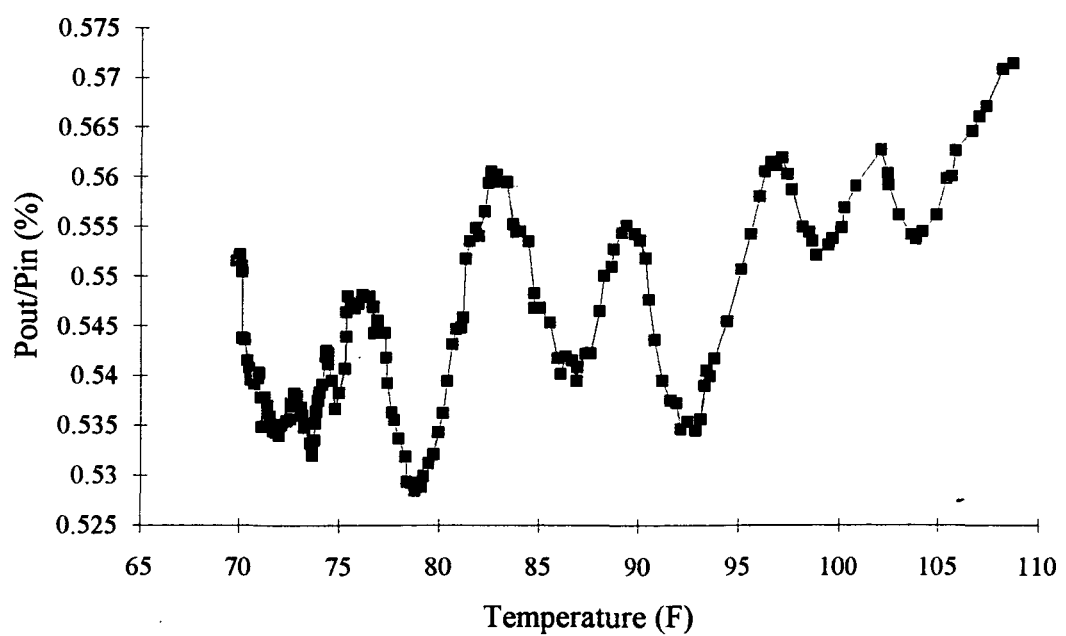


Figure B.2. Attenuation vs. Temperature at a Bend Radius of .352924 cm (Peak 2)

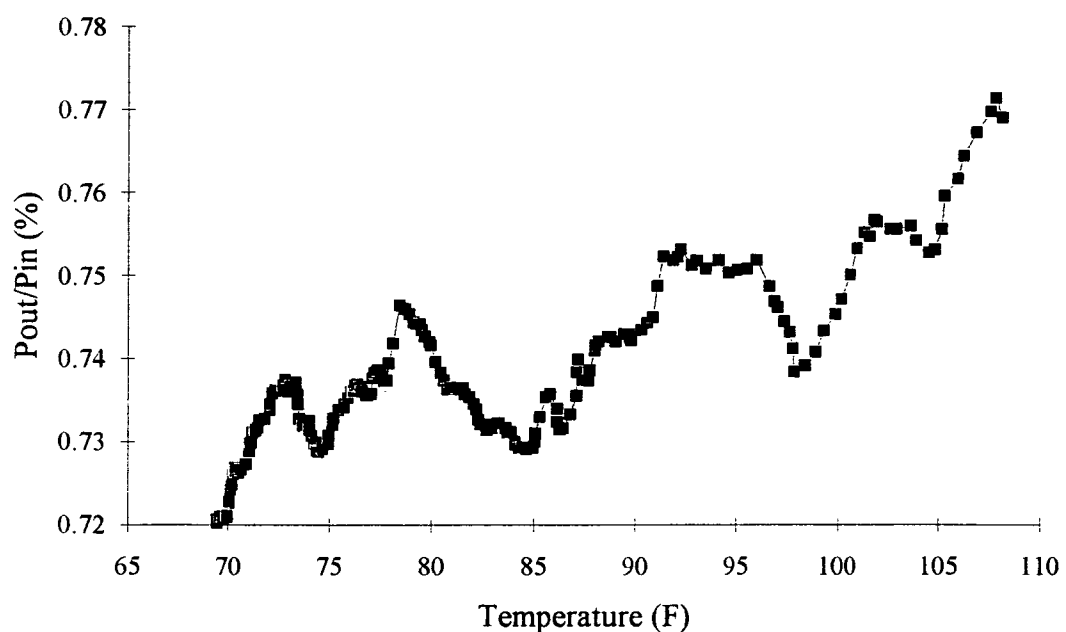


Figure B.3. Attenuation vs. Temperature at a Bend Radius of .381840 cm (Peak 3)

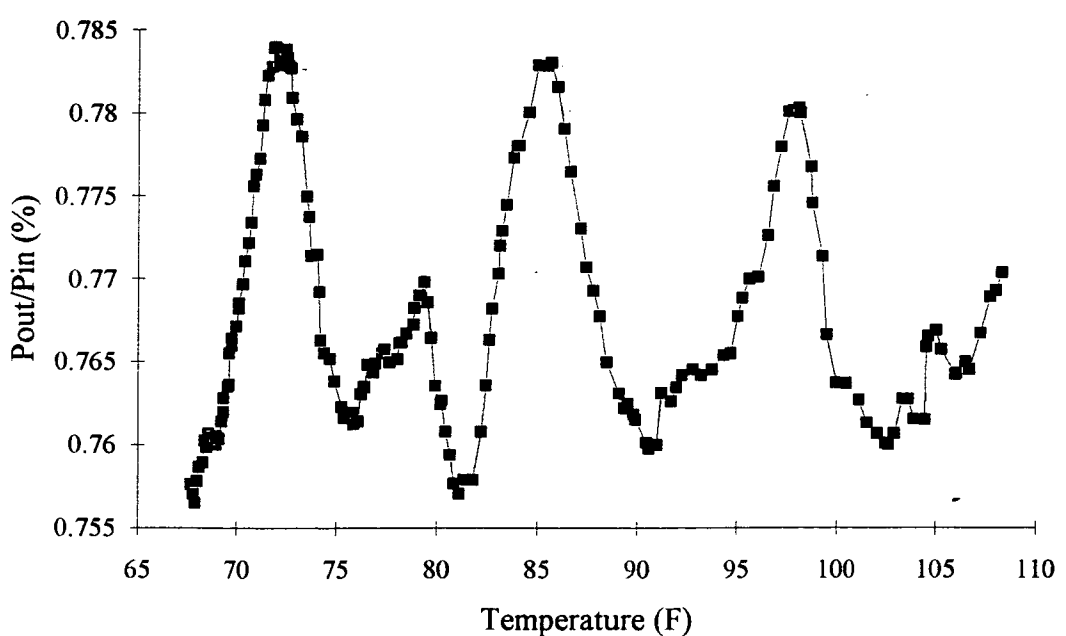


Figure B.4. Attenuation vs. Temperature at a Bend Radius of .409644 cm (Peak 4)

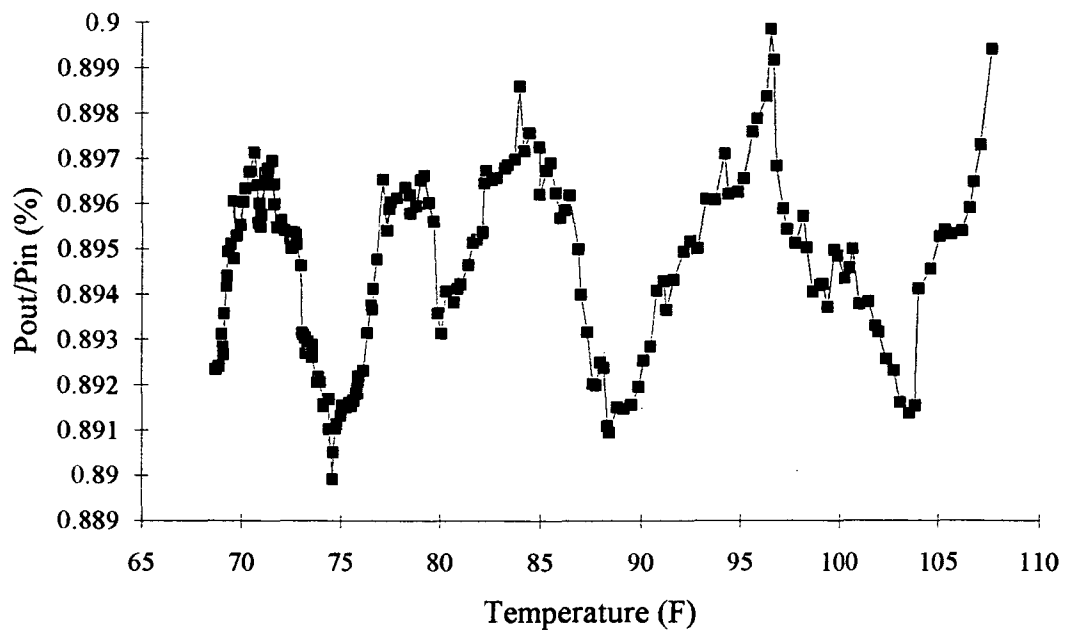


Figure B.5. Attenuation vs. Temperature at a Bend Radius of .444121 cm (Peak 5)

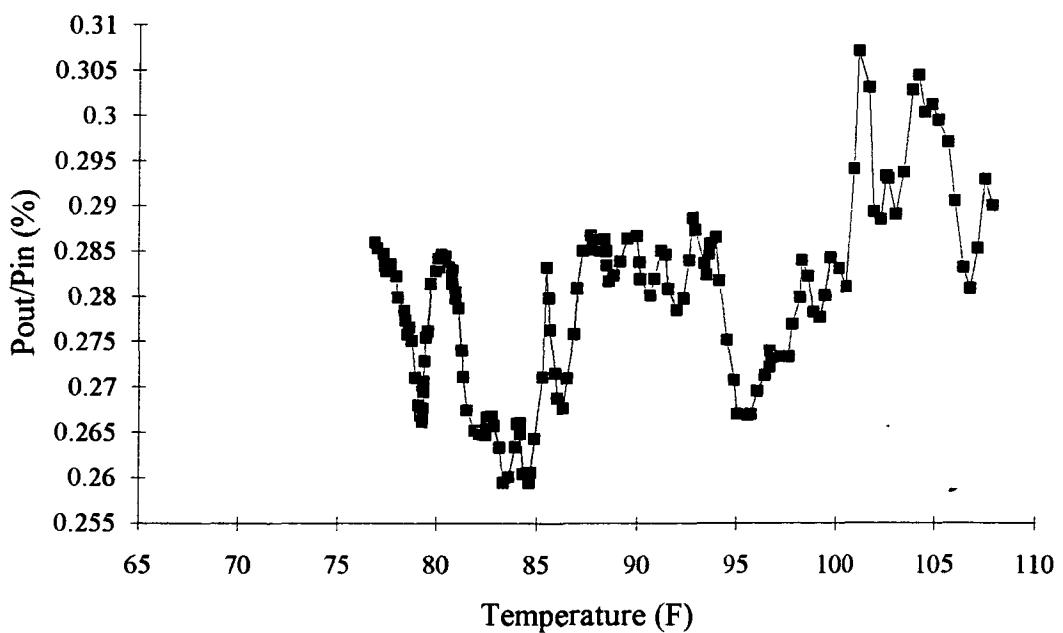


Figure B.6. Attenuation vs. Temperature at a Bend Radius of .334017 cm (Middle 1)

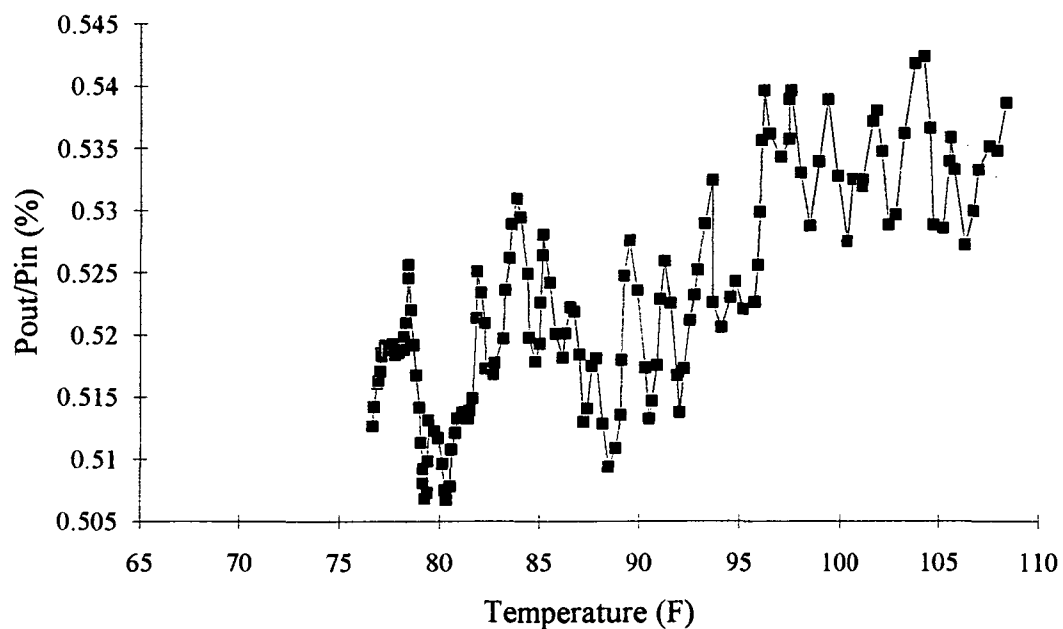


Figure B.7. Attenuation vs. Temperature at a Bend Radius of .347363 cm (Middle 2)

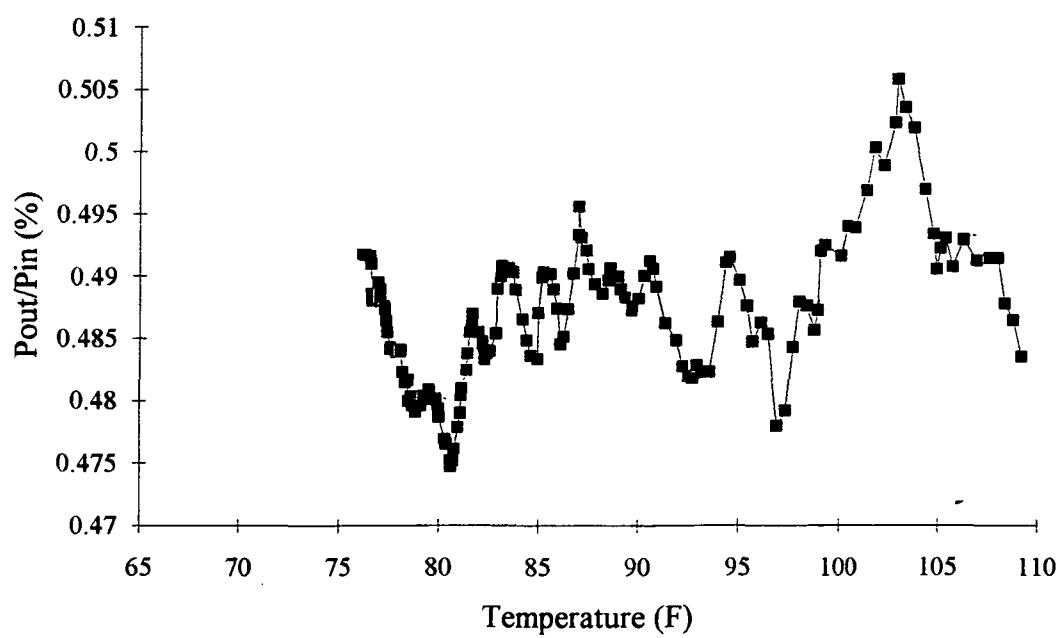


Figure B.8. Attenuation vs. Temperature at a Bend Radius of .419654 cm (Middle 3)

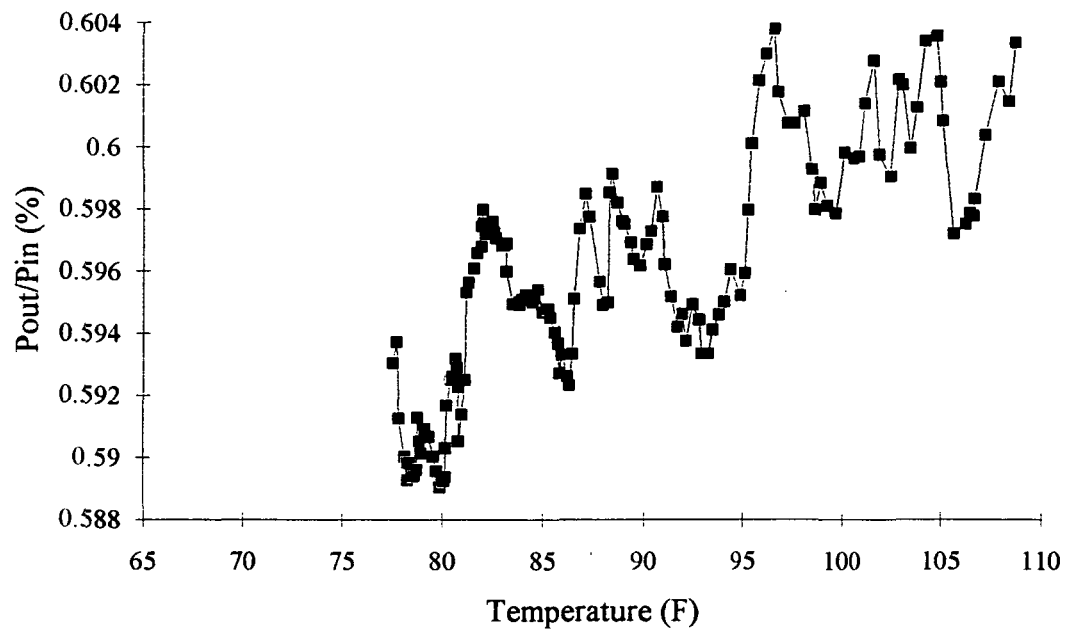


Figure B.9. Attenuation vs. Temperature at a Bend Radius of .435019 cm (Middle 4)

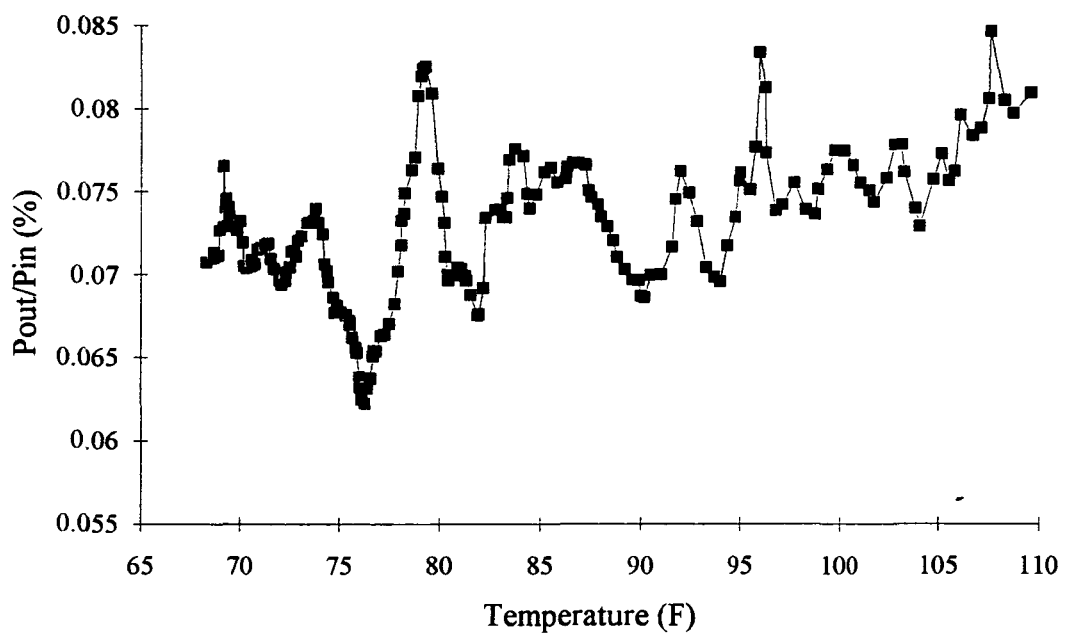


Figure B.10. Attenuation vs. Temperature at a Bend Radius of .340690 cm (Valley 1)

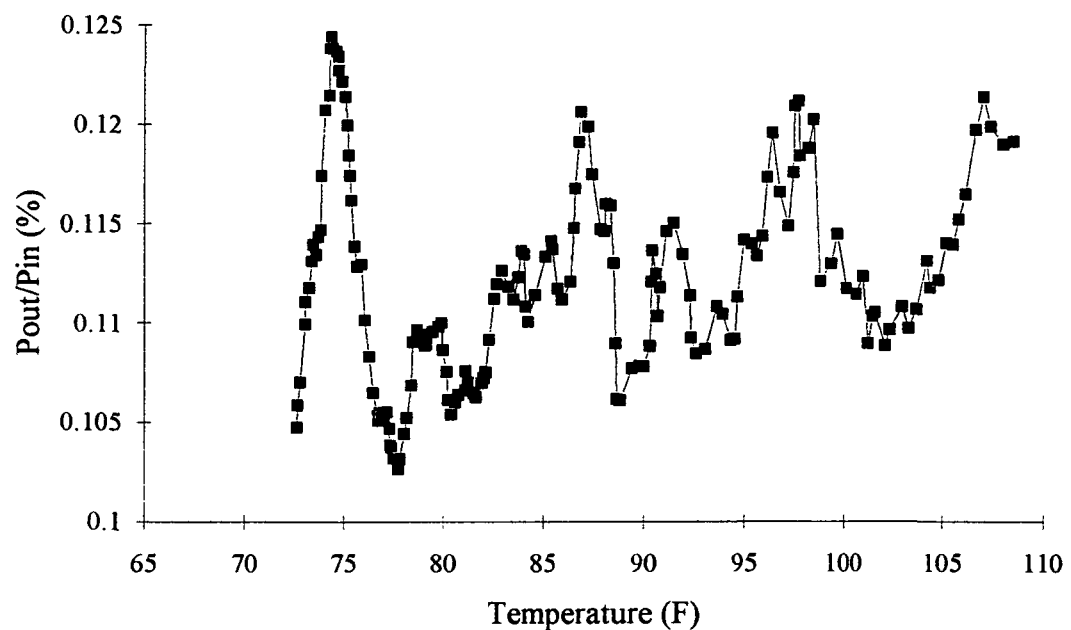


Figure B.11. Attenuation vs. Temperature at a Bend Radius of .366270 cm (Valley 2)

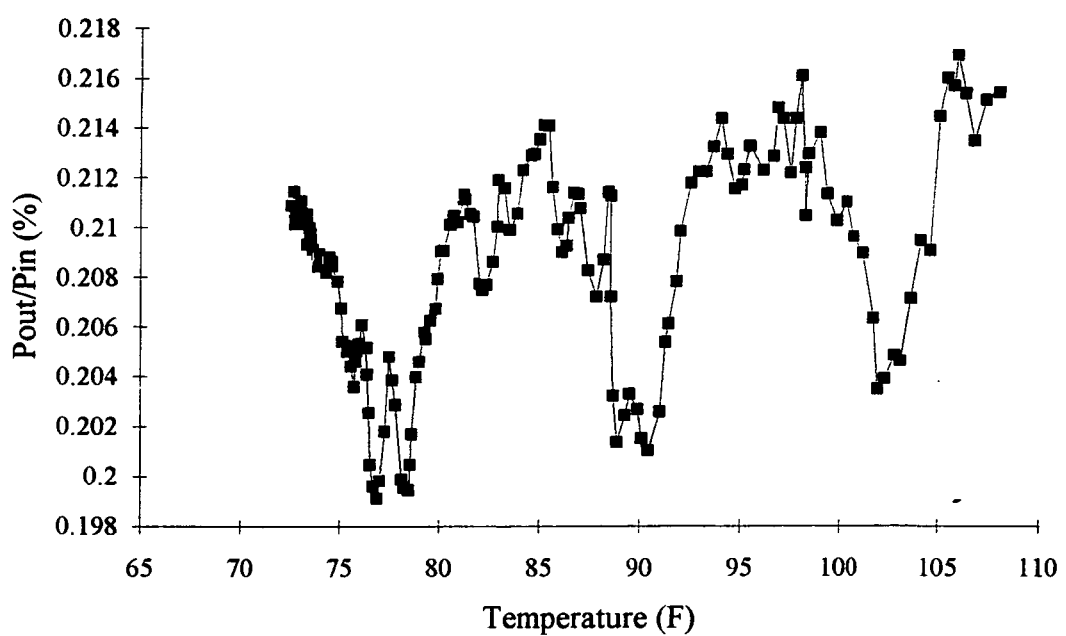


Figure B.12. Attenuation vs. Temperature at a Bend Radius of .395186 cm (Valley 3)

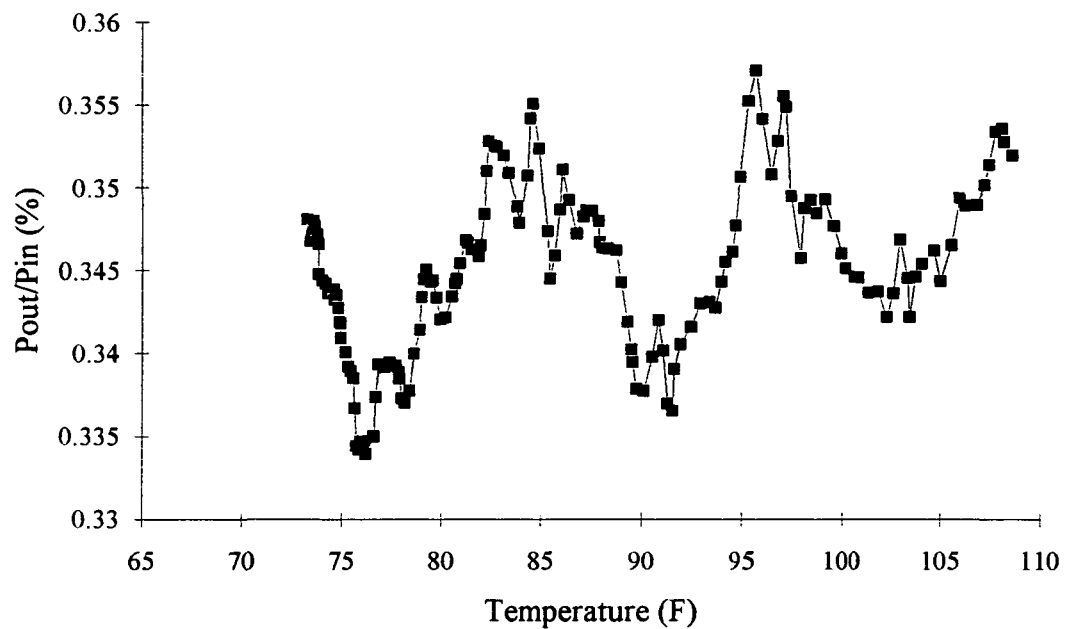


Figure B.13. Attenuation vs. Temperature at a Bend Radius of .427439 cm (Valley 4)

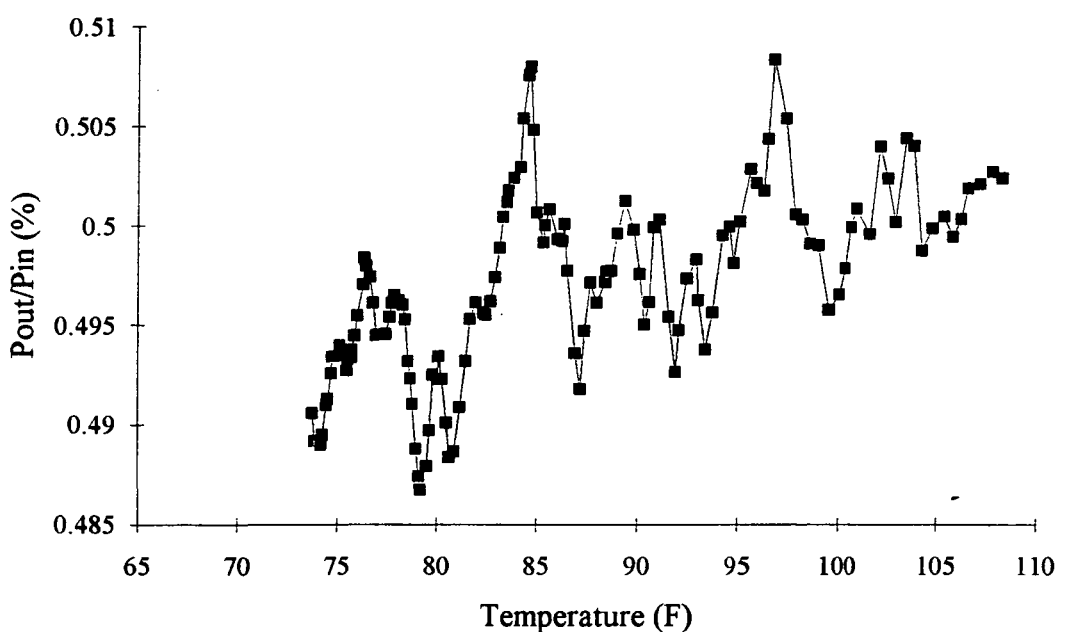


Figure B.14. Attenuation vs. Temperature at a Bend Radius of .460804 cm (Valley 5)

APPENDIX C

Tabular Data for Attenuation as a Function of Temperature Characterization

Data is Tabulated as Sub-directory APPEND_C in disk Format

APPENDIX D

**Results of Temperature Characterization Using Attenuation as a
Function of Temperature Rate (Fast Fourier Transform)**

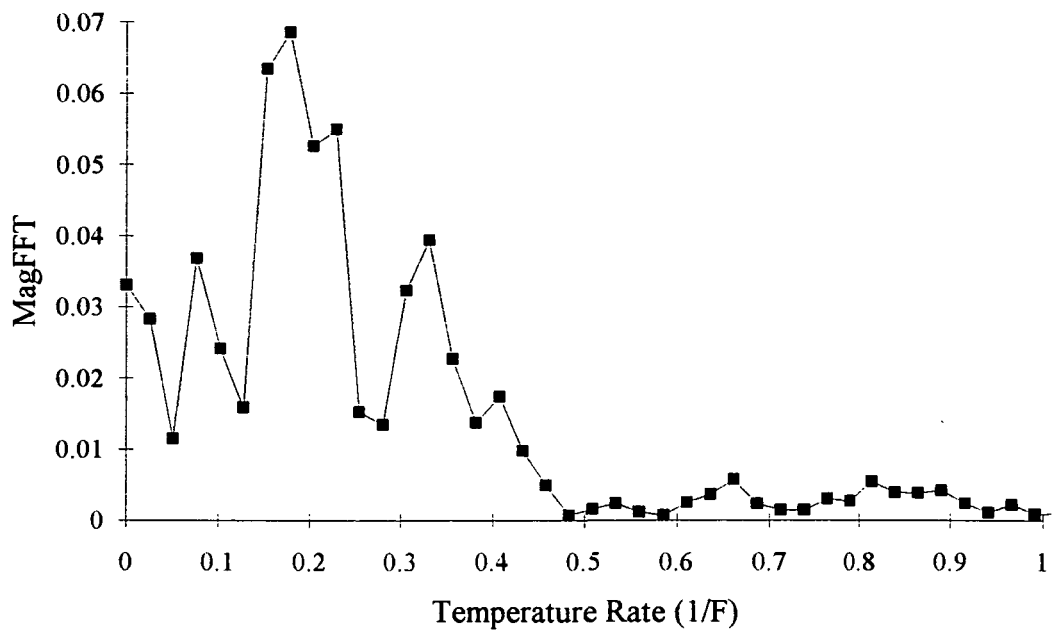


Figure D.1. Fourier Transform of Heat Test Data at a Radius of .329569 cm (Peak 1)

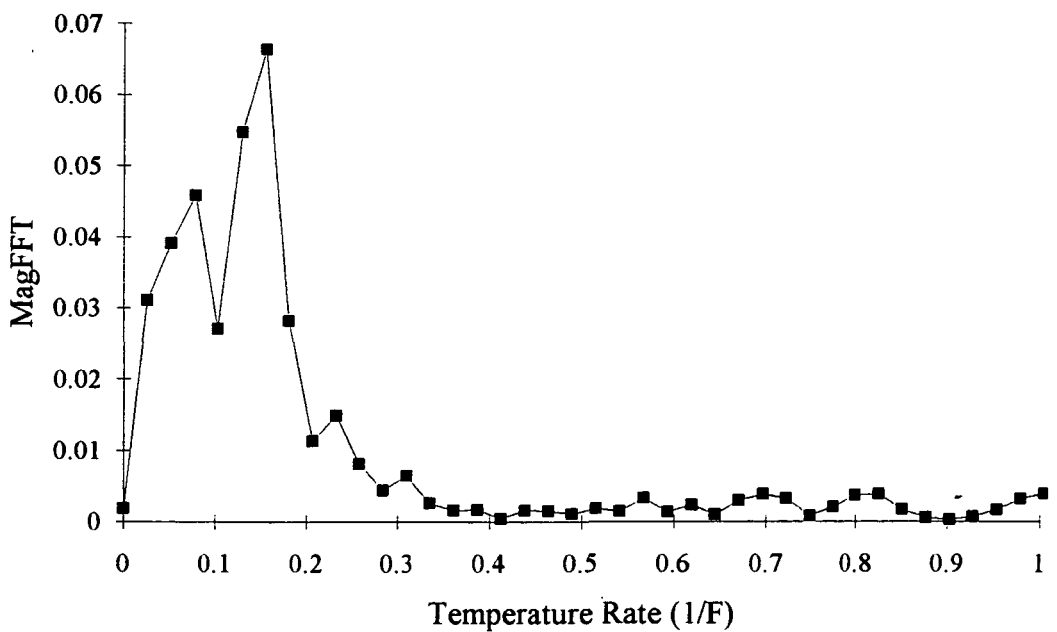


Figure D.2. Fourier Transform of Heat Test Data at a Radius of .352924 cm (Peak 2)

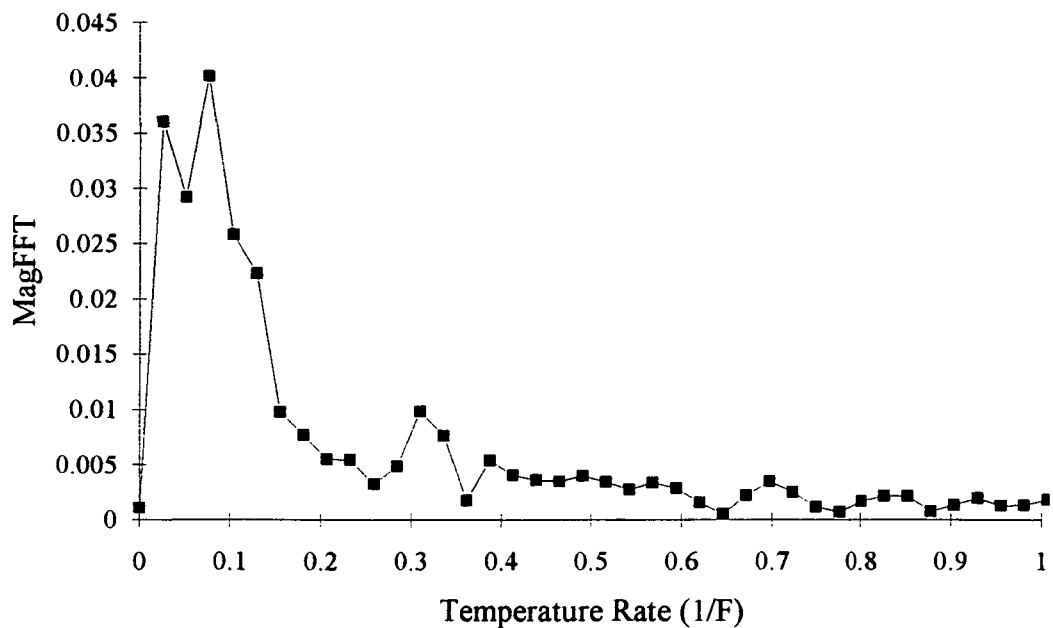


Figure D.3. Fourier Transform of Heat Test Data at a Radius of .381840 cm (Peak 3)

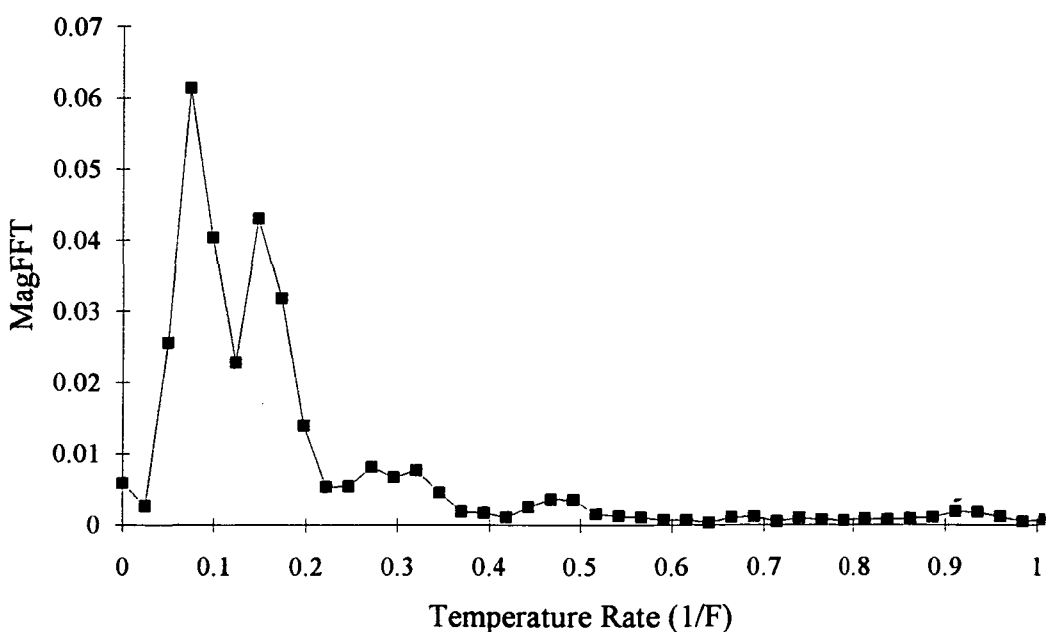


Figure D.4. Fourier Transform of Heat Test Data at a Radius of .409644 cm (Peak 4)

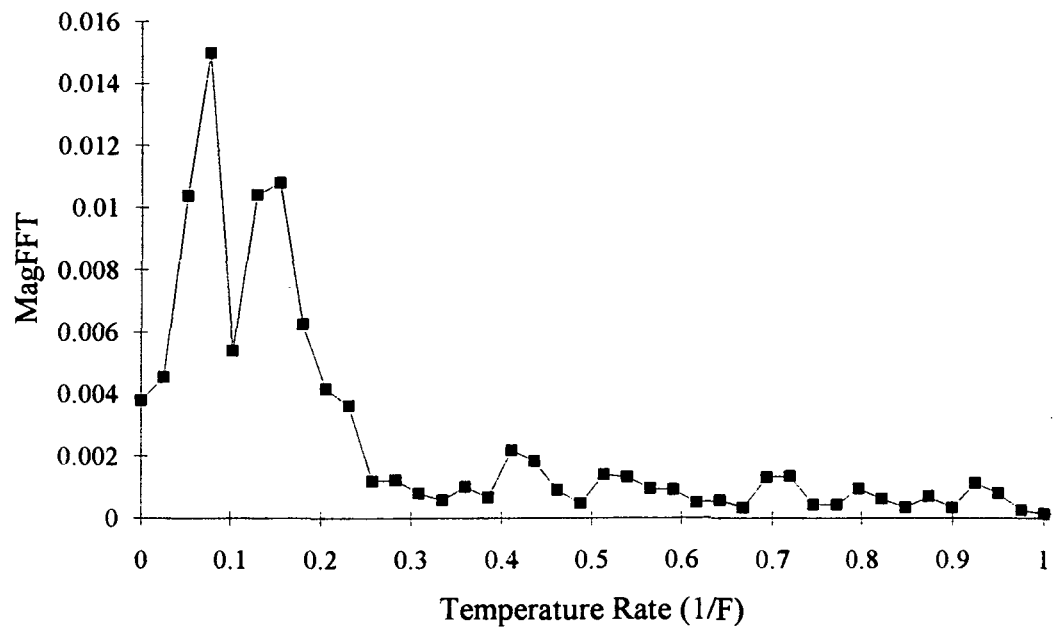


Figure D.5. Fourier Transform of Heat Test Data at a Radius of .444121 cm (Peak 5)

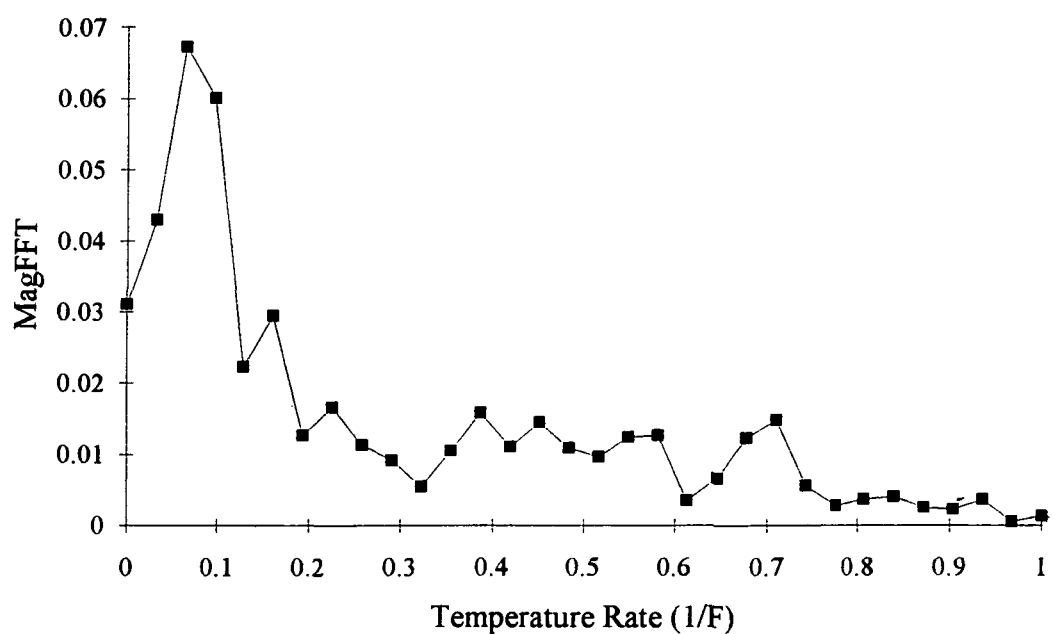


Figure D.6. Fourier Transform of Heat Test Data at a Radius of .334017 cm (Middle 1)

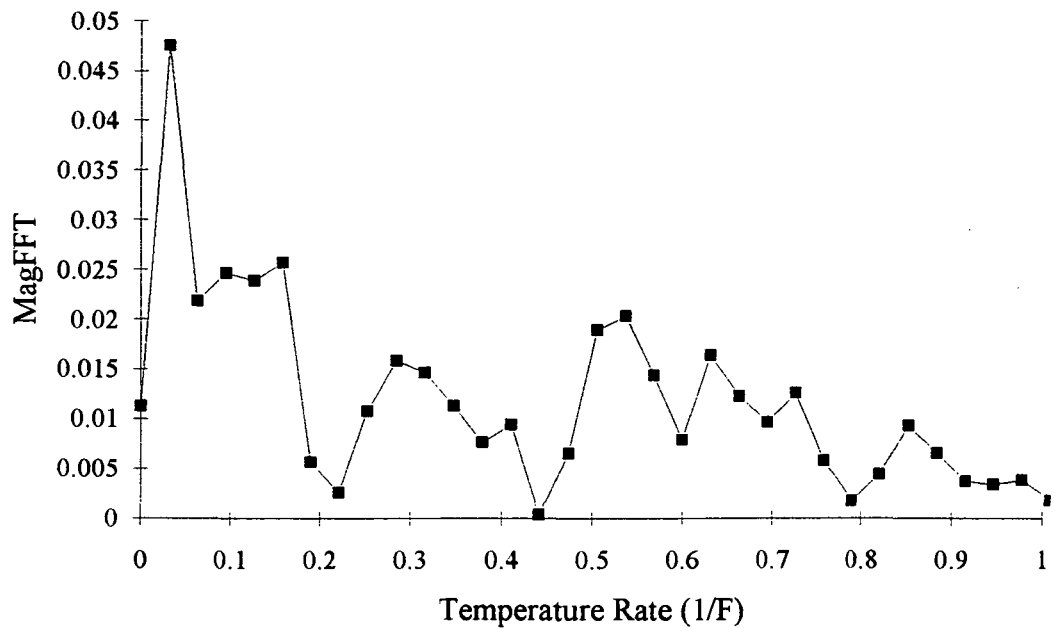


Figure D.7. Fourier Transform of Heat Test Data at a Radius of .347363 cm (Middle 2)

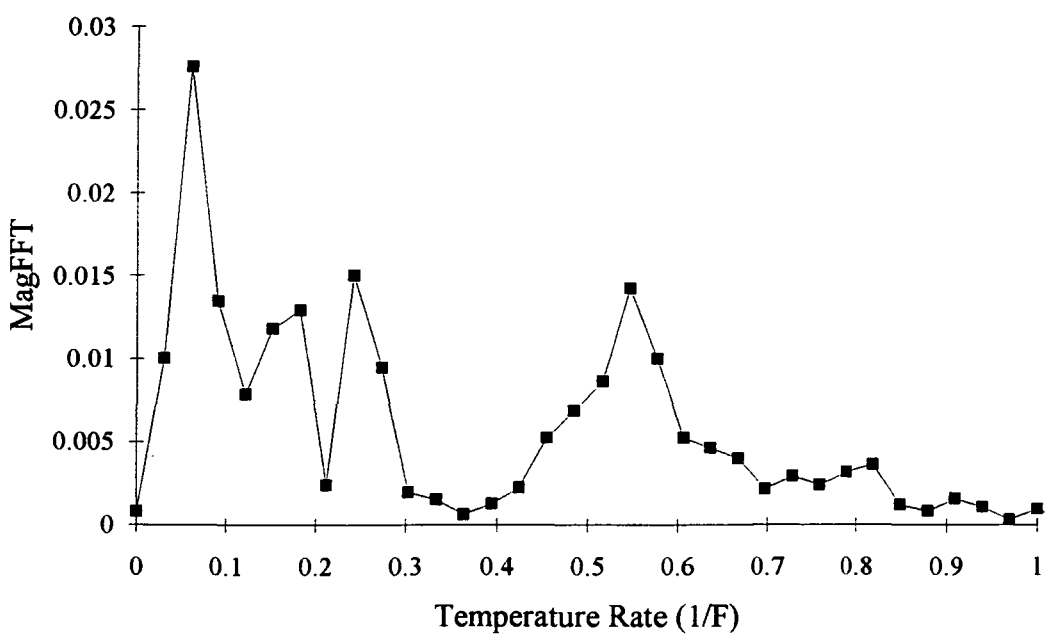


Figure D.8. Fourier Transform of Heat Test Data at a Radius of .419654 cm (Middle 3)

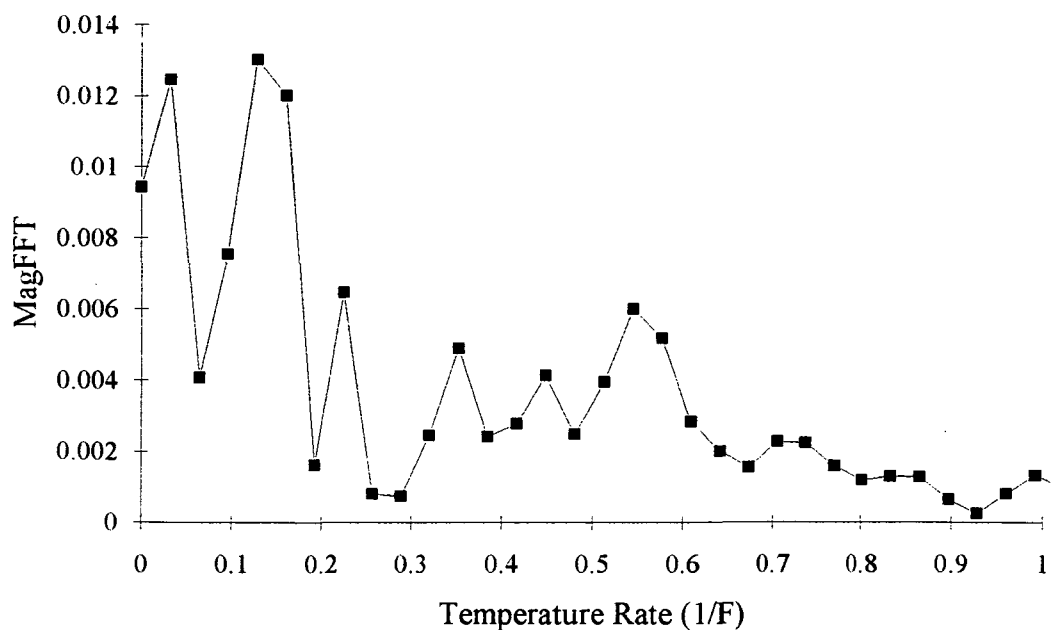


Figure D.9. Fourier Transform of Heat Test Data at a Radius of .435019 cm (Middle 4)

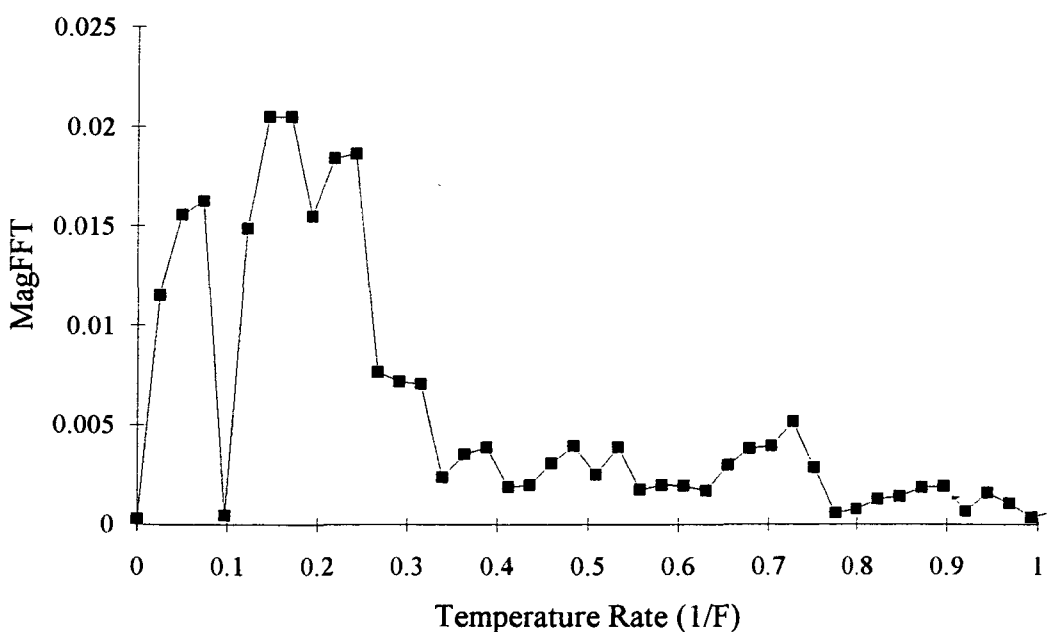


Figure D.10. Fourier Transform of Heat Test Data at a Radius of .340690 cm (Valley 1)

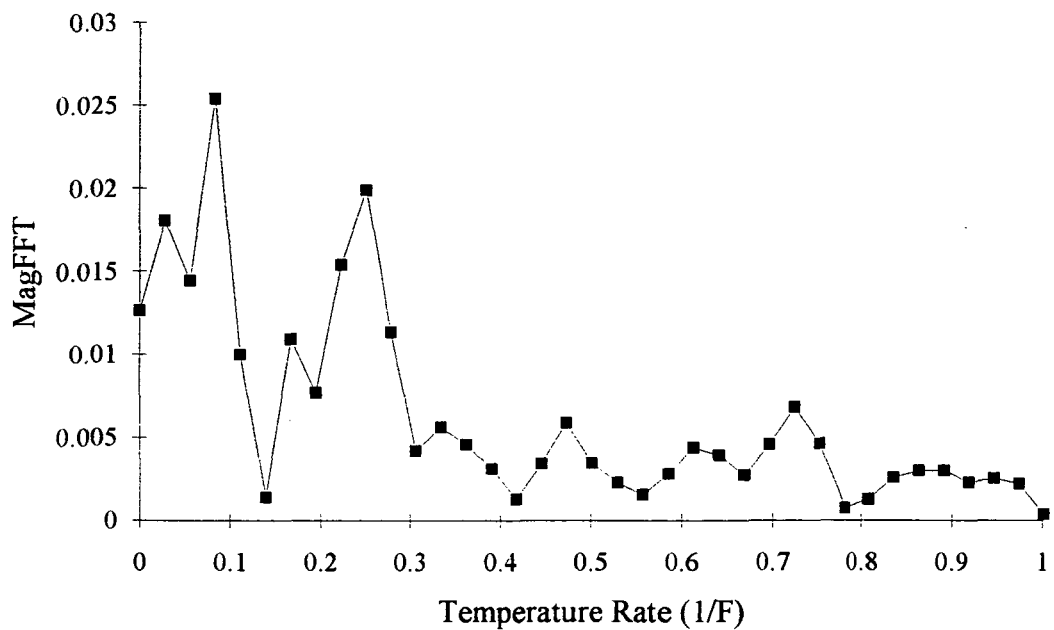


Figure D.11. Fourier Transform of Heat Test Data at a Radius of .366270 cm (Valley 2)

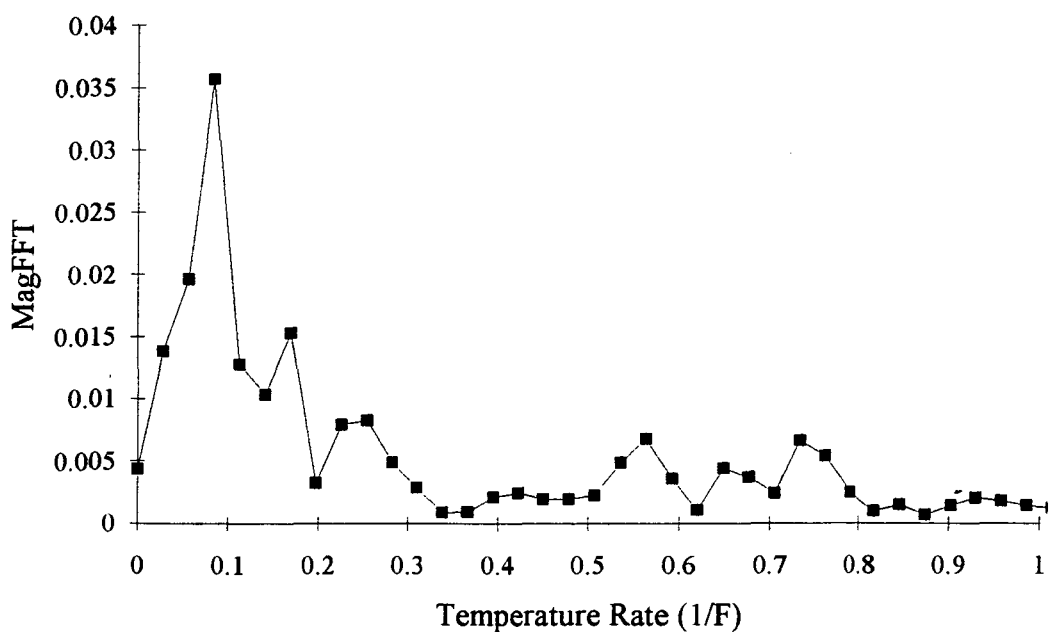


Figure D.12. Fourier Transform of Heat Test Data at a Radius of .395186 cm (Valley 3)

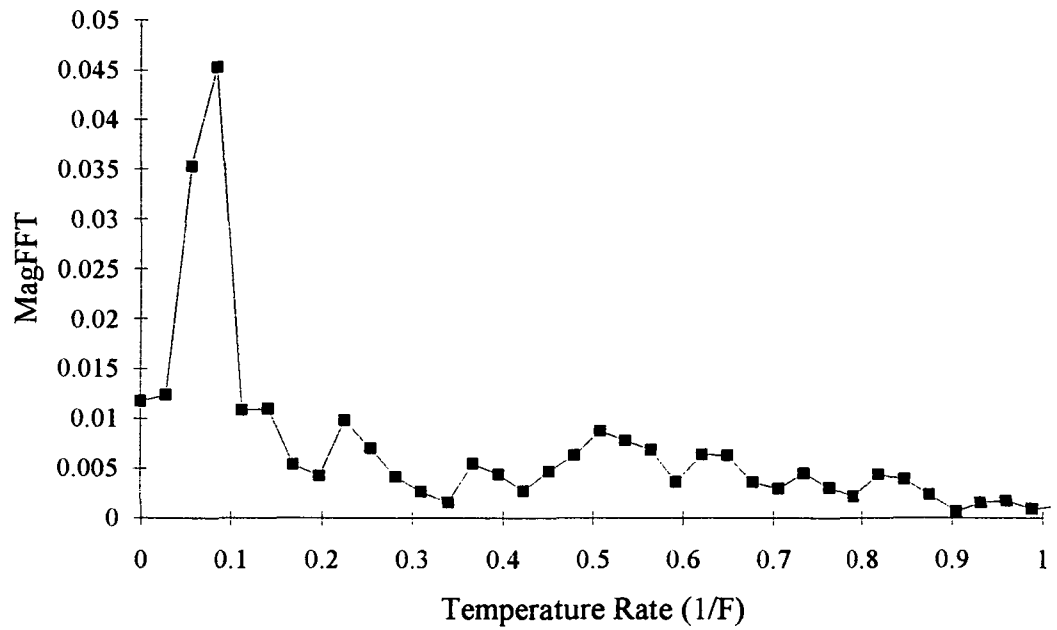


Figure D.13. Fourier Transform of Heat Test Data at a Radius of .427439 cm (Valley 4)

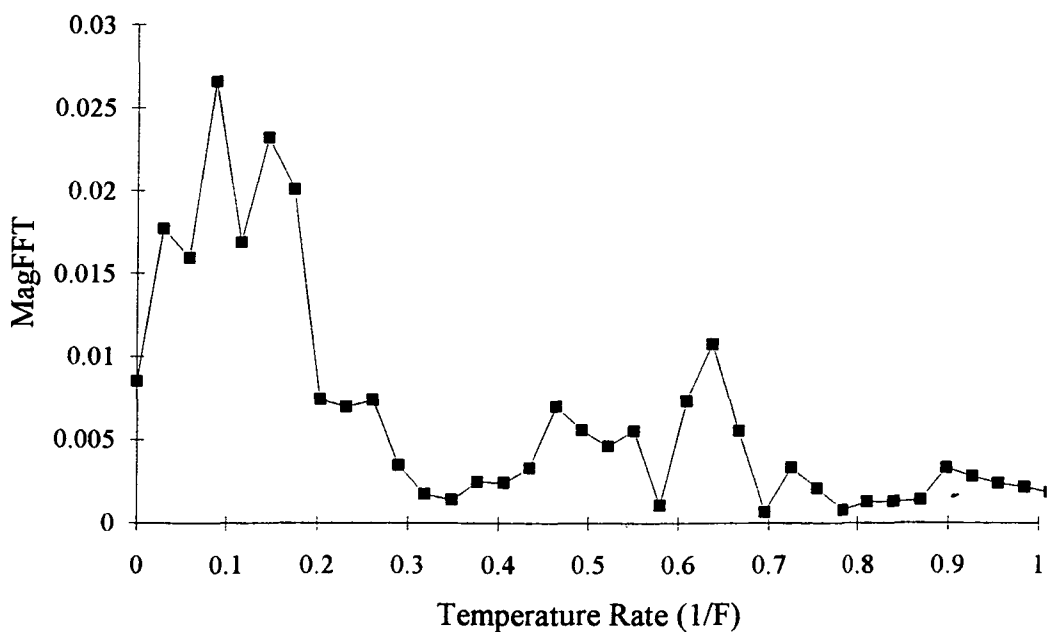


Figure D.14. Fourier Transform of Heat Test Data at a Radius of .460804 cm (Valley 5)

APPENDIX E

Data For Attenuation as a Function of Radius Change Using Optical Reflectometry

Data is Tabulated as Sub-directory APPEND_E in disk Format

APPENDIX F

Termination Methods For Optical Fibers Embedded in Multilayered Structures

The termination of an optical fiber as it exits a structure is a sub-topic in the application of optical fibers as strain sensing devices. Three methods of fiber termination described are: pigtailing, termination with the use of lenses and prisms, and termination using a newly developed boot connector. The qualities of each type of termination will be compared on the basis of simplicity, ease in manufacturing, reliability, and cost . Production descriptions will also be presented for the connector using prisms and lenses and for the boot connector.

Methods for terminating an optical fiber as it exits a device are critical in the application of optical fibers as strain sensing devices. The problem of fiber termination and connection is made more difficult since the optical fiber is embedded in the composite structures and cannot be brought through the layers of composite without experiencing bending. Small radii bends in the optical fiber severely limit the sensitivity of the fiber to strain induced bending loss and may yield the sensor useless.

In the field of optical communication the main requirement for an optical connector is that the attenuation levels due to joining fiber ends must be minimal. For strain sensing applications, the optical fibers are usually embedded in a structure or part and subjected to a high level of handling after connection. Due to this, the best connections would not only provide low attenuation losses, but be able to protect the fragile optical fiber.

Three methods for fiber termination are: pigtailing or leaving a section of optical fiber exposed at the end of the structure, using a series of lenses and prisms to obtain a fixed mountable connector, and using a boot which produces a soft bend and terminates the fiber with a mountable connector. A brief description to the pigtailing method is described, but the emphases of this paper is on the design and application of the mountable connectors since they would provide the protection to the optical fibers.

F.1 Pigtailing of Optical Fibers

The most simplistic method to exit a structure with an optical fiber is to leave a free length of fiber at the edge of a part. This method, known as pigtailing, is very cost effective since the only requirements for connection is the use of a standard glass splice or a fusion splicing technique. The disadvantages of this method are in reliability, stability, and orientation of exit direction.

The pigtail fiber is very susceptible to breakage at the point of structure exit since it is unprotected and very fragile. Normally the buffer on the fiber allows for sufficient bending to avoid breakage, but since the fiber is fixed to the structure at the exiting surface, slight bends of the pigtail lead to a sharp bend radius at the exit and can easily cause breakage. Also if the fiber is embedded in a composite structure, the resin bleed off on the fiber makes the buffer brittle and decreases the fibers ability to bend without breaking. When the structure with the optical fiber embedded is being produced, tested, or placed in assembly, the fiber is susceptible to breakage due to the high level of human handling and the smallness of the fiber size. The other main disadvantage of the pigtailing method is the exit orientation of the fiber. The optical fiber must exit on the plane with which the fiber is placed. This allows for only two dimensional placement of the fiber as it exits a structure or part. For optical fibers embedded in a structure, the fiber can only exit from the sides of a part which leads to problems when the part is machined, or placed in assembly. The many disadvantages of this method greatly outweigh the cost advantage.

F.2 Connectorization Using Prisms and Lenses

A method for eliminating the problems of pigtailing optical fibers is to use a mountable terminating connector. Connectors offer a fixed end which allows optic cables to be attached directly to the structure without the need for a permanent connection such as splicing. A connector which employs Gradient Index (GRIN) lenses and a ninety

degree prism has been developed which provides protection to the delicate fiber and allows for cable connection.

As shown in Figure F.1, the connector relies on the basic principles that light exiting a medium travels in a straight line.

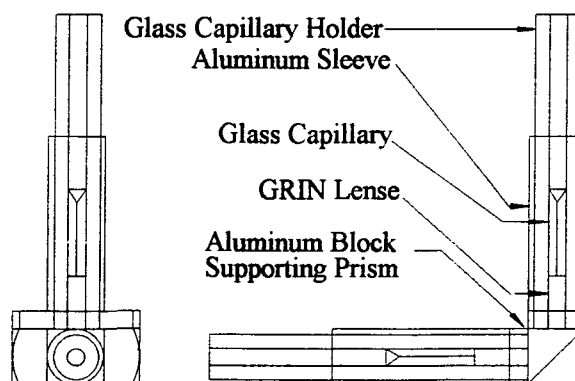


Figure F.1. Prism-Lens System For Fiber Termination

For an entrance connector, the light from a pigtailed source is lead into the connector through a glass capillary which centers the fiber on a GRIN lens. The GRIN lens is mounted with its surface touching a 90 degree prism. An identical setup of capillary and GRIN lens is placed on the other face of the prism allowing the light to be passed through the connector. The light enters the first GRIN lens from the source fiber, is passed through the glass of the prism, and exits the connector through the second GRIN lens and fiber. Due to the index changes in the lenses, the point source entering the lens travels as a sine wave as shown in Figure F.2.

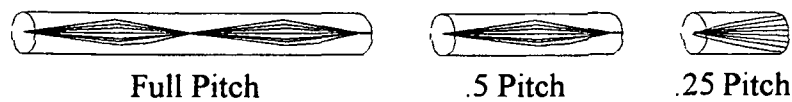


Figure F.2. Sine Wave Light Pattern Through GRIN Lens

If the lens is cut to a .25 pitch length, the point source is magnified, which allows for ease in alignment at the prism surfaces. The lenses also have property of converting a broad source to a point source so the second GRIN lens reduces the enlarged light to a point and transfers the light into the exiting fiber.

The two aluminum sleeves are machined using a lathe with the flange sides cut after machining to mate with the prism block. The prism block is manufactured using a milling machine which allows for precision parallel surfaces with good surface flatness. Glass capillary holders are used for their compatibility to the glass capillaries and GRIN lenses. The connector is mounted with the embedded glass holder permanently attached to the aluminum sleeve while the exposed glass holder is not fixed and can be removed until optical testing is desired. The connector can be embedded completely as long as the top of the exiting aluminum sleeve is not covered. This allows for the same connector to be used with a variety of structure thicknesses.

The advantages of this connector type are: the optical fiber is not exposed to the environment and cannot be inadvertently broken, the optical cables to the equipment do not have to be permanently fixed to the structure and can be connected only when needed, and the exit direction of the fiber is unlimited so long as the entrance and exit ports are separated by ninety degrees. The cost of this type of connection is approximately ten times the cost of pig tailing the optical fibers, but the prism-lens connector does not have the disadvantages of the pigtail connection.

Disadvantages of the prism-lens system are in the alignment of the lenses to the prism and the amount of light attenuation produced from the interfaces. Due to the small size, the separate parts of the connector must be glued instead of mechanically fixed thus some drift during bond setup is experienced when the connectors are made. In order for the connector to transmit light, the aluminum sleeves must be exactly ninety degrees from

each other in two dimensions and their centers must be at the same plane point on the two sides of the prism. Any misalignment experienced in curing the bond epoxy yields an unusable connector. The attenuation of the connector is large compared to commercial connectors due to the multiple interface surfaces. The connector has four splice points, two between the fibers and the lenses and two between the lenses and the prism. The mirror like surfaces on the glass reflect a portion of the light at each interface. The probability of misalignment is also increased by these numerous interfaces. The high level of production difficulty and the cost of the connector reduce the advantages of this method.

F.3 Connectorization Using The Boot Connector

A third method for termination and connection of optical fibers makes use of a soft radius bend and a base support foot to terminate surface mount fibers or exit composites with embedded fibers. The connector does not require alignment of optics such as lenses or prisms, but still retains the desired properties of the prism-lens system. As shown in Figure F.3 below, the connector is composed of a support foot, a tube which allows the fiber to exit the composite, and a ferrule which can be polished and connected to an optic cable with a female-female mating sleeve.

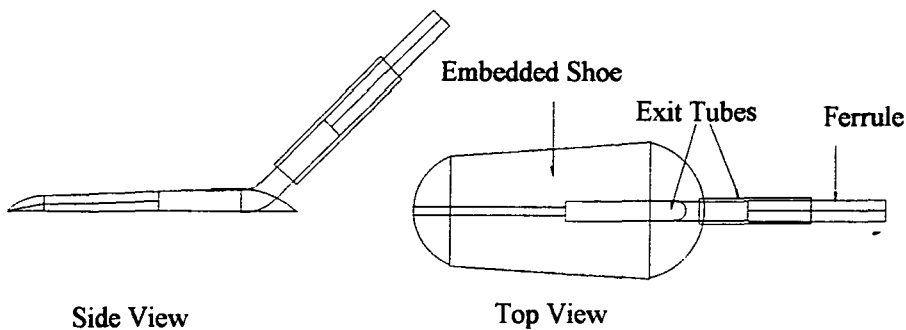


Figure F.3. Boot Connector For Fiber Termination

The connector has the same good qualities of standard pigtailing since it does not contain lenses or have multiple interfaces. Design of the connector is based on the optical fibers ability to sustain bends of large radii, with respect to the fiber diameter, and still transmit light. For strain sensing applications, the optical fiber is of a serpentine configuration in the structure or part, so a bend larger than the serpentine bends will not attenuate the light. The only attenuation of the connector is between the ends of the sensor fiber and the cable leading to the equipment which is equivalent to pigtailing.

The boot, formed from three machined aluminum parts, is surface tapered and rounded to reduce any resin rich regions around the connector and provide a stable base for the connector tube. The ferrule is mounted to the aluminum tube by a sized sleeve providing the proper ferrule length and cavity to epoxy the connector. Although the connector cannot obtain an exit angle greater than forty-five degrees, it allows the termination to be on the surface of the structure or part and provides protection to the delicate optical fibers. The connectors cost is approximately 4 times the cost of pigtailing and is simplistic in design. It can be fabricated to conform to virtually any part design and still provide connector losses comparable to pigtailing and splicing. The boot of the connector can be made of virtually any machineable or moldable product as long as the material can withstand the cure temperatures of the optical epoxy and the composite part. The only limitation of this type of connector is that the bend radius of the connector tube must be greater than the bend radii of the serpentine fiber mounted or embedded.

F.4 Summary of Termination Methods

The proper termination and connectorization of optical fibers embedded in composite structures has more requirements than the standard communications industry. The connectors must provide protection for the optical fibers as well as exhibit low attenuation at the connection.

Three types of connections presented were standard pigtailing, connecting with a series of lenses and prisms, and connection using a soft bend boot. The advantages and disadvantages of each are as follows:

The pigtail provides low cost and simplistic connection, but does not protect the optical fiber as it exits the structure. With the pigtail connection, the only fiber orientation upon exit is from the end of the part and is limited to the sensor plane. If the fiber is broken, the sensor is rendered useless.

The lens-prism connector offers protection to the optical fiber and allows the connections to be made from the surface as well as the side, but production difficulties and high attenuation due to multiple interfaces reduce the effectiveness of the connector. The connector must be perfectly aligned on two axes and have entrance and exit sleeve centers aligned. The cost of this type of connector is also high compared to the other two methods.

The connection using a soft bend and a rounded boot provides the positive properties of both pigtailing and connecting with the lens-prism system. The attenuation is minimized by having only one interface, the fiber is protected, the cost is reduced, and the exit orientation is not limited to the structure end or the plane of the sensor. The connector base can be machined from various materials such as aluminum, plastic, steel, or monolithic graphite or can be molded to conform to almost any surface configuration. The only requirements for this type of connection is that the base material is capable of withstanding the cure processes for the optical epoxy and the composite and that the bend radius of the connector is larger than the bend radius of the serpentine. The connector can be fitted with industry standard ferrules which increases compatibility with products already on the market.

Of the three types of connectors discussed, the soft bend boot seems to exhibit the greatest advantages with the fewest weaknesses. The ease in production and the flexibility of this connector allow a wide range of connector placement configurations from one standard connector.

APPENDIX G

Results From testing Sample Structures Under Three point Loading
Data is Tabulated as Sub-directory APPEND_G in disk Format

APPENDIX H

**Data Aquisition Program Used to Transfer Data From LeCroy Sampling Oscilloscope to a
Computer**

```

10 ***** This Prgram Is Used With The LeCroy Sampling
20 ***** Oscilloscope To Retrieve Data For The Optical
30 ***** Fiber Strain Sensing Tests. The RS-232 on
40 ***** The LeCroy Is Connected To The 9-Pin Com2 Of The
50 ***** Computer. Note A NULL MODEM Must Be Used For
60 ***** Communications.
70 '
80 ***** Communications Port and Output Files Initialization
90 '
100 open "com2:9600,n,8,1" as #1
110 open "b4ptnum1.dat" for output as #2
120 open "b4femeal.dat" for output as #3
130 open "b4fesde1.dat" for output as #4
140 open "b4ffmeal.dat" for output as #5
150 open "b4ffsde1.dat" for output as #6
160 open "b4c1meal.dat" for output as #7
170 open "b4c1sde1.dat" for output as #8
180 open "b4c2meal.dat" for output as #9
190 open "b4c2sde1.dat" for output as #10
200 '
210 ***** Initializing Computer/Oscilloscope Connection
220 '
230 print #1, chr$(27)+"R"
240 remote$=input$(10,#1)
250 ' print "remote="remote$
260 for x = 1 to 500
270 '
280 ***** Triggering Of Oscilloscope
290 '
300 print #1, "TRMD NORM"
310 print #1, "FE:FRST"
320 print #1, "FF:FRST"
330 ini$=input$(29,#1)
340 ' print "ini="ini$
350 delay 10
360 '
370 ***** Stopping Trigger
380 '
390 print #1, "TRMD SINGLE"
400 '
410 ***** Calling For Mean and Standard Deviation of Signals
420 '
430 print #1, "FE:PAVA? MEAN,SDEV"

```

```
440 feini$=input$(46,#1)
450 ' print "feini="feini$
460 input #1,femean
470 print "femean="femean
480 b1$=input$(9,#1)
490 ' print "b1$="b1$
500 input #1,fesdev
510 print "fesdev="fesdev
520 B2$=INPUT$(5,#1)
530 ' PRINT "B2$="B2$
540 print #1, "FF:PAVA? MEAN,SDEV"
550 ffini$=input$(33,#1)
560 ' print "ffini="ffini$
570 input #1,ffmean
580 print "ffmean="ffmean
590 C1$=INPUT$(9,#1)
600 ' PRINT "C1$="C1$
610 input #1,ffsdev
620 print "ffsdev="ffsdev
630 C2$=INPUT$(5,#1)
640 ' PRINT "C2$="C2$
650 print #1, "C1:PAVA? MEAN,SDEV"
660 c1ini$=input$(33,#1)
670 ' print "c1ini="c1ini$
680 input #1,c1mean
690 print "c1mean="c1mean
700 D1$=INPUT$(9,#1)
710 ' PRINT "D1$="D1$
720 input #1,c1sdev
730 print "c1sdev="c1sdev
740 D2$=INPUT$(5,#1)
750 ' PRINT "D2$="D2$
760 print #1, "C2:PAVA? MEAN,SDEV"
770 c2ini$=input$(33,#1)
780 ' print "c2ini="c2ini$
790 input #1,c2mean
800 print "c2mean="c2mean
810 E1$=INPUT$(9,#1)
820 ' PRINT "E1$="E1$
830 input #1,c2sdev
840 print "c2sdev="c2sdev
850 E2$=INPUT$(5,#1)
860 ' PRINT "E2$="E2$
```

```
870 '
880 ***** Printing Input Data To Output Files
890 '
900 print #2,using "#####.#";x
910 print #3,using "+#.#####~~~";femean
920 print #4,using "+#.#####~~~";fesdev
930 print #5,using "+#.#####~~~";ffmean
940 print #6,using "+#.#####~~~";ffsdev
950 print #7,using "+#.#####~~~";c1mean
960 print #8,using "+#.#####~~~";c1sdev
970 print #9,using "+#.#####~~~";c2mean
980 print #10,using "+#.#####~~~";c2sdev
990 print x" loop(s) completed"
1000 '
1010 ***** Prompt user to restart sequence when ready
1020 '
1030 print "press any key to take next data, press 'q' to end"
1040 input aaa$
1050 if aaa$="q" then goto 1100
1060 next x
1070 '
1080 ***** Setting Oscilloscope To Local Mode
1090 '
1100 print #1,chr$(27)+"L"
1110 beep
1120 print "done"
1130 end
```